Geosciences and engineering : a publication of the University of Miskolc

6. évf. 9. sz. / 2018

Jarzyna, Jadviga A. - Krakowska, Paulina I. - Puskarczyk, Edita - Wawrzyniak-Guz, Kamila - Zych, Marczin Petrophysical Characterictics of the Sale Gas Formations in the Baltic Basin, Northern Poland	9–18
Drahos Dezső - Galsa Attila - Gyulai Ákos - Ormos Tamás - Dobróka Mihály Application of Optimum Weights in Geophysical Data Inversion	19–31
Nuamah, Daniel O. B. - Dobróka Mihály Reduction to Pole of Non-Equdistantly Measured Magnetic Data Using an Inversion-Based Fourier Transformation Algorithm	32–39
Baracza Mátyás Krisztián - Turai Endre - Nádasi Endre - Gyulai Ákos CGI Inversion Method Presaented Through a Field Case	40–52
Kiss Anett - Dobróka Mihály Improvement of a Seismic Q Model	53–59
Timár Gábor - Drahos Dezső - Molnár Gábor - Varga Péter Towards to the Geodit - A Short Overwiev of the History of Gravimetric Measurements in Geodesy	60–74
Tóth Gyula - Völgyesi Lajos Experiences of Qdeadalus Measurement	76–86
Abordán Armand - Szabó Norbert Péter Particle Swarm Optimization Assisted Factor Analysis for Shale Volume Estimation in Groundwater Formations	87–97
Akbar, Muhammad Nur Ali A Systematic Dependence of Acoustic Velocity on Internal Pore Structure in Standstone	98–117
Ilyés Csaba - Turai Endre - Szűcs Péter - Ilyés Tamás Examination of Debrecen's 110-year Rainfal Data	118–126
Czirok Lili - Kuslits Lukács Effects of Earthquake Data Clustering on the Results of Stress Inversions	127–141
Nádasi Endre - Turai Endre Increasing the Accuracy of GPR Measurements	142–150
Somogyiné Molnár Judit - Kiss Anett - Dobróka Tünde Edit Global Joint Inversion of Acoustic Velocity and Quality Factor Data Using Rock Physical Models	151–162
Dobróka Mihály Márton A Least Squares Inversion Procedure Applied to Parameter Estimation of Dynamic Ordering in Superconducting Vortex Systems	163–175

Geosciences and Engineering, Vol. 6, No. 9 (2018), pp. 9–18.

PETROPHYSICAL CHARACTERISTICS OF THE SHALE GAS FORMATIONS IN THE BALTIC BASIN, NORTHERN POLAND

JADWIGA A. JARZYNA–PAULINA I. KRAKOWSKA–
EDYTA PUSKARCZYK–KAMILA WAWRZYNIAK-GUZ–MARCYN ZYCH

jarzyna@agh.edu.pl; krakow@agh.edu.pl; puskar@agh.edu.pl;
wawrzyni@agh.edu.pl, zychagh@gmail.com
AGH University of Science and Technology, Krakow, Poland;
Faculty of Geology Geophysics and Environmental Protection,
Department of Geophysics

Abstract: Results of laboratory experiments combined with well logging to get information on density and porosity together with mineral composition were the basis for shale gas rock model construction. Density – bulk, skeletal and grain determined from various laboratory experiments and porosity – total, effective/dynamic and from dual liquid immersion measurement, well correlating with TOC and volume of kerogen, showed the place of organic matter and gas in pore space and the skeleton of claystone-mudstone gas formations. Results of pyrolysis (Rock-Eval), i.e. TOC (Total Organic Carbon) used to determine the hydrocarbon generation potential of rocks were also considered together with element composition from chemical analyses and mineral composition from XRD measurements. SCAL analysis, NMR experiments, Pressure Decay Permeability measurements together with water immersion porosimetry (WIP) and adsorption/desorption of nitrogen vapors (77K) method were realized and the comprehensive interpretation of the outcomes was done. Absolute permeability, pore diameters size, total surface area from Hg porosimetry were compared with outcomes of nitrogen physical adsorption/desorption method. It enabled extension of pore diameter range into extremely small values. The nitrogen adsorption/desorption method also contributed to porosity values, adding notable volume of the smallest pores. The results from NMR experiments confirmed a complicated porous space structure and showed that total surface area from adsorption/desorption of nitrogen method together with pore space area from Hg porosimetry correlate well with the irreducible water saturation. Laboratory results were combined with well logs (GR) and results of the comprehensive interpretation (PHI) and volumes of mineral components, for instance illite/smectite and kerogen. GEM logging results were also used to improve volume of carbonates in shale gas rocks matrix and organic/inorganic coal. Identification of Fe element was useful in pyrite recognition. Another important factor was including the sedimentological macroscopic description of cores before cutting plugs and geological homogenization of samples and adopting the proper sequence of laboratory experiments to be sure that all properties were determined on the same part of the rock material.

Keywords: *petrophysics, well logging, shale gas formations, mineral composition, reservoir properties*

INTRODUCTION

Unconventional shale gas formation has been the subject of intensive exploration in Poland since the late 1990s. The most promising regions were considered to be sedimentary basins placed along the Teisseyre-Tornquist zone from the north-west to south-east of Poland. The investigations were focused on the Silurian and Ordovician thick shale formation which spread in Poland along the western margin of the East European Platform in the Baltic, Lublin and Podlasie Basins (Kiersnowski 2013; Narkiewicz et al. 2014). Large archive core material and well log data indicating the presence of hydrocarbons after geological research conducted in the 1960s, '70s and '80s were also available and included for reinterpretation. New geological cores acquired from several wells drilled by POGC SA and LOTOS-Petrobaltic SA in recent years confirmed presence of gas in shale formations. New methods of laboratory experiments and methodology of well logging measurements and comprehensive interpretation were applied to possess more and more detailed information (Jarzyna–Wawrzyniak-Guz 2017b). Several scientific elaborations have conducted to recognize Polish shale gas formations and compare them to other world-wide shale plays known from the literature (see e.g. Raport PIG-PIB 2012).

GEOLOGICAL SETTING

The object of the analysis covers two formations, potential resources of unconventional hydrocarbons: the Ja Member of the Silurian Pa Formation and Ordovician Sa Formation. In these formations sedimentation of organic-rich black shales with graptolites as the main fossil started in the Late Llanvirnian reaching Wenlock (Podhalańska 2003). In the analyzed wells the Pa Formation is placed between Pr Fm (lower boundary) and Pe Fm (upper boundary). The lower boundary is marked at the point of clear lithological changes involving the replacement of limestone or marl deposits of the Ordovician series into clay sediments of the Pa Formation. Ja Mb belongs to the lower part of the Pa Fm and is built of black bituminous claystones. It is characterized by high organic matter content; however, it may not ensure large gas reserves since the thickness of this bed does not exceed 12 m (Modliński et al. 2006). The lower boundary of the Sa Formation runs on the limestone Ko Fm within Llanvirnian and Llandeilian series while the upper boundary is set by the marl and shale Pr Fm within Ashgillian series *(Table 1)*. The lithology is mainly comprised of black, dark grey and grey-greenish bituminous shales. Shales of Sa Fm and Ja Mb are rich in organic matter with the median values of TOC amounting to 3.1 and 3.0 wt.%, respectively. The highest TOC contents recorded in wells in the study area reached 8.5 wt.% in Sa Fm (Jarzyna et al. 2017a, b).

MATERIALS AND METHODS

Selected results of laboratory experiments were collected for the presented study. Results are related to formations, not to boreholes, to form a general description of the Silurian and Ordovician shale plays. Laboratory methods for density and porosity

measurements were pointed out because bulk density and total porosity are values measured in standard well logging.

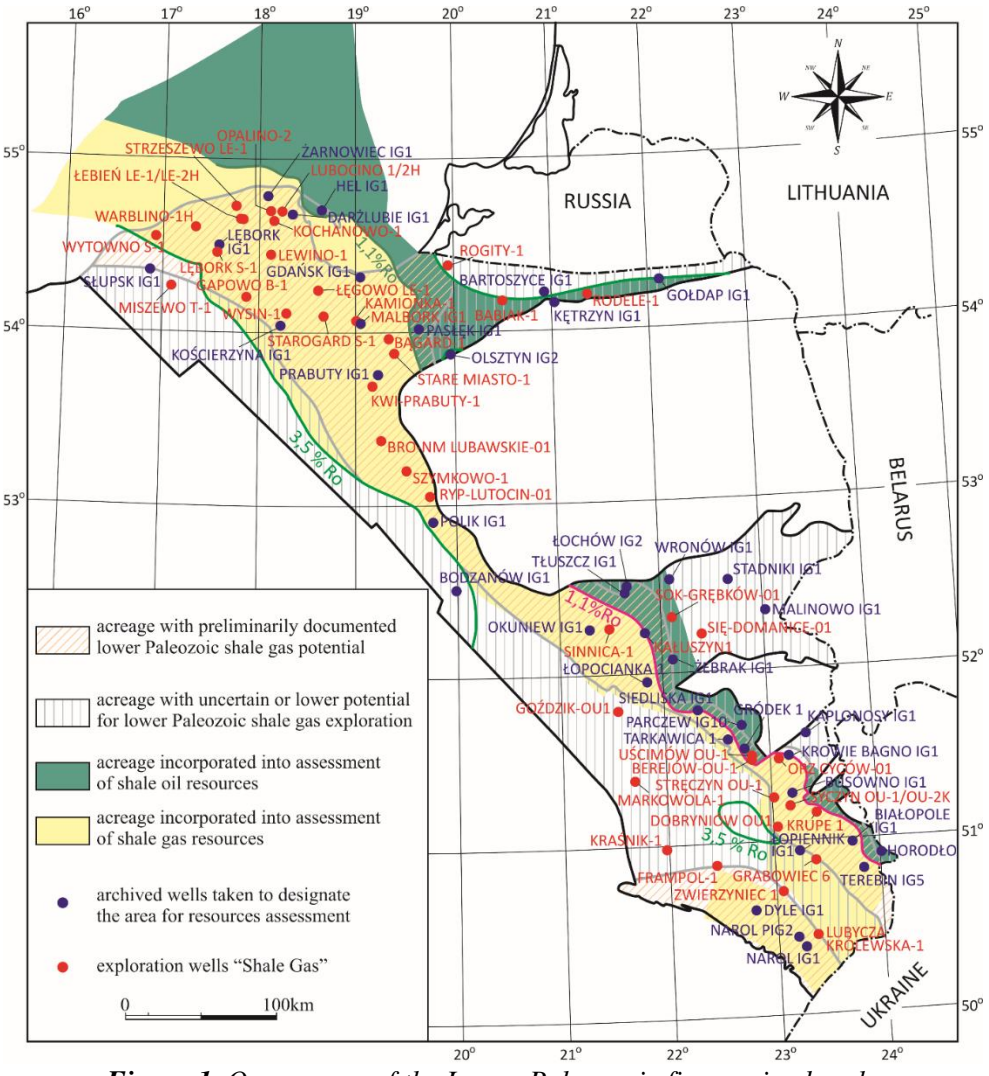

Figure 1. *Occurrence of the Lower Palaeozoic fine-grained rocks potentially accumulating shale gas*
(Kiersnowski 2013, modified)

A great variety of those parameters from the laboratory experiments provided the basis for studying mutual relationships. The list of laboratory measured parameters includes, among others, grain density (GD_{WIP}) and total porosity (Φ_{WIP}) determined by *Water Immersion Porosimetry (Dual-Liquid Porosimetry)* (Kuila et al. 2014;

Topor et al. 2016), bulk density (BD), skeletal density (SD), total pore area (TPA), average pore diameter (APD), effective porosity (Φ_eff) and physical permeability (K) from Hg porosimetry, permeability (K_PDP) and bulk density (BD_PDP) from Pressure Decay Permeability (PDP) method, density (D) from He pycnometry, total (Φ_NMR) and effective porosity (Φ_NMR_eff) together with irreducible water saturation (Sw irr) from NMR experiment. Results of physical adsorption of nitrogen (Rouquerol et al. 2014) were also included in the data set to extend the information from the Hg porosimetry into micropores. On the basis of this method specific surface (S_{BET}) was also determined together with pore volumes in several groups related to small pore diameters. Total organic carbon (TOC) and other characteristic parameters from Rock-Eval pyrolysis (Kotarba et al. 2014) and some petrophysical parameters calculated on the basis of mineralogy and chemical data like the photoelectric absorption index (PEF) or SIGMA were included. Specialist professional equipment was adopted for experiments, such as, AutoPore IV 9500 Micromeritics, PDP Terra Tek Schlumberger Reservoir Laboratory, Quantachrome Autosorb-1C automatic gas adsorption apparatus, Rock-Eval 8 and also some prototype sets for example for water immersion porosimetry.

Table 1

Stratigraphic sequence and lithology of formations in the study area (Baltic Basin)

Geological formation	**Stratigraphy**	**Lithology**
Pe Formation	Silurian, Ludlow, Wenlock	Claystone
Pa Formation	Silurian, Llandovery	Claystone
Ja Member at the foot of Pa Formation	Silurian, Llandovery	Bituminous claystone
Pr Formation	Ordovician, Ashgillian	Marl, Limestone, Claystone
Sa Formation	Ordovician, Caradocian, Llanvirnian	Bituminous claystone, Claystone
Ko Formation	Ordovician, Llanvirnian, Llandeilian	Limestone

RESULTS

In data sets built for boreholes the number of measured quantities was limited and not the same, so comparison could be done only for selected parameters. Well logging results were considered in the full cored depth sections in each borehole. This paper presents results from the Pa formation including the Ja Member at the bottom, the Pr formation built of marls and claystones and the Sa formation. The mineral composition of formations is presented in pie charts *(Figure 2)* showing the

percentages of minerals and groups of minerals: quartz, feldspars, dolomite and ankerite and clay minerals. Pyrite, ankerite, siderite and other minerals including iron element play an important role due their high density in contrast to kerogen and organic matter. The presence of such minerals is also considered from the aspect of shale formation brittleness. Differences in mineral composition between claystone-mudstone Pa formations and bituminous claystones in the Ja Member and Sa formations is distinctly visible.

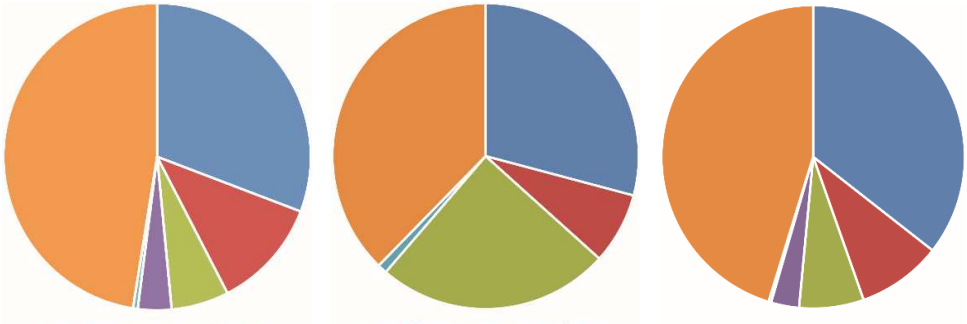

Pa Formation with Ja Member at the bottom; 1–(29.4), 2–(10.0), 3– (5.6), 4–(2.4), 5–(0.7), 6–(52.3)

Pr Formation; 1–(29.15), 2–(7.54), 3–(24.62), 4–(0.00), 5–(1.01), 6–(37.69)

Sa Formation;1–(35.79), 2–(9.02), 3–(6.89), 4–(2.98), 5–(0.28), 6–(45.24)

Figure 2. *Histograms of the mineral composition in the representative depth sections on the basis of XRD mineralogy results, volume percentage: 1–quartz, 2–feldspar, 3–calcite, dolomite and ankerite, 4–pyrite, 5–others including anhydrite, siderite, hematite, halite, fluorite, bassanite, gypsum, galena, 6–sum of clay minerals*

In each of the formations *(Figure 2)* a relatively high quartz volume is observed. The volume of clay minerals is also high, but they are not further differentiated into illite, montmorillonite (smectite), kaolinite or chlorite.

Table 2

Ranges of the compared parameters

	Silurian, Pa Formation with Ja Member; depth: 2850.15–2906.7 m		**Ordovician, Pr Formation; depth: 2907-2914.9 m**		**Ordovician, Sa Formation; depth: 2915–2940.9 m**	
Numer of data	76		11		42	
	min	**max**	**min**	**max**	**min**	**max**
TOC [% wt.]	0.06	7.30	0.16	0.69	0.08	8.5
Bulk density [g/cm3]	2.38	2.70	2.64	2.72	2.38	2.69
Skeletal density [g/cm3]	2.51	2.81	2.76	2.79	2.46	2.81
Material density [g/cm3]	2.52	2.85	2.76	2.79	2.47	2.90
Kerogen volume [v/v]	0.00	0.12	0.00	0.04	0.00	0.18

Ranges of TOC, bulk, skeletal and material densities and kerogen volume (determined from the comprehensive interpretation of well logs) in the Silurian Pa Formation with Ja Member, Pr Formation and Ordovician Pr and Sa Formations are presented in *Table 2* to illustrate variability among stratigraphic formations. A distinct relation is visible between lithology and density. There are also visible changes in bulk density and skeletal density with depth. The decrease of bulk density with increase of kerogen volume and TOC percentage can be observed.

Relationships between skeletal and material density vs TOC in the Sa Formation are presented in *Figure 3*. Dispersion of both densities is visible and from these plots it is difficult to decide which density better describes shale gas formations. The slope of correlation lines is similar but the bulk density in the Sa Formation of the highest TOC content reveals higher values, which means that kerogen is located in pore space.

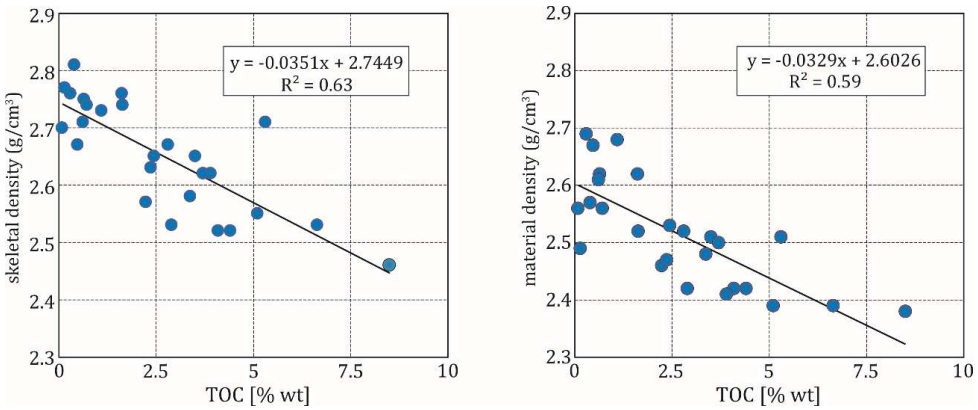

Figure 3

Relationships between skeletal and material density vs TOC in the Sa Formation

Relationships between petrophysical parameters from well logs and results of the comprehensive interpretation: GR anomaly and total porosity – PHI vs. kerogen volume *(Figure 4)* presented separately for the Ja Member and Sa Formation sweet spots show that the intensity of natural radioactivity correlates similarly in both shale gas formations *(Figure 4a)*. Thus, high anomalies in GR may be primary indicators of sweet spots, i.e. places with a higher volume of kerogen. Comparison between PHI and the volume of kerogen shows a higher dispersion of points than previous relationships. PHI presents a similar range of values for both sweet spots. In both formations data are grouped into two parts; in both groups there is a visible increase of kerogen volume with porosity. This indicates kerogen presence in the pore space of the shale formation. For the selected porosity a higher kerogen volume is observed in the Ja Member in comparison to the Sa Formation. The distinct division of Ja Member data into two groups shows that for the same porosity two different volumes of kerogen can be detected. This means that kerogen in the Ja Member is present in

two forms, probably filling partially pore space and as organic matter in the skeleton *(Figure 4b)*.

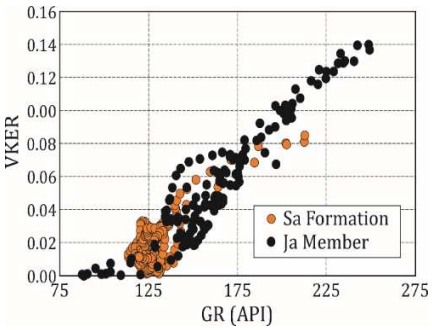

Figure 4a

Relationship between kerogen volume vs. natural radioactivity GR anomaly

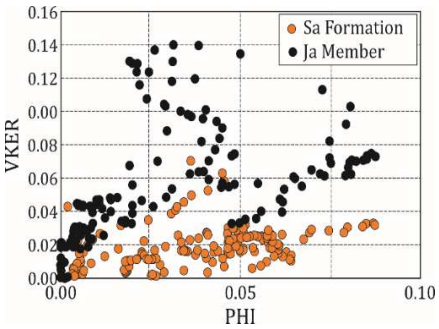

Figure 4b

Relationship between kerogen volume vs. total porosity PHI

Measurements of the low temperature isotherms of nitrogen adsorption (77K) are the basis to determine porous texture parameters of rocks, i.e. specific surface, volume of pores, average pore diameter and pore distributions (Thommes et al. 2015). The low pressure part of the isotherm provides data for microstructure characterization – micropores are filled with porous media at relatively low pressure, based on the Dubinin and Raduszkiewicz theory. In mesopores adsorption is multilayered and at the end capillary condensation takes place (gas is adsorbed in pores as fluid under pressure). Pressure increase causes an increase in the adsorbed medium volume. The method elaborated by Barrett, Joyner and Halenda (BJH) is the mostly used to describe mesopores distribution. Micro- and mesopores influence specific surface which is frequently calculated using Brunauer, Emmet, Teller (BET) equation. Micro- and mespores were also characterized using the Quenched Solid Density Functional method (DFT). Macropores are not very important in specific surface calculations but they are the path for media transport to smaller pores. Pore volume can be simply calculated from the nitrogen adsorption isotherms but the pore size and specific surface determination is based on adopted models. Three examples of adsorption/desorption isotherms and results of their processing are presented *(Figure 5)*. They represent different mudstone-claystone rocks from the Ja Member (a, b, depth: 2896.93 m, BD = 2.39 g/cm^3, Φ_eff = 2.18%, TOC = 5.93%wt), and Sa Formation (c, d, depth: 2920.47 m, BD = 2.97 g/cm^3, Φ_eff = 0.29%, TOC = 2.40%wt and e, f, depth: 2936.85 m, BD = 2.23, Φ_eff = 2.65%, TOC = 2.27%wt). Differences in plots in Figure 5 are distinctly visible. They are partially caused by different mineral composition *(*see *Figure 2)* and variability of bulk density and TOC. Comparison of BJH and DFT curves illustrate the influence of the adopted model for nitrogen adsorption data processing. The most details are revealed in the DFT approach. Hg porosimetry results (poroz.) showed the important role of micro- and mesoporosity in the rocks in study, especially in specific surface determination.

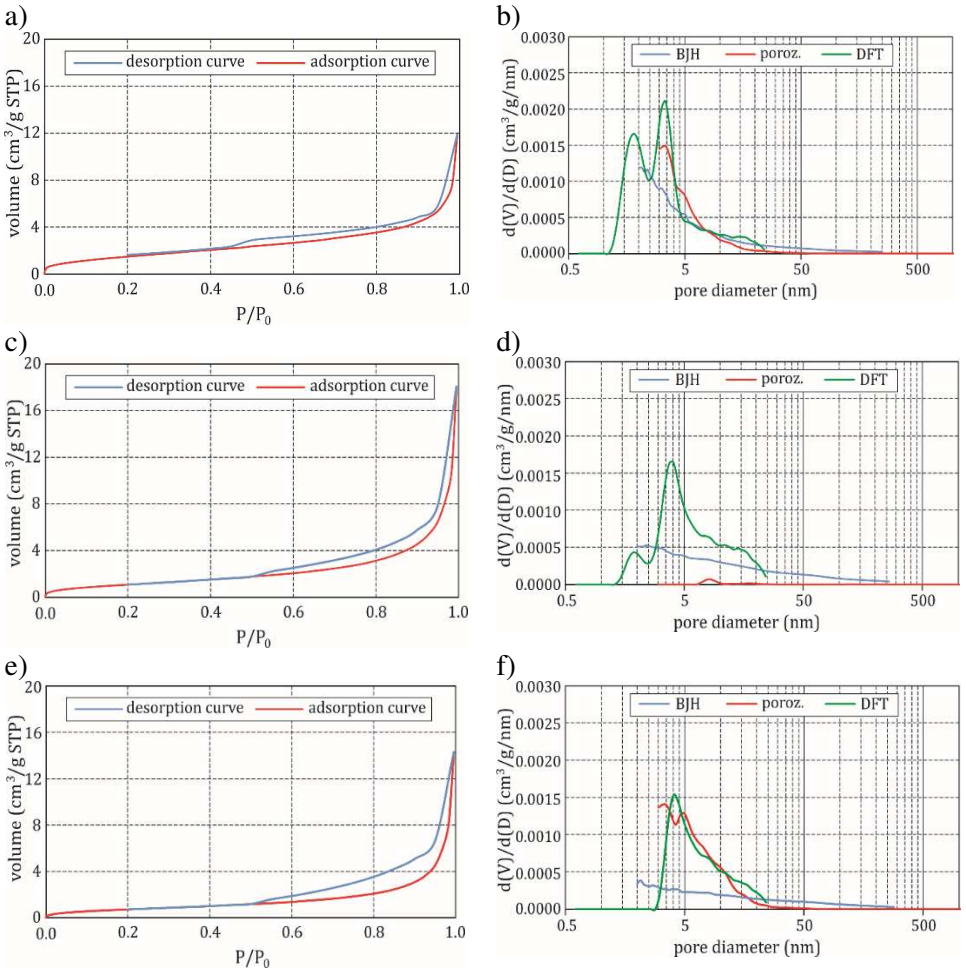

Figure 5

Results of physical adsorption of nitrogen; left plots – adsorption (red) and desorption (blue) curves, right plots – distribution curves, results of processing using Barrett, Joyner and Halenda (BJH) method and DFT method compared to Hg porosimetry result (poroz.)

SUMMARY

As many as possible laboratory techniques and well logging measurements were done to identify mutual relationships between quantities representing petrophysical parameters of shale gas formations. Mineral composition, reservoir properties and geochemical parameters were the basis for sweet spot characterization. Combined results from the complementary methods revealed additional features. Laboratory methods and specific equipment dedicated to shale gas formations investigations were listed along with relevant literature. The same approach was adopted for well logging without including formulas and plots illustrating all mutual relationships.

Examples and references provided the idea of a comprehensive approach to shale gas deposits. A short geological description and depth information was included to provide information on Polish shale gas plays.

ACKNOWLEDGMENTS

Data was allowed by POGC SA, Poland in the MWSSSG Polskie Technologie dla Gazu Łupkowego (2013-2017) project. The authors thank Prof. Leszek Czepirski's research group (AGH UST) for cooperation in the nitrogen adsorption experiments.

REFERENCES

[1] Jarzyna J. A., Bala M., Krakowska P. I., Puskarczyk E., Strzepowicz, A., Wawrzyniak-Guz, K., Wiecław, D., Zietek, J. (2017a). Shale Gas in Poland. In: *Natural Gas*. INTECH, distributed by Internet.

[2] Jarzyna J. & Wawrzyniak-Guz (red) (2017b). *Adaptacja do warunków polskich metodologii wyznaczania sweet spotów na podstawie korelacji pomiarów geofizycznych z rdzeniami wiertniczymi.* Zad. 10. Kraków, GOLDRUK (in Polish).

[3] Kiersnowski H. (2013). Geological Environment of Gas Bearing Shales. In: Nawrocki J. (ed.). *Shale gas as seen by Polish Geological Survey*. Polish Geological Institute, National Research Institute.

[4] Kotarba, M. J., Lewan, M. & Wieclaw, D. (2014). Shale gas and oil potential of Lower Palaeozoic strata in the Polish Baltic Basin by Hydrous Pyrolysis. Presented at the *Fourth EAGE Shale Workshop. Shales: What do they have in common?* 6–9 April, 2014. Porto, Portugal.

[5] Kuila U., McCarty D. K., Derkowski A., Fischer T. B., Prasad, M. (2014). Total porosity measurement in gas shales by the water immersion porosimetry (WIP) method. *Fuel*, 117, pp. 1115–1129.

[6] Modliński Z., Szymański B., Teller L. (2006). The Silurian lithostratigraphy of the Polish part of the Peri-Baltic Depression (N Poland). *Przegląd Geologiczny*, 54 (9), pp. 787–796 (in Polish).

[7] Narkiewicz M., Maksym A., Malinowski M., Grad M., Guterch A., Petecki Z., Probulski J., Janik T., Majdański M., Środa P., Czuba W., Gaczyński E., Jankowski L. (2014). Transcurrent nature of the Teisseyre–Tornquist Zone in Central Europe: results of the POLCRUST-01 deep reflection seismic profile. *International Journal of Earth Sciences*, 104, pp. 775–796.

[8] Podhalańska T. (2003). Late Ordovician to Early Silurian transition and the graptolites from Ordovician/Silurian boundary near the SW rim of the East European Craton (northern Poland). *Series Geological Correlation*, 18, pp. 165–172.

[9] Raport PIG-PIB (2012). Ocena zasobów wydobywanych gazu ziemnego i ropy naftowej w formacjach łupkowych dolnego paleozoiku w Polsce (basen bałtycko – podlasko – lubelski). *Raport pierwszy*, PIG-PIB Warszawa (in Polish).

[10] Rouquerol, F., Rouquerol, J., Sing, K. S. W., Llewellyn, P. Maurin, G. (2014). *Adsorption by Powders and Porous Solids: Principles, Methodology and Applications*. Academic Press.

[11] Thommes M., Kaneko K., Neimark A. V., Olivier J. P., Rodriguez-Reinoso F., Rouquerol J. & W. Sing K. S. (2015). Physisorption of gases, with special reference to the evaluation of surface area and pore size distribution (IUPAC Technical Report), *Pure and Applied Chemistry*, 87 (9–10), pp. 1052–1069.

[12] Topor T., Derkowski A., Utpalendu K., Fischer T. B., McCarty D. K. (2016). Dual Liquid Porosimetry – porosity measurement technique for oil- and gas-shales. *Fuel*, 183, pp. 537–549.

Geosciences and Engineering, Vol. 6, No. 9 (2018), pp. 19–31.

APPLICATION OF OPTIMUM WEIGHTS IN GEOPHYSICAL DATA INVERSION

DEZSŐ DRAHOS[1]–ATTILA GALSA[1]–ÁKOS GYULAI[2]–
TAMÁS ORMOS[2]–MIHÁLY DOBRÓKA[2]

[1]*Department of Geophysics and Space Science, Eötvös Loránd University*
[2]*Department of Geophysics, University of Miskolc*

Abstract: One of the most serious problems in joint inversion is the selection of the particular weight factors that control the correct contribution of individual data sets to the joint objective function. These weight factors are necessary input factors of joint inversion but generally they are unknown. A method is presented and applied in which there is no need to know these weight factors in advance. The maximum likelihood method is used so that the optimization is done not only with respect to the model parameters but also to the standard deviations of the data. The application is demonstrated by joint inversion of various erroneous data sets. Several simulated joint inversion problems such as (1) toy examples, (2) refraction seismic data and (3) geoelectrical measurements were studied. The inversion results show the applicability and effectiveness of the method.

Keywords: *joint inversion, optimum weights, maximum likelihood method*

INTRODUCTION

The determination of data weights is a crucial point in the inversion procedure, especially in joint inversion. In joint inversion the data from different type measurements relating to the same geological site are inverted; thus, one common objective function must be compiled. The common objective function depends on the single objective functions. The conventional strategy is to add the objective functions of the different data sets, which will be the joint objective function. One problem is that the magnitudes and the dimensions are different, and the data errors of the different data sets can also be dissimilar. In order to overcome these difficulties optimum weights should be selected. Dobróka et al. [1] and De Nardis et al. [2] divided the difference of the measured and computed values by the measured one. This solves the magnitude and dimension problems, but a further problem is the unlike errors of different data sets. Therefore the component objective functions should be multiplied by weight factors to give the correct contribution to the determination of the model parameters. Juliá et al. [3] introduced the 'influence parameter' p, which is responsible for the correct contribution between the seismic receiver function and the dispersion data sets. A similar method was applied by Mota and Monteiro Santos [4]

where seismic velocity data and resistivity data were inverted jointly in a hydrogeological survey. Here, the weights α and 1-α were applied. However, there is still no general rule for the determination of the weight factors even though the result depends on them. Treitel and Lines [5] mentioned this as a big unsolved problem of joint inversion. A new method is proposed here where the optimum weight factors are computed during the inversion procedure.

APPLIED METHOD

The method of optimum weights is presented in [6] in detail. Let us consider two different types of geophysical measurements. The sets of data and the corresponding sets of theoretical functions relating to the model are denoted by the vectors $\mathbf{d_1}$, $\mathbf{g_1}(\mathbf{m})$ and $\mathbf{d_2}$, $\mathbf{g_2}(\mathbf{m})$, respectively. The dimensions of the vectors are n_1 and n_2. The unknown model parameters to be determined are the components of the vector $\mathbf{m}$. The relation between the measured data and the model parameters are

$$\mathbf{d_1} = \mathbf{g_1}(\mathbf{m}) + \mathbf{e_1}, \tag{1}$$

and

$$\mathbf{d}_2 = \mathbf{g}_2(\mathbf{m}) + \mathbf{e}_2, \tag{2}$$

where $\mathbf{e_1}$ and $\mathbf{e_2}$ denote the error vectors for task 1 and 2, respectively. Error vectors include independent random numbers assuming normal distribution with zero expected values. The standard deviation of $\mathbf{e_1}$ and $\mathbf{e_2}$ is σ_1 and σ_2, respectively.

The conventional form of the joint objective function with the norm L_2 is

$$\lambda = w_1 \sum_{i=1}^{n_1} \left(d_{1,i} - g_{1,i}(\mathbf{m})\right)^2 + w_2 \sum_{j=1}^{n_2} \left(d_{2,j} - g_{2,j}(\mathbf{m})\right)^2, \tag{3}$$

where w_1 and w_2 denote the weight factors of the geophysical measurements, i and j are the index of the measuring data point.

Applying the maximum likelihood principle [7] for the two data sets separately, the likelihood functions l_1 and l_2 should be maximized with respect to $\mathbf{m}$. Supposing the uncorrelated normal distribution of the errors for the two data sets, the form of the likelihood functions for task 1 is

$$l_1 = f_1(d_{1,1}, \mathbf{m}) f_1(d_{1,2}\mathbf{m}) ... f_1(d_{1,n_1}, \mathbf{m}), \tag{4}$$

where

$$f_1(d_{1,i}, \mathbf{m}) = \frac{1}{\sqrt{2\pi}\sigma_1} \exp\left[-\frac{1}{2\sigma_1^{\,2}} \left(d_{1,i} - g_{1,i}(\mathbf{m})\right)^2 \right], \tag{5}$$

and the likelihood function for task 2 is

$$l_2 = f_2(d_{2,1},\mathbf{m}) f_2(d_{2,2}\mathbf{m})...f_2(d_{2,n_2},\mathbf{m}), \tag{6}$$

where

$$f_2(d_{2,j},\mathbf{m}) = \frac{1}{\sqrt{2\pi}\sigma_2}\exp\left[-\frac{1}{2\sigma_2{}^2}\left(d_{2,j} - g_{2,j}(\mathbf{m})\right)^2\right] \tag{7}$$

[7]. By maximizing l_1 and l_2 functions, two independent estimations of the measurement, $\mathbf{m_1}$ and $\mathbf{m_2}$ will be calculated. However, the main goal of the joint inversion is to determine one common estimation of the model parameters, $\mathbf{m}$. Therefore, the product of $l = l_1 l_2$ should be maximized,

$$\begin{aligned} l = &\frac{1}{(\sqrt{2\pi})^{n_1+n_2}\sigma_1{}^{n_1}\sigma_2{}^{n_2}}\cdot \\ &\cdot\exp\left[-\frac{1}{2\sigma_1{}^2}\sum_{i=1}^{n_1}\left(d_{1,i} - g_{1,i}(\mathbf{m})\right)^2 - \frac{1}{2\sigma_2{}^2}\sum_{j=1}^{n_2}\left(d_{2,j} - g_{2,j}(\mathbf{m})\right)^2\right]. \end{aligned} \tag{8}$$

The usual way to solve *Equation (8)* is to minimize the negative logarithm of l,

$$\lambda = -\ln l, \tag{9}$$

which is

$$\begin{aligned} \lambda = &\frac{n_1+n_2}{2}\ln(2\pi) + n_1\ln\sigma_1 + n_2\ln\sigma_2 + \\ &+\frac{1}{2\sigma_1{}^2}\sum_{i=1}^{n_1}\left(d_{1,i} - g_{1,i}(\mathbf{m})\right)^2 + \frac{1}{2\sigma_2{}^2}\sum_{j=1}^{n_2}\left(d_{2,j} - g_{2,j}(\mathbf{m})\right)^2. \end{aligned} \tag{10}$$

When the standard deviations σ_1 and σ_2 are known, only the two last terms of *Equation (10)* need to be minimized and in this case the weights of the two separate objective functions are

$$w_1 = \frac{1}{\sigma_1{}^2} \quad \text{and} \quad w_2 = \frac{1}{\sigma_2{}^2}. \tag{11}$$

However, the standard deviation of the measurements is generally unknown, thus the minimization must be done with respect to σ_1 and σ_2, too. In order to calculate the standard deviations, the assumption of

$$\frac{\partial\lambda}{\partial\sigma_1} = 0 \quad \text{and} \quad \frac{\partial\lambda}{\partial\sigma_2} = 0 \tag{12}$$

must be fulfilled. After some algebra we get

$$\sigma_1^{\,2} = \frac{1}{n_1}\sum_{i=1}^{n_1}\left(d_{1,i} - g_{1,i}(\mathbf{m})\right)^2 \quad \text{and} \quad \sigma_2^{\,2} = \frac{1}{n_2}\sum_{j=1}^{n_2}\left(d_{2,j} - g_{2,j}(\mathbf{m})\right)^2 . \quad (13)$$

By substituting *Equation (13)* into *Equation (10)* we get for the objective function λ after neglecting the constant terms of the equation,

$$\lambda = \frac{n_1}{2}\ln\left[\frac{1}{n_1}\sum_{i=1}^{n_1}\left(d_{1,i} - g_{1,i}(\mathbf{m})\right)^2\right] + \frac{n_2}{2}\ln\left[\frac{1}{n_2}\sum_{j=1}^{n_2}\left(d_{2,j} - g_{2,j}(\mathbf{m})\right)^2\right]. \quad (14)$$

Equation (14) has already been minimized with respect with σ_1 and σ_2, and the objective function depends only on the model parameters. Thus, the task is to determine model parameters **m** by the minimization of λ. In the view of **m**, standard deviations σ_1 and σ_2 can be calculated using *Equation (13)*, thus the optimum weights of different measurements are determined for joint inversion.

NUMERICAL EXAMPLES

Toy examples

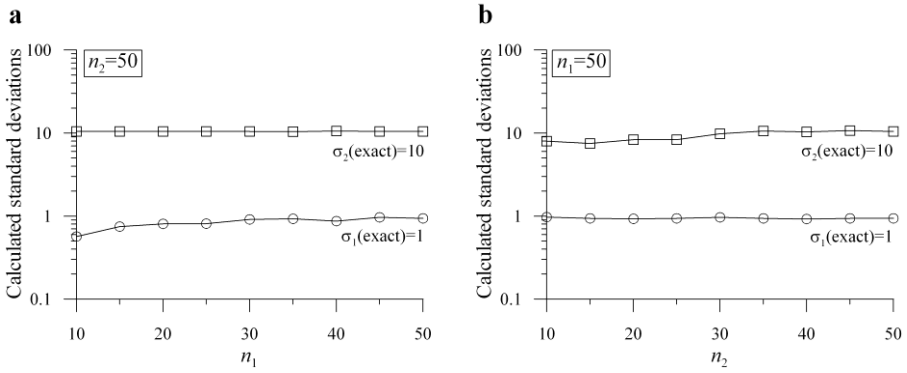

Figure 1. *Calculated standard deviations as a function of the numbers of data sets, n_1 and n_2. The exact values of the standard deviations are σ_1(exact) = 1 and σ_2(exact) = 10, (a) n_1 increases from 10 to 50 and n_2 = 50 (fixed); (b) n_2 increases from 10 to 50 and n_1 = 50 (fixed)*

Numerical calculations without geophysical meaning were carried out to check the accuracy of the method presented in part 2. Linear direct problems like those in *Equations (1)* and *(2)* were generated in which the exact values of the five model parameters were $m_1 = 1.0$, $m_2 = 2.0$, $m_3 = 3.0$, $m_4 = 4.0$ and $m_5 = 5.0$. Data sets $\mathbf{d_1}$ and $\mathbf{d_2}$ were created using $\mathbf{e_1}$ and $\mathbf{e_2}$ error numbers with normal distributions of zero expected values and standard deviations of $\sigma_1 = 1$ and $\sigma_2 = 10$, respectively. *Figure 1a* shows how the estimated values of the standard deviations tend to the exact values as the number of data set 1 increases from $n_1 = 10$ to 50. Meanwhile, the number of

data set 2 was fixed, $n_2 = 50$. *Figure 1b* depicts the case when the number of the data set is fixed at $n_1 = 50$ and n_2 ranges between 10 and 50. This task illustrates well that the number of the data sets facilitates the accurate estimation of the individual standard deviations of the data sets.

In the next example the standard deviations are $\sigma_1 = 1$ and $\sigma_2 = 10$, and then $\sigma_1 = 1$ and $\sigma_2 = 100$. In Example 2 the number of data were $n_1 = n_2 = 50$. Since different tasks can depend on different model parameters, three cases were distinguished. In case A of Ex. 2, both task 1 and task 2 depend on all five model parameters. In case B of Ex. 2, task 1 depends on m_1, m_2, m_3 and m_4, while task 2 depends on m_2, m_3, m_4, and m_5. In case C of Ex. 2 task 1 depends only on m_1, m_2 and m_3, while task 2 depends on m_3, m_4, and m_5, so the only one common model parameter is m_3.

Table 1 summarizes (1) the exact and the estimated values of the standard deviation of tasks 1 and 2, (2) the exact and the estimated values of the model parameters and (3) their standard deviations $\sigma(m_i)$. Case A illustrates that both the model parameters and standard deviations σ_1, σ_2 are estimated with high accuracy, independent of whether $\sigma_2 = 10$ or $\sigma_2 = 100$. Case B represents the situation when m_5 is independent of task 1. As a result of that the estimation for m_5 is much worse and $\sigma(m_5)$ increased, especially in the case when $\sigma_2 = 100$. In case C of Ex. 2, task 1 having low standard deviation is sensitive only to the model parameters m_1, m_2 and m_3, thus the estimation for m_4, and m_5 and their standard deviations is quite poor, especially when $\sigma_2 = 100$. In conclusion, the quality of the estimation does not lower for the model parameters which depend on task 1 with low standard deviation. In other words, they are independent of the standard deviation of task 2, because task 1 ensures the high quality solution. The decline in the quality appears only when model parameters are independent of task 1.

Table 1. *Joint inversion results for task 1 and 2 in cases A, B and C (see text for details). The exact and the estimated standard deviations for task 1 and 2; the exact and estimated model parameters and their standard deviations for $\sigma_1 = 1$ and $\sigma_2 = 10$, and then $\sigma_1 = 1$ and $\sigma_2 = 100$. Common model parameters in cases A, B and C are denoted by red. Number of data sets is $n_1 = n_2 = 50$*

Case A	$\mathbf{g}_1(m_1,m_2,m_3,m_4,m_5)$			$\mathbf{g}_2(m_1,m_2,m_3,m_4,m_5)$	
	σ_1(exact) = 1.0			σ_2(exact) = 10.0	
	σ_1(est) = 1.010			σ_2(est) = 10.648	
m(exact)	1.0	2.0	3.0	4.0	5.0
m(est)	0.966	1.947	2.957	4.050	5.061
σ(**m**)	0.037	0.046	0.039	0.038	0.040
	σ_1(exact) = 1.0			σ_2(exact) = 100.0	
	σ_1(est) = 1.010			σ_2(est) = 96.48	
m(exact)	1.0	2.0	3.0	4.0	5.0
m(est)	0.968	1.974	2.965	4.025	5.043
σ(**m**)	0.042	0.051	0.044	0.043	0.045

Case B	$\mathbf{g}_1(m_1,m_2,m_3,m_4)$			$\mathbf{g}_2(m_2,m_3,m_4,m_5)$	
	σ_1(exact) = 1.0			σ_2(exact) = 10.0	
	σ_1(est) = 1.069			σ_2(est) = 10.322	
m(exact)	1.0	2.0	3.0	4.0	5.0
m(est)	1.056	1.986	3.012	3.935	5.074
σ(**m**)	0.039	0.043	0.040	0.039	0.162
	σ_1(exact) = 1.0			σ_2(exact) = 100.0	
	σ_1(est) = 1.045			σ_2(est) = 99.498	
m(exact)	1.0	2.0	3.0	4.0	5.0
m(est)	1.076	1.943	2.968	3.994	5.161
σ(**m**)	0.038	0.042	0.040	0.038	1.561

Case C	$\mathbf{g}_1(m_1,m_2,m_3)$			$\mathbf{g}_2(m_3,m_4,m_5)$	
	σ_1(exact) = 1.0			σ_2(exact) = 10.0	
	σ_1(est) = 1.009			σ_2(est) = 8.935	
m(exact)	1.0	2.0	3.0	4.0	5.0
m(est)	0.967	1.924	3.109	4.128	4.657
σ(**m**)	0.035	0.037	0.037	0.294	0.301
	σ_1(exact) = 1.0			σ_2(exact) = 100.0	
	σ_1(est) = 1.004			σ_2(est) = 93.23	
m(exact)	1.0	2.0	3.0	4.0	5.0
m(est)	0.983	2.007	3.003	6.637	2.360
σ(**m**)	0.035	0.037	0.037	3.065	3.132

Refraction seismics

Theoretical refraction seismic data sets were generated to test the joint inversion method presented above in geophysical survey. The model consists of two horizontal layers separated by a horizontal boundary at the depth of h = 5 m *(Figure 2)*. In the upper layer the exact seismic velocity is v_1 = 300 m/s, in the lower layer is v_2 = 600 m/s. Two refraction seismic measurements were done and the measured data sets are $\mathbf{d}_1$ and $\mathbf{d}_2$. The first measurement includes n_1 = 20 data, geophones were located at varying distances from the shot point x_1 = 1 m, 2 m, …, 20 m. The second measurement includes n_2 = 60 data at a distance of x_2 = 2 m, 4 m, …, 120 m. It is assumed that the standard deviations of the two measurements are different, measurement 1 has good quality data (σ_1 = 1 ms), but measurement 2 has bad quality data (σ_2 = 5 ms).

The theoretical travel time t is

$$t = \begin{cases} \dfrac{x}{v_1} & \text{if} \quad x < x_c \\ \dfrac{x}{v_2} + 2h\dfrac{\sqrt{v_2^2 - v_1^2}}{v_1 v_2} & \text{if} \quad x \geq x_c \end{cases} \tag{15}$$

where x_c is the crossover distance,

$$x_c = 2h\sqrt{\frac{v_2 + v_1}{v_2 - v_1}} \tag{16}$$

[8]. This means for the given geophysical situation that the refraction wave overtakes the direct wave at the distance of $x_c = 17.3$ m. In other words, measurement 1 includes only 2 geophones in the second part of the travel time curve *(Figure 2)*. Error data were produced with normal distribution and zero expected values.

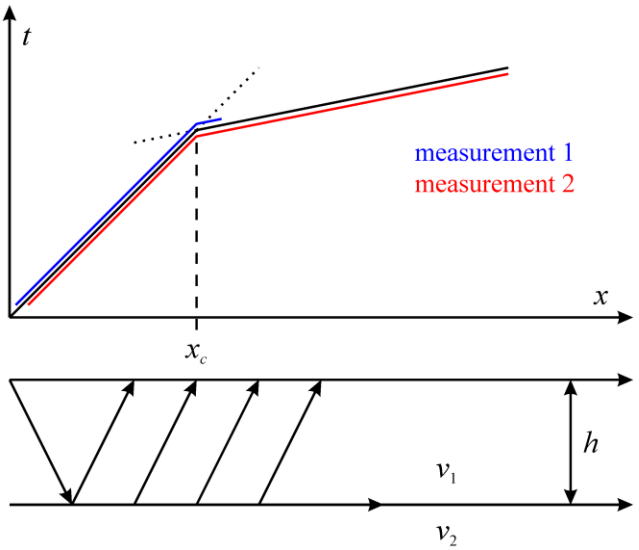

Figure 2. *Illustration of refraction seismic measurements and ray paths in horizontal, two-layered model. Blue and red colors in travel time graph denote the locations of measurement 1 and 2, respectively*

Four types of the inversion procedures were accomplished:

- Case A: inversion for measurement 1.
- Case B: inversion for measurement 2.
- Case C: joint inversion, measurement 1 and 2 are supposed to have equal standard deviations, weight factors in *Equation (3)* are the same, $w_1 = w_2 = 1$.
- Case D: joint inversion, measurement 1 and 2 are supposed to have different standard deviations, they are computed by *Equation (13)*.

Table 2 lists the exact and the estimated standard deviations of measurement 1 and 2 (σ_1 and σ_2), the exact and the estimated model parameters (v_1, v_2 and h) and their estimated standard deviations ($\sigma(\mathbf{m})$). Case A has a good estimation for v_1, but data are more insensitive to v_2 and h. We underline that data set $\mathbf{d_1}$ includes only 2 points after the crossover ($x_1 = 18$ m and 20 m). Case B yields a medium quality estimation for the model parameters due to the higher standard deviation of measurement 2 ($\sigma_2 = 5$ ms).

For case C the uniform standard deviation of measurement 1 and 2 is 3.62 ms, which is situated between the exact values of $\sigma_1 = 1$ ms and $\sigma_2 = 5$ ms. The estimation for the model parameters is good. In case D the estimated standard deviations reflect the exact values (0.99 ms and 5.65 ms), the estimated standard deviation of the model parameters are less than in case C, thus model parameters are closer to the exact values. In conclusion, the estimation of the standard deviations and the model parameters is the most adequate in case D, where the geophysical measurements are treated with their own weights, and these optimum weights are estimated during the joint inversion procedure.

Table 2. *Results of different inversion types of refraction seismic data sets in cases A, B, C and D (see text for details). Number of the two data sets (n_1, n_2), exact and estimated standard deviation of measurements (σ_1, σ_2), exact and estimated model parameters (v_1, v_2, h) and their estimated standard deviations ($\sigma(m)$) are listed*

Case A	**Inversion for measurement 1**		
	$n_1 = 20$	$n_2 = 0$	
	σ_1(exact) = 1 ms		
	σ_1(est) = 0.99 ms		
Model parameters	v_1 [m/s]	v_2 [m/s]	h [m]
m(exact)	300	600	5
m(est)	300	417	3.28
σ(**m**)	2.0	68.0	0.99

Case B	**Inversion for measurement 2**		
	$n_1 = 0$	$n_2 = 60$	
		σ_2(exact) = 5 ms	
		σ_2(est) = 5,60 ms	
Model parameters	v_1 [m/s]	v_2 [m/s]	h [m]
m(exact)	300	600	5
m(est)	287	590	4,51
σ(**m**)	19,5	8,7	0,49

Case C	**Joint inversion with uniform weights**		
	$n_1 = 20$	$n_2 = 60$	
	σ_1(exact) = 1 ms	σ_2(exact) = 5 ms	
	σ_1(est) = 3.62 ms	σ_2(est) = 3.62 ms	
Model parameters	v_1 [m/s]	v_2 [m/s]	h [m]
m(exact)	300	600	5
m(est)	293	590	4.63
σ(**m**)	8.8	7.2	0.30

Case D	**Joint inversion with optimum weights**		
	$n_1 = 20$		$n_2 = 60$
	σ_1(exact) = 1 ms		σ_2(exact) = 5 ms
	σ_1(est) = 0.99 ms		σ_2(est) = 5.65 ms
Model parameters	v_1 [m/s]	v_2 [m/s]	h [m]
m(exact)	300	600	5
m(est)	300	594	4.92
σ(**m**)	2.1	5.5	0.12

Vertical electric sounding

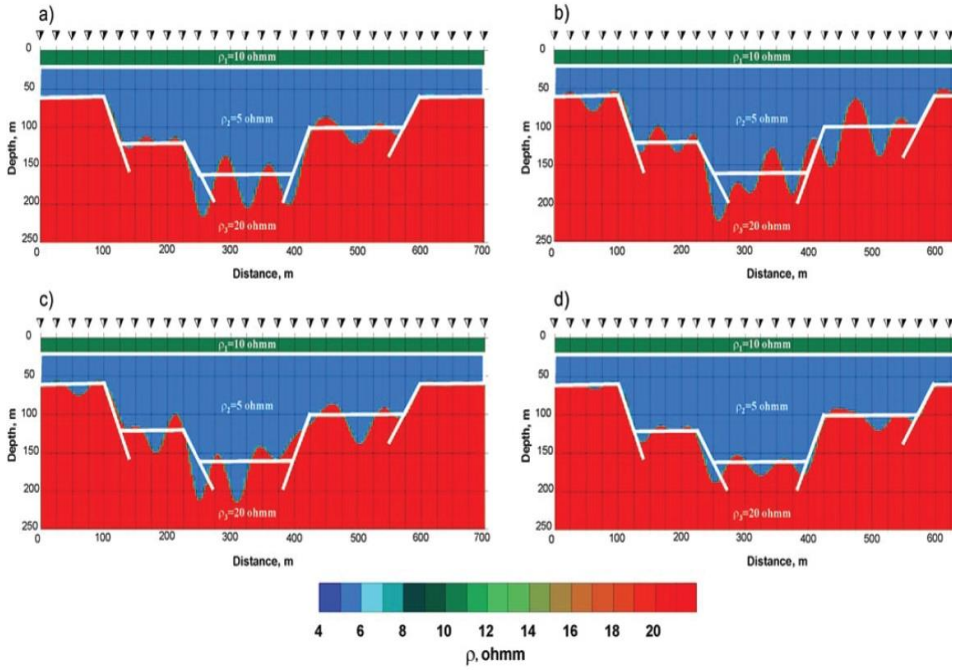

Figure 3. *Graphical solution of the four inversion types, (a) case A – inversion of parallel measurements, (b) case B – inversion of perpendicular measurements, (c) case C – joint inversion with equal weights and (d) case D – joint inversion with individual weights (see text for details). Coloring shows the inverted resistivity distribution, white lines denote the exact layer boundaries. The midpoints of VES measurements are marked by triangles on the surface* [9]

Theoretical vertical electric sounding (VES) data sets were generated to test the optimum weights method by using another inversion procedure [9]. A two-dimensional, three-layered model was built in which only the upper layer was horizontal *(Figure 3)*. From the model parameters the thickness of the upper layer h_1 = 40 m and the

resistivity of the layers $\rho_1 = 10$ Ωm (upper), $\rho_2 = 5$ Ωm, and $\rho_3 = 20$ Ωm (lower) were fixed during the inversion. The only unknown parameter was the position of the laterally varying second layer boundary.

In order to determine the depth of the second layer boundary $h_2(x)$, the direct solution of VES measurements was computed theoretically. 29 VES measurements were simulated both parallel and perpendicular to the section ($n_{par} = n_{per} = 29$). One VES measurement consisted of 19 VES points with different AB electrode distances in both parallel and perpendicular directions, $n_1 = n_2 = 19$, respectively. The midpoints of the Schlumberger array are denoted in *Figure 3* by triangles. The error-free direct solutions were computed by a three-dimensional FD numerical code [10]. In order to simulate a realistic measurement, error with normal distribution and zero expected value was added to the error-free solution. The amplitudes of the error were 2% parallel and 4% perpendicular to the section, which corresponds to $\sigma_1 = 0.00860$ and $\sigma_2 = 0.01703$ on the logarithmic scale, respectively.

Series expansion method was applied to invert the depth of the second layer boundary and determine it between one-dimensional sounding points. Fourier series were applied to approximate the boundary,

$$h_2(x) = \sum_{q=-Q}^{Q} B_q \Phi_q(x), \tag{17}$$

where Φ and B denote the sine and cosine basis functions and the expansion coefficients, respectively, and x is the coordinate parallel with the section. $Q = 11$ was used as a maximum degree of the basis functions; thus, 23 model parameters had to be determined during the inversion,

$$\mathbf{m} = \left(B_{-11}, B_{-10}, ..., B_{11}\right), \tag{18}$$

while other model parameters (h_1, ρ_1, ρ_2 and ρ_3) were supposed to be known.

Inversion procedure can be completed for the parallel and the perpendicular VES measurements both separately and jointly. The objective function to be minimized is

$$\lambda_1 = \sum_{j=1}^{n_{par}} \sum_{i=1}^{n_1} \left[\log \rho_{a1,i,j}^{(M)} - \log \rho_{a1,i,j}^{(T)}(\mathbf{m})\right]^2 \tag{19}$$

for the parallel measurements, and

$$\lambda_2 = \sum_{j=1}^{n_{per}} \sum_{i=1}^{n_2} \left[\log \rho_{a2,i,j}^{(M)} - \log \rho_{a2,i,j}^{(T)}(\mathbf{m})\right]^2 \tag{20}$$

for the perpendicular measurements. In *Equations (19)* and *(20)* L_2 norm is applied to calculate the difference between the logarithm of the measured ($\rho_{a1,i,j}^{(M)}$) and calculated theoretical ($\rho_{a1,i,j}^{(T)}$) apparent resistivity data, where *j* and *i* denote the index of the VES measurements and the AB distances within one VES measurement, respectively.

Joint inversion can be accomplished in the conventional manner, when equal weights are supposed for the two directions. Thus the joint objective function to be minimized is $\lambda_1+\lambda_2$. However, using optimum weights for parallel and perpendicular VES measurements the joint objective function is

$$\lambda = \frac{n_1 n_{par}}{2} \ln\left(\frac{1}{n_1 n_{par}}\lambda_1\right) + \frac{n_2 n_{per}}{2} \ln\left(\frac{1}{n_2 n_{per}}\lambda_2\right) \tag{21}$$

based on *Equation (14)*.

Similarly to part 3.2, four types of inversion were done to determine Fourier series basis function and calculate the depth of the second layer boundary $h_2(x)$:

- Case A: inversion for parallel measurements *[Equation (19)]*;
- Case B: inversion for perpendicular measurements *[Equation (20)]*;
- Case C: joint inversion using equal weights ($\lambda = \lambda_1 + \lambda_2$);
- Case D: joint inversion using optimum weights *[Equation (21)]*.

Figure 3 displays the four solutions obtained from the different inversion types. It can be established qualitatively that case D shows the minimal discrepancy between the theoretical (white line) and the inverted (blue–red boundary) layer boundary. *Table 3* shows quantitatively the data and model distances of the four inversion types. The data distance is the standard deviation of the data based on the difference between the logarithmic measured and theoretical apparent resistivity values. Data distance can be calculated for parallel (data distance 1) and perpendicular (data distance 2) VES measurements. Model distance gives the standard deviation of the depth of the second layer boundary based on the difference between the exact and the inverted solution of $h_2(x)$. *Table 3* highlights that data distance 1 and 2 reflect the relative amplitude of the error added to the error-free direct solution in parallel (2%) and perpendicular (4%) directions. Model distance should be understood as a quality-control factor of the inversion considering the unknown parameter $h_2(x)$. If only the perpendicular VES measurements with high errors are used for inversion (case B) the estimated solution approximates poorly the exact one. If the parallel VES measurements with low error are used for inversion (case A) the estimated solution is better. Applying all measurements with equal weights results in a medium quality solution, because bad quality data infected the good data. The best solution for $h_2(x)$ was served by the optimum weight method, which used both parallel and perpendicular VES data with their individual weights.

Table 3. *Relative discrepancy between the calculated and exact apparent resistivity data for VES measurements parallel (data distance 1) and perpendicular (data distance 2) to the two-dimensional section for the four inversion types. Relative model distance between the calculated and exact depth of the second layer boundary*

Case	Inversion type	Data distance 1	Data distance 2	Model distance
A	Data set 1 (parallel)	1.86%	–	5.50%
B	Data set 2 (perpendicular)	–	3.74%	9.40%
C	Joint inversion with equal weights	1.92%	3.76%	7.45%
D	Joint inversion with optimum weights	1.86%	3.77%	3.63%

CONCLUSIONS

In the optimum weight method the Maximum Likelihood principle is taken into consideration. Optimization of the joint objective function relates not only to the unknown model parameters **m** but is extended also to the unknown standard deviations. This is in accordance with the Maximum Likelihood principle, which asserts that the probability of observed data **d** is made as large as possible. The method can be regarded as the generalization of the L_2 norm inversion technique. It is important to note that the data sets should be uncorrelated. In this paper the method was tested by simulated data, such as inversion of toy examples, refraction seismic data and VES measurements with combination of series expansion method. The inversion results show the effectiveness and the accuracy of the optimum weight inversion method.

REFERENCES

[1] Dobróka, M., Gyulai, Á., Ormos, T., Csókás, J., Dresden, L. (2011). Joint inversion of seismic and geoelectric data recorded in an underground coal mine. *Geophysical Prospecting*, 39, pp. 643–665.

[2] De Nardis, R., Cardarelli, E., Dobróka, M. (2005). Quasi 2D hybrid joint inversion os seismic and geoelectric data. *Geophysical Prospecting*, 55/5, pp. 705–716.

[3] Juliá, J., Ammon, C., Herrmann, R. B., Correig, A. M. (2002). Joint inversion of receiver function and surface wave dispersion observations. *Geophys. J. Inter.*, 143, pp. 99–112.

[4] Mota, R., Monteiro dos Santos, F. A. (2006). 2D sections of porosity and water saturation percent from combined resistivity and seismic surveys for hydrogeologic studies. *The Leading Edge*, 25/6, pp. 735–737.

[5] Treitel, S., Lines, R. (1999). Past, present and future of geophysical inversion – a Y2K analysis. *CREWES Research Report*, 11, pp. 13–20.

[6] Drahos, D. (2008). Determining the objective function for geophysical joint inversion. *Geophys. Transactions*, 45/3, pp. 105–121.

[7] Menke, W. (1989). *Geophysical Data Analysis: Discrete Inverse Theory*. New York: Academic Press, p. 289.

[8] Lowrie, W. (2007). *Fundamentals of Geophysics.* Second Edition. Cambridge: Cambridge Univ. Press, p. 381.

[9] Drahos, D., Gyulai, Á., Ormos, T., Dobróka, M. (2011). Automated weighting joint inversion of geoelectric data over a two dimensional geologic structure. *Acta Geod. Geoph. Hung.*, 46/3, pp. 309–316.

[10] Spitzer, K. (1995). A 3-D finite-difference algorithm for DC resistivity modelling using conjugate gradient method. *Geophys. J. Inter.*, 123/3, pp. 903–914.

Geosciences and Engineering, Vol. 6, No. 9 (2018), pp. 32–39.

REDUCTION TO POLE OF NON-EQUIDISTANTLY MEASURED MAGNETIC DATA USING AN INVERSION-BASED FOURIER TRANSFORMATION ALGORITHM

DANIEL O. B. NUAMAH[1]–MIHÁLY DOBRÓKA[1]

[1]*Department of Geophysics, University of Miskolc, Miskolc-Egyetemváros, H-3515 Miskolc, Hungary*

Abstract: Method development in data processing is an important discipline in geophysics and other engineering fields. The ability to derive quality information from interpretation largely depends on the effectiveness of the data processing method applied. A new robust and resistant inversion based 2D Fourier transformation is presented where the spectrum is discretized by series expansion (S-IRLS-FT) using Hermite-functions as basis functions. The series expansion coefficients are given by the solution of a linear inverse problem. Taking advantage of the beneficial properties of Hermite-functions, that they are the eigenfunctions of the inverse Fourier transformation, the elements of the Jacobian matrix can be calculated rapidly and easily without integration. The procedure was robustified using the Iteratively Reweighted Least Squares (IRLS) method with Steiner weights. This resulted in a very efficient, robust and resistant inversion procedure. Its applicability is demonstrated in the reduction to the pole of synthetic magnetic data generated (or produced) in regular (equidistant sampling) and even in "random walk" measurement arrays. Compared to the standard DFT algorithm, the inversion-based 2D Fourier transformation proved to be more robust and effective in processing, even in the random walk dataset.

Keywords: *Fourier Transformation, Inversion, Series Expansion, Cauchy Noise, Random Walk*

INTRODUCTION

The systematic improvement in geophysical data acquisition over the years demands more innovative data processing methods. Traditional surveys employ equidistant measurement on a regular grid. Unfortunately, measurements are sometimes taken out of grid due to several obstacles encountered in the field. This has necessitated the development of processing techniques equally effective at "random walk" measurements. Fourier transformation is one of the most frequently used operations in data processing. It connects the time domain of signal registration and the frequency domain of signal processing. In case of discrete data sets, the Discrete Fourier Transformation (DFT) algorithm is often applied. As the measured data always contain noise, the noise sensitivity of the processing methods is an important feature. The noise registered in the time domain is directly transformed into the frequency domain. Therefore, the traditional discrete variants of Fourier transformation are

very noise sensitive procedures. Dobróka et al. [1] presented an inversion based 1D Fourier transformation method (S-IRLS-FT) which proved to be an effective tool for noise reduction. The method was then generalized to 2D, and an application was presented in solving reduction to the pole of the magnetic data set (Dobróka et al. [2]). In this paper, it is shown that the newly developed inversion-based Fourier transformation algorithm can also be used in the processing of a non-equidistant (even random walk) geometry dataset.

METHOD DEVELOPMENT – 2D INVERSION-BASED FOURIER TRANSFORMATION

The 2D Fourier transform of a function $u(x,y)$ can be calculated by the integral

$$U(\omega_x, \omega_y) = \frac{1}{2\pi} \int_{-\infty}^{\infty} \int_{-\infty}^{\infty} u(x, y)\, e^{-j(\omega_x x + \omega_y y)}\, dx\, dy\,, \tag{1}$$

its inverse is given by the formula

$$u(x, y) = \frac{1}{2\pi} \int_{-\infty}^{\infty} \int_{-\infty}^{\infty} U(\omega_x, \omega_y)\, e^{j(\omega_x x + \omega_y y)}\, d\omega_x\, d\omega_y\,, \tag{2}$$

where x, y are the spatial coordinates, $U(\omega_x,\omega_y)$ means the 2D spatial-frequency spectrum, and ω_x, ω_y indicate the spatial-angular frequencies. Following a powerful inversion strategy (the so-called series expansion-based optimization) developed at the Geophysical Department of the University of Miskolc (Gyulai and Szabó [3], Dobróka et al. [1]), the discretization of the continuous spectrum can be done through series expansion,

$$U(\omega_x, \omega_y) = \sum_{n=1}^{N} \sum_{m=1}^{M} B_{n,m}\, \Psi_{n,m}(\omega_x, \omega_y)\,, \tag{3}$$

where $\Psi_{n,m}(\omega_x,\omega_y)$ are frequency dependent basis functions, and $B_{n,m}$ are the expansion coefficients which represent the model parameters of the inverse problem. The basis function system should be square integrable in the interval $(-\infty, \infty)$. The Hermite functions meet this criterion with an additional advantage. The determination of Jacobian matrix in an inversion process requires the calculation of a complex integral for the interval $(-\infty, \infty)$, which is usually a time-consuming process. As was derived by Dobróka et al. [1], the elements of the Jacobian matrix can be considered as the inverse Fourier transformation of the basis function system. Therefore, they can be calculated more easily if the basis functions are chosen from the eigenfunctions of the inverse Fourier transformation. It can be shown that the normed and scaled Hermite functions

$$H_n(\omega_x,\alpha)=\frac{e^{-\frac{\alpha\omega_x^2}{2}}h_n(\omega_x,\alpha)}{\sqrt{\sqrt{\frac{\pi}{\alpha}}n!(2\alpha)^n}},$$

where

$$h_n(\omega_x,\alpha)=(-1)^n e^{\alpha\omega_x^2}\left(\frac{d}{d\omega_x}\right)^n e^{-\alpha\omega_x^2}, \tag{4}$$

$$H_m(\omega_y,\beta)=\frac{e^{-\frac{\beta\omega_y^2}{2}}h_m(\omega_y,\beta)}{\sqrt{\sqrt{\frac{\pi}{\beta}}m!(2\beta)^m}},$$

where

$$h_m(\omega_y,\beta)=(-1)^m e^{\beta\omega_y^2}\left(\frac{d}{d\omega_y}\right)^m e^{-\beta\omega_y^2}, \tag{5}$$

are eigenfunctions of the inverse Fourier transformation and the Jacobian matrix of the inverse problem can be written as

$$G_{k,l}^{n,m}=\frac{(j)^{n+m}}{\sqrt[4]{\alpha\beta}}H_n^{(0)}\left(\frac{x_k}{\sqrt{\alpha}}\right)H_m^{(0)}\left(\frac{y_l}{\sqrt{\beta}}\right). \tag{6}$$

Here $H_n^{(0)}, H_m^{(0)}$ denote the non-scaled Hermite functions. Applying *Equation (6)* provides a fast solution to the forward problem

$$u(x_k,y_l)=\sum_{n=1}^{N}\sum_{m=1}^{M}B_{n,m}G_{k,l}^{n,m}. \tag{7}$$

The introduction of single indices instead of double ones ($s = k + (l - 1)K$, $I = n + (m - 1)N$) makes the calculations much easier:

$$u(x_k,y_l)=u_{k,l}=u_s,\quad B_{nm}=B_i,\quad u_s=\sum_{i=1}^{I}B_i G_{s,i},\quad (i=1,...,I,\ \ s=1,...,S), \tag{8}$$

where $I = N + (M - 1)N = NM$ is the number of series expansion coefficients, $S = K + (L - 1)N = KL$ is the maximal number of data. With these simplifications, the deviation of measured and calculated data (e_s) can be calculated as

$$e_s = u_s^{(measured)} - \sum_{i=1}^{I} B_i \, G_{s,i} \, . \tag{9}$$

The Iteratively Reweighted Least Squares (IRLS) method is a reliable data processing procedure if the data set contains outliers. It can be combined with Cauchy weights, where the scale parameters σ^2 have to be known a priori. Using the Most Frequent Value method (Steiner [4]), Szegedi and Dobróka [5] proposed the use of Steiner weights because the scale parameters are derived from the statistical sample in an inner iteration cycle. To make the Fourier transformation more robust, a new Steiner-weighted IRLS method (S-IRLS) was introduced where the following weighted norm is minimized

$$E_w = \sum_{s=1}^{N} W_{ss} \, e_s^2 \, , \tag{10}$$

where W_{ss} is the s-th Steiner weight. The normal equation for the j-th IRLS step can be written as

$$\underline{\underline{\mathbf{G}}}^{\mathbf{T}} \underline{\underline{W}}^{(j-1)} \underline{\underline{\mathbf{G}}} \vec{B}^{j} = \underline{\underline{\mathbf{G}}}^{\mathbf{T}} \underline{\underline{W}}^{(j-1)} \vec{u}^{(measured)} . \tag{11}$$

After reaching the stop criteria, the series expansion coefficients determined in the final iteration step are considered the solution of the problem.

APPLICATION

To prove the applicability of the 2D robust inversion based S-IRLS FT method, we tested it on synthetic magnetic data sets. The initial data was noise free and was contaminated with random noise following Cauchy distribution for processing. A set of 1089 measurement points was assumed along with a 5 m × 5 m grid, which was further randomized to obtain non-equidistant measurements. Data were generated for a surface between –100 m, and 100 m both in the x and y directions above a 'C_L' shaped magnetic body (inclination I = 63°, declination D = 3°, magnetization 200 nT). The surface magnetic data were calculated by the Kunaratnam [6] method and were subsequently reduced to the pole (I = 90°) by applying the formula in the frequency domain

$$R(u,v) = T(u,v) S(u,v) , \tag{12}$$

where $T(u,v)$ is the 2D Fourier transform of the magnetic data set, $S(u,v)$ is the frequency domain operator of pole reduction, and $R(u,v)$ is the reduced data set after

the data reduction process. First, the reduction to the pole was performed using a conventional DFT algorithm. The map of noiseless magnetic data on equidistant grid and its reduced-to-pole-one version are given in Figure 1a and Figure1b, respectively. The data was contaminated with Cauchy noise to produce *Figure 2a*, which was reduced to pole using the traditional DFT method. The poor noise reduction capability of the DFT method can be clearly seen in *Figure 2b*. This underlines the need for a new, robust and outlier-resistant Fourier Transformation method.

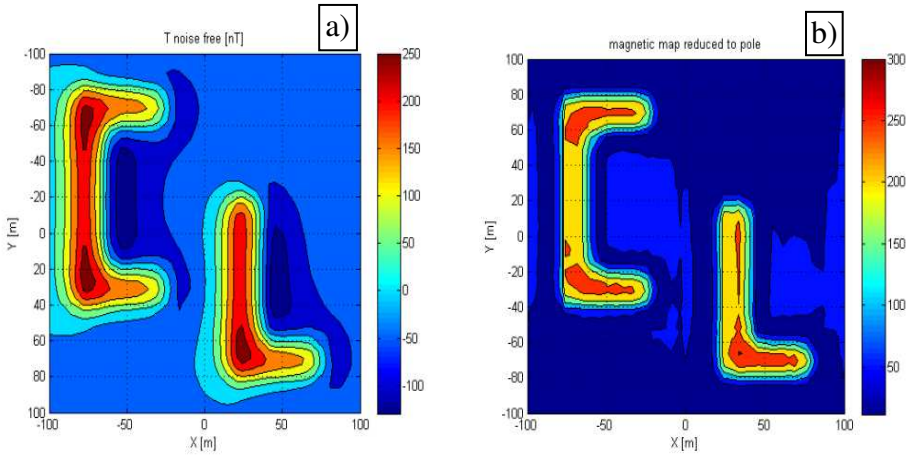

Figure 1. *Noise-free data set and the conventional DFT:*
a) Magnetic map without pole reduction, b) Magnetic map reduced to the pole

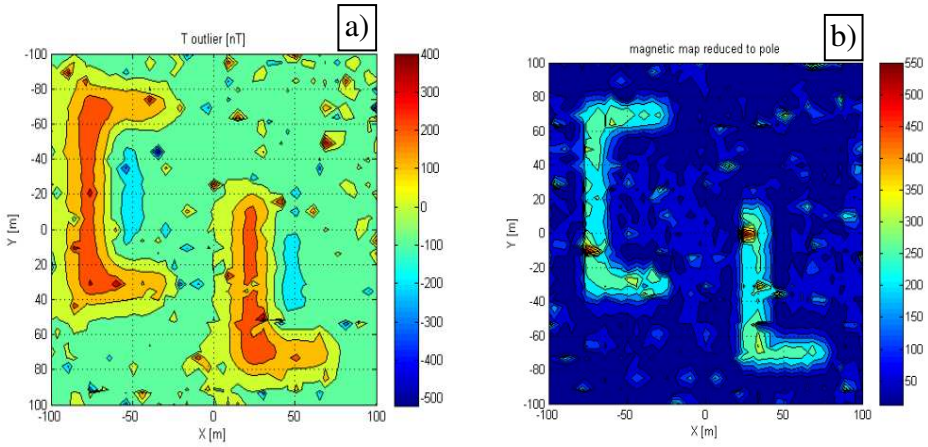

Figure 2. *Data set with Cauchy noise and the conventional DFT:*
a) Magnetic map without pole reduction, b) Magnetic map reduced to the pole

Therefore, the magnetic data were processed using the new S-IRLS-FT algorithm instead of traditional DFT. The same map of noisy data *(Figure 3a)* and its processing result are presented *(Figure 3b)*. Comparing *Figure 2b* (the pole reduced map on noisy data set using conventional DFT) and *Figure 3b* (the pole reduced map

on noisy data set using S-IRLS-FT), significant improvement can be seen in the processed data using the S-IRLS-FT method. The traditional DFT left more spikes of Cauchy noise after the pole reduction, causing artifacts and a possible misinterpretation of magnetic anomalies. The high noise reduction capability of the new S-IRLS-FT algorithm is clearly observable.

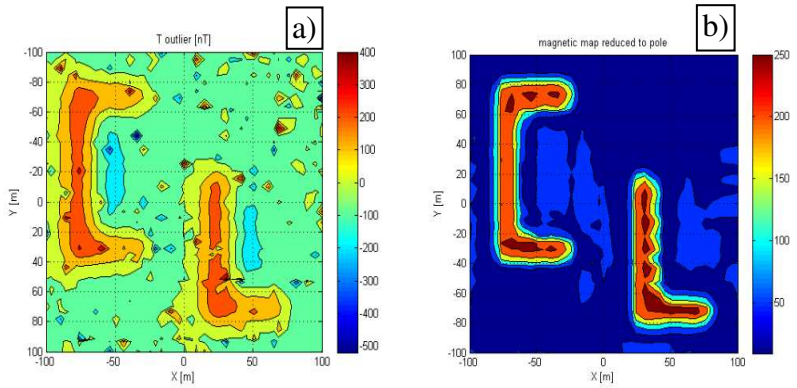

Figure 3. *Data set with Cauchy noise and the new S-IRLS-FT: a) Magnetic map without pole reduction, b) Magnetic map reduced to the pole*

As important feature of the new inversion-based Fourier Transformation is that the measurement array should not be equidistant along the (*x, y*) directions. This capability is demonstrated in *Figure 4*. In *Figure 4a*, (produced from *Figure 1a* and the same as *Figure 1b*) the arrangement of the measurement points was equidistant. To generate a highly non-equidistant arrangement, we shifted randomly all the measurement points from their "regular" place in the sampling interval before the S-IRLS FT method was applied. The result in the noise-free case is shown in *Figure 4b*, which is similar to *Figure 4a*, demonstrating that the method gives accurate results even in "random walk" measurements. *Figures 5* and *6* show a plot of sampling points or generated survey coordinates on the regular equidistant grid as well as random walk geometry measurement.

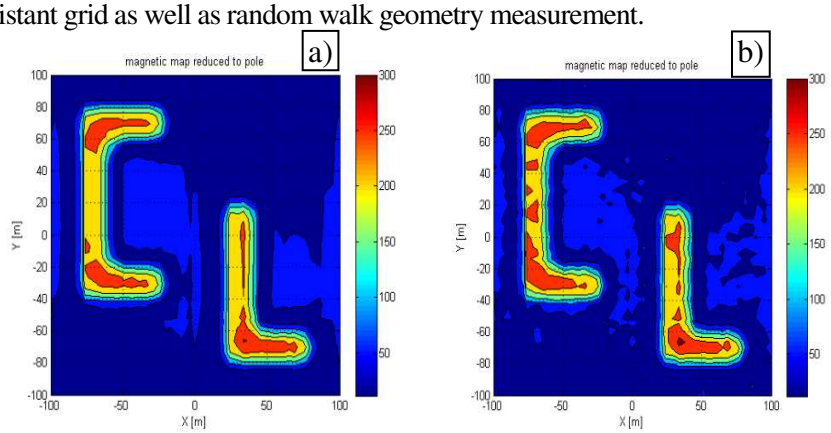

Figure 4. *Reduction to the pole of noise-free data set: a) Equidistant measurement system, b) Random walk measurement system*

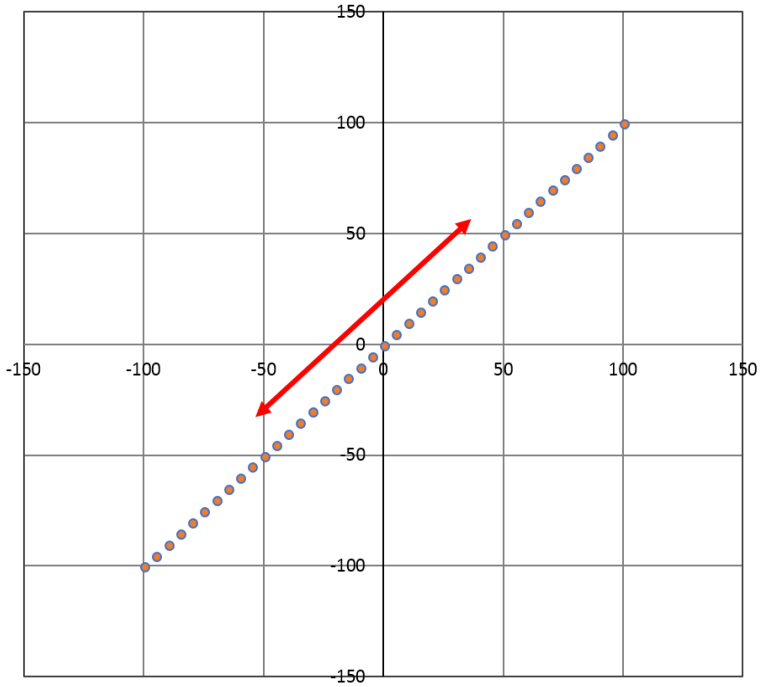

Figure 5. *A linear plot of equidistant sampling location on a regular grid*

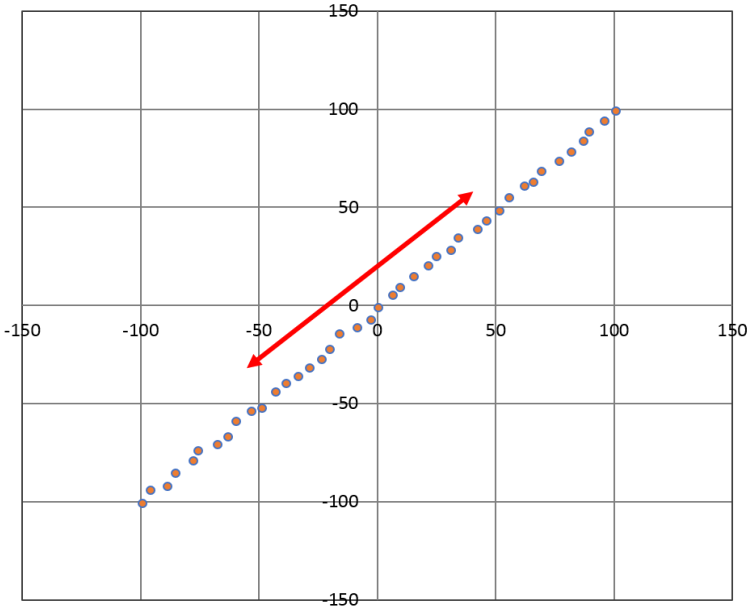

Figure 6. *A linear plot of "random walk" sampling location*

CONCLUSION

The Discrete Fourier Transformation (DFT) is a common data processing method but incorporates some level of noise in the transformation process, as shown here. Therefore, a new algorithm had to be developed. The introduced 2D S-IRLS-FT method treats the Fourier transformation as an inverse problem. Data are discretized by series expansion and the inversion problem is solved for the series expansion coefficients by IRLS method using Steiner weights. Taking advantage of the good features of Hermite functions described in this paper, they were chosen as basis functions making the algorithm faster. Comparatively, the newly introduced inversion-based Fourier transformation algorithm (2D S-IRLS-FT method) has a higher noise rejection capability than the traditional DFT Method, as demonstrated in reduction to pole of magnetic data. It was also shown that the inversion-based Fourier transformation algorithm can be effectively used in processing of data sets collected in non-equidistant (even in random walk) geometry.

ACKNOWLEDGEMENTS

The described article was carried out as part of the EFOP-3.6.1-16-2016-00011 *Younger and Renewing University – Innovative Knowledge City – institutional development of the University of Miskolc aiming at intelligent specialization* project implemented in the framework of the Szechenyi 2020 program. The realization of this project is supported by the European Union, co-financed by the European Social Fund. The authors express their thanks to prof. dr. Tamás Ormos for his help and activity in program development.

REFERENCES

[1] Dobróka, M., Szegedi, H., Somogyi Molnár, J. Szűcs, P. (2015). On the Reduced Noise Sensitivity of a New Fourier Transformation Algorithm. *Math. Geos*., 47 (6), pp. 679–697.

[2] Dobróka M, Szegedi H. & Vass P. (2017). Inversion-based Fourier transform as a new tool for noise rejection. *INTECH 2017*, Doi:10.5772/66338.

[3] Gyulai, Á., Szabó, N. P. (2014). Series expansion based geoelectric inversion methodology used for geo-environmental investigations. *Frontiers in Geosc.*, 2 (1), pp. 11–17.

[4] Steiner, F. (1997) *Optimum methods in statistics*. Budapest: Akadémiai Kiadó.

[5] Szegedi, H., Dobróka, M. (2014). On the use of Steiner's weights in inversion-based Fourier transformation – robustification of a previously published algorithm. *Acta Geodaetica et Geophysica*, 49/1, pp. 95–104, DOI 10.1007/s403 28-014-0041-0.

[6] Kunaratnam, K. (1981) Simplified expressions for the magnetic anomalies due to vertical rectangular prisms. *Geophys. Prosp.,* 29, pp. 883–890.

Geosciences and Engineering, Vol. 6, No. 9 (2018), pp. 40–52.

CGI INVERSION METHOD PRESENTED THROUGH A FIELD CASE

MÁTYÁS KRISZTIÁN BARACZA[2, 3]–ENDRE TURAI[2]–
ENDRE NÁDASI[1, 2]–ÁKOS GYULAI[2]

[1] *MTA-ME Geoengineering Research Group*
[2] *University of Miskolc, Department of Geophysics*
[3] *University of Miskolc, Research Institute of Applied Earth Sciences*

Abstract: This paper presents the application of Combined Geoelectric Inversion (CGI) to real data. The geoelectric survey was performed in the Mátra Mountains. The geological setting of the area is very complex; clay zones can be found in highly fractured andesite as a result of weathering of strongly tectonized volcanic rock. The CGI inversion method was compared to the widely used RES2DINV algorithm using the field data. The results clearly showed the strengths of the CGI inversion program, as it has better resolution and higher reliability than the RES2DINV program. This study also deals with the possibility of generalization of the CGI inversion method.

Keywords: *geoelectric, combined inversion, series expanson-based inversion, 1.5D inversion*

INTRODUCTION

The results and efficiency of the CGI (Combined Geoelectric Inversion) method have been demonstrated in some earlier publications. Some of the presented examples includes inversions on synthetic models, while others comprise field cases. The CGI method consists of two main steps (Gyulai et al. 2010). At first, 1D approximation is applied in forward modeling to calculate data at VES stations along a profile. In the second step, the inversion is solved on the whole 2D profile. We call this inversion strategy 1.5D inversion. Our investigations made on synthetic and field data confirmed that the 1.5D inversion method gives much more accurate parameters than a series of individual 1D inversions (Gyulai and Ormos 1997a, 1997b, 1999). One reason for this is that the series expansion-based inversion contains much fewer unknowns than data, while it is also due to the nature of simultaneous (joint) inversion characteristics of the inverse problem. In 1.5D approximate inversion, series expansion was applied for describing the lateral change of the model parameters. Two types of series expansions were applied in our program. One of them was based on series expansion using power functions, the other used Fourier series expansion. This problem can be handled by a more generalized method as well, series expansion based on arbitrarily chosen basis functions, which was introduced by Dobróka (1994), Kis (1998), and Szabó (2004). We assume that laterally changing model parameters can be approximated with sufficient accuracy by using the orthogonal Fourier series expansion:

$$\rho_n(s) = \frac{1}{2} d_{n_0} + \sum_{k=1}^{K_n} d_{n_k} \cos k \frac{2\pi s}{S_p} + \sum_{k=1}^{K_n} d^*_{n_k} \sin k \frac{2\pi s}{S_p}, \quad (1)$$

where $n = 1, \ldots, N-1$,

$$h_n(s) = \frac{1}{2} c_{n_0} + \sum_{l=1}^{L_n} c_{n_l} \cos l \frac{2\pi s}{S_p} + \sum_{l=1}^{L_n} c^*_{n_l} \sin l \frac{2\pi s}{S_p}, \quad (2)$$

where $n = 1, \ldots, N-1$, and $\rho_n(s)$ is the resistivity function, $h_n(s)$ is the function describing the *n*-th layer-thickness. Parameters d_{n_k}, $d^*_{n_k}$, c_{n_l} and $c^*_{n_l}$ denote the series based expansion coefficients, which should be determined by the inversion procedure; the model parameters can be derived from them. Constant N is the number of layers, and *s* is the lateral coordinate along the profile of total length S_p. The maximal values of $K_n$and L_n are the number of VES stations.

Because of the 1D approximation, the result of the 1.5D inversion can be accepted as a final result only in the case of slowly changing geological structures. This is valid for the case when the estimation error indicates relatively good results. It should not be forgotten that the model error due to the approximation is not or is only a small part of the covariance matrix. Thus, both the estimation error and the correlation matrix can be considered also as an approximation.

THE COMBINED GEOELECTRIC INVERSION (CGI) METHOD

For getting more accurate results in the case of abruptly varying geological structures, it might be necessary to apply a subsequent step in the inversion procedure, namely the application of a 2D or 3D method in forward modeling (Spitzer 1995), depending on the complexity of the geological structure. The first short description of the method was presented by Gyulai (1999). Just as 1D forward modeling can can be used as an approximation in the case of 2D structures, so can 2D forward modeling be used in a 3D case. Just as 1D forward modeling can can be used as an approximation in the case of 2D structures, so can 2D forward modeling be used in a 3D case. Gyulai and Tolnai (2012) demonstrated that the simultaneous inversion of bidirectional VES data using 2D forward modeling can be applied in practice (with the application of Steiner's weights) for the detection of 3D geological structures. The essence of the method is that the bidirectional (strike and dip directional) measurements are evaluated together and simultaneously, with an adjustment method based on the most frequent value (Steiner 1988). The technique was named Steiner's weighing method after its author. Outlying data given as a result of the approximation are automatically taken into consideration with smaller weight by the inversion. A special application of the technique will be presented at the end of the next chapter section.

FIELD CASE

The field measurement was conducted in the Mátra Mountains, North Hungary. An IRIS Syscal Pro instrument was applied. The apparent resistivity distribution can be

seen in *Figure 1* for Schlumberger array. Based on our practical experience, for structures comprised of mostly 2D elements, the pseudosection referenced to AB/4 (m) depths is the most similar to the parameter distribution obtained by inversion, that is, to the geological structure including the depth distributions as well.

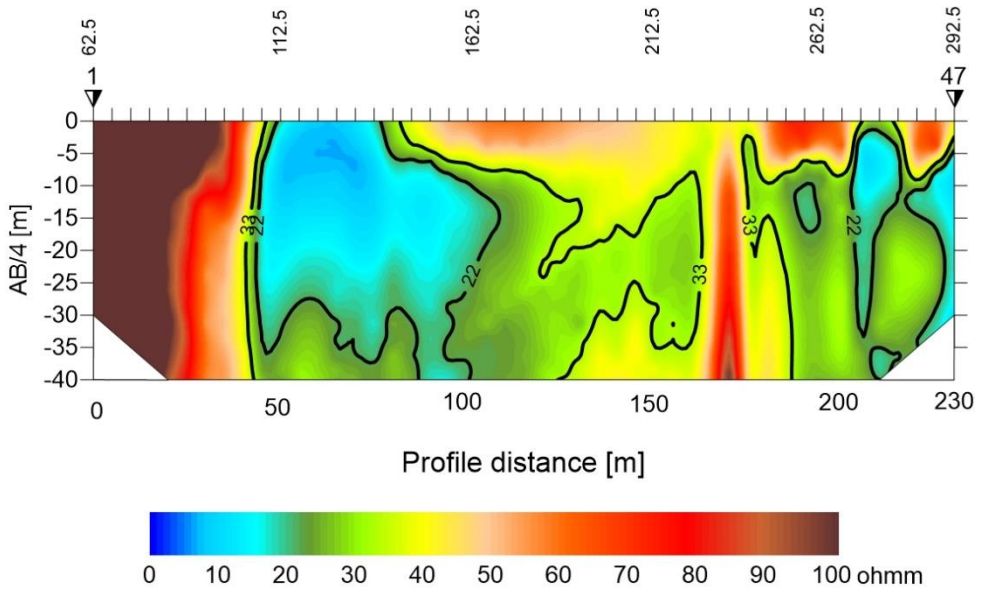

Figure 1. *Measured apparent resistivity pseudosection from 2D imaging survey* (Schlumberger)

Figure 1 shows a truncated segment of the apparent resistivity section, where the maximal value of AB/4 is 40 m, which is equal to the maximal investigation depth. Even the distribution of the various colors of the apparent resistivity pseudo profile shows the inhomogeneity of the examined area. The cool colors represent the presence of clay minerals, while the warm colors indicate volcanic origin clastic rocks, which have worse electrical conductivity. Two types of profile distance are shown on the section: the relative scale beginning with 0 m can be seen below, the absolute scale indicating the real profile distance is given above. The same scaling system was applied to the additional sections as well, for the sake of easier comparability.

Figure 2 shows the inversion result calculated with the RES2DINV program. The RES2DINV program (Geotomo Software) is used worldwide. The original section is longer than this, with gradually decreasing penetration depth towards the edges of the profile (trapezoid section). To compare it with the CGI results, a truncated/shortened version of the section is presented. The color scale of the section is logarithmic, which is offered at relatively large intervals by RES2DINV. The RMS value (data distance) calculated by the RES2DINV software was 6.5% for *Figure 2*.

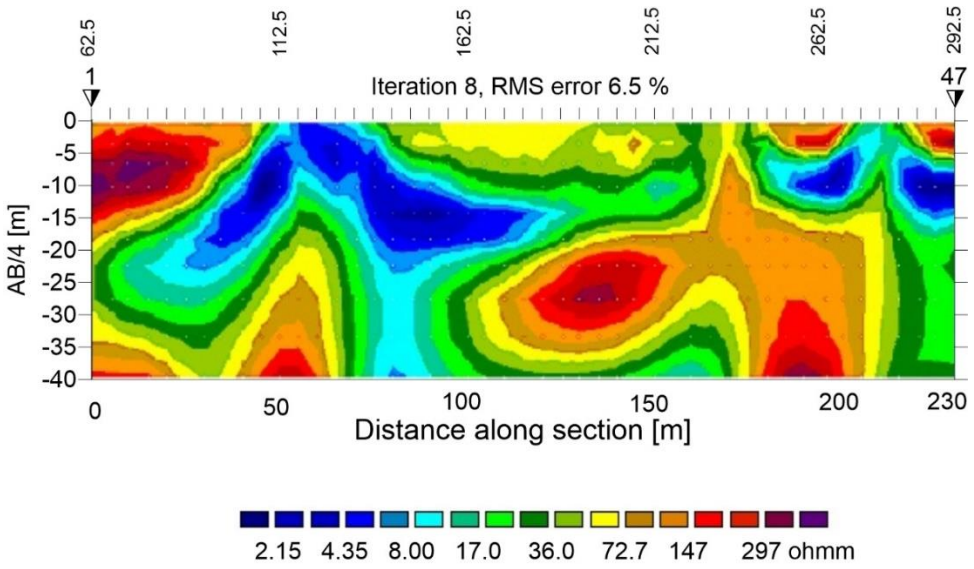

Figure 2. *Resistivity distribution along the section created by RES2DINV software*

On the resistivity image of CGI inversion, a more detailed color scale was applied, which shows similar colors at characteristic rock changes.

The largest possible investigation depth was utilized during the evaluation, which was 40 m. It is well known that the resistivity distribution of the structure is described by the resistivity values of a set of elementary blocks. Because of the huge number of unknown parameters, the problem is underdetermined. This is dissolved by smoothing methods, which grant the stability of the inversion, but are not backed up by geological data. It follows that the interfaces cannot appear sharply and the resolution of the inversion method is not sufficient. It is not possible to use squality checking parameters based on the application of constraints, which is based on the covariance matrix. The authors of this new inversion method are rather critical of the widespread used of RES2DINV software, which is more of a tomographic (inversion) method, in near-surface investigations, especially in the case of 3D structures. RES2DINV allows users to compare the measured and calculated data, but in practice this comparison is usually made by smoothing out the little differences between them. Furthermore, in the case of complex geological structures, these distances in the data space inadequately characterize the reliability of the estimation.

In *Figure 2* the inverted profile also shows the significant inhomogeneity of the area. The blueish colors denote clayey rocks, while the shades of red indicate the volcanic debris set of rocks containing fewer clay minerals.

Figures 3–6 show the results of CGI inversion results using the data set given in *Figure 1*. In this paper, the authors do not deal with the strategy of the series expansion inversion, because it is presented in detail in Gyulai et al. (2010). It should be

noted that in case of complex geological structures, it is usually enough to choose the coefficients of either the layer thicknesses or resistivities for the rapid description of the lateral changes. The necessary trial runs can be executed quickly during the 1.5D inversion and the necessary practical routine can be acquired soon.

Two examples of CGI evaluation are presented in this paper. In "Inversion 1" the same series of expansion based inversion coefficients were applied in the second step (2D forward modeling) of the CGI as in the first step of the inversion (1D forward modeling). Generally, this solution is applied in practice. In addition, however, the selection of the coefficients is a critical part of the strategy; there is no significant difference in the result of the inversion if there are some differences from the optimal number of coefficients. Hence, in "Inversion 2" the method was branched, so the number of the coefficients was increased from the 16th iterative step (*Figure 5*, Inversion 2). It could have been done from an earlier or a later iterative step as well.

Some quantities should be defined for use in validating the accuracy of the inversion results. The normalized data distance (d) is defined as

$$d = \sqrt{\frac{1}{I}\sum_{i=1}^{I}\left(\frac{\rho_{a,i}^{(measured)} - \rho_{a,i}^{(calculated)}}{\rho_{a,i}^{(calculated)}}\right)^2} * 100\%, \tag{3}$$

where I indicates the total number of measured apparent resistivity data $(\rho_{a,i})$. In field data calculated from the parameters $(\vec{m}^{(start)})$ of start model, the relative model distance can be computed as

$$D^* = \sqrt{\frac{1}{M}\sum_{i=1}^{M}\left(\frac{m_i^{(estimated)} - m_i^{(start)}}{m_i^{(start)}}\right)^2} * 100\%, \tag{4}$$

where M denotes the total number of model parameters.

In inversion, the means of the variances qualifies the precision of the parameter estimation. These can be derived from the diagonal elements of the parameter covariance matrix (Menke 1984). The elements of the covariance matrix at each VES station can be computed as follows (using series expansion):

$$\sigma_{km} = \sigma_k(x_m) = \frac{\sqrt{\sum_{i=1}^{J(k)}\sum_{j=1}^{J(k)}\left\{\Psi_{ki}(x_m) * \Psi_{kj}(x_m) * COV_{ij}\right\}}}{p_k(x_m)}, \tag{5}$$

where $\sigma_k(x)$ indicates the estimation error of the k^{th} model parameter (i.e., resistivity or thickness) and σ_{km} is the same at the m^{th} VES station (at $x = x_m$). K is the total number of the $p_k(x)$ model parameters ($k = 1,2,...,K$) and M is the number of VES stations along the profile ($m = 1,2,...,M$). $J(k)$ is the number of elements in the basis function of the series expansion describing the k^{th} model parameter, $\Psi_{ki}(x)$ and $\Psi_{kj}(x)$ are the i^{th} and j^{th} basis functions, and COV_{ij} denotes the covariance matrix elements of the estimated expansion coefficients (defined in Menke 1984).
The mean (percentage) estimation error (F) is defined as

$$F = \sqrt{\frac{1}{KM}\sum_{k=1}^{K}\sum_{m=1}^{M}\sigma_{km}^2} * 100(\%) \,. \tag{6}$$

It presents the accuracy of the parameter estimation for the whole model. The degree of correlation among the estimated model can be characterized by the extensively used correlation matrix

$$CORR_{ij} = \frac{COV_{ij}}{\sqrt{COV_{ii}COV_{jj}}}. \tag{7}$$

A single scalar, which is called mean spread or correlation norm (Menke, 1984), is also introduced as follows

$$S = \sqrt{\frac{1}{P(P-1)}\sum_{j=1}^{P}\sum_{i=1}^{P}\left(CORR_{ij} - \delta_{ij}\right)^2} \,. \tag{8}$$

In contrast to the correlation matrix, S describes the model correlation with one single value, where P is the total number of the model parameters and δ_{ij} is the Kronecker delta symbol.

The smaller the values of the above introduced D, F and S are, the more reliable the results of the inversion are. In the case of field data, only F and S values can be used for characterization of the inversion results.

Figures 3a–c show the results of the 1.5D inversion. *Figure 3a* presents the determined resistivity structure by the inversion procedure, whereas *Figure 3b* shows the distribution of data distances (difference between measured and calculated data normalized with calculated data). The 1.5D inversion result is quite similar to that of CGI, the data distance d is 6%, which is slightly lower, than in case of RES2DINV. It is interesting to observe the high values of *Figure 3c*, where the distribution of data distances (calculated on the 2D model) are presented at the 0^{th} iteration of CGI.

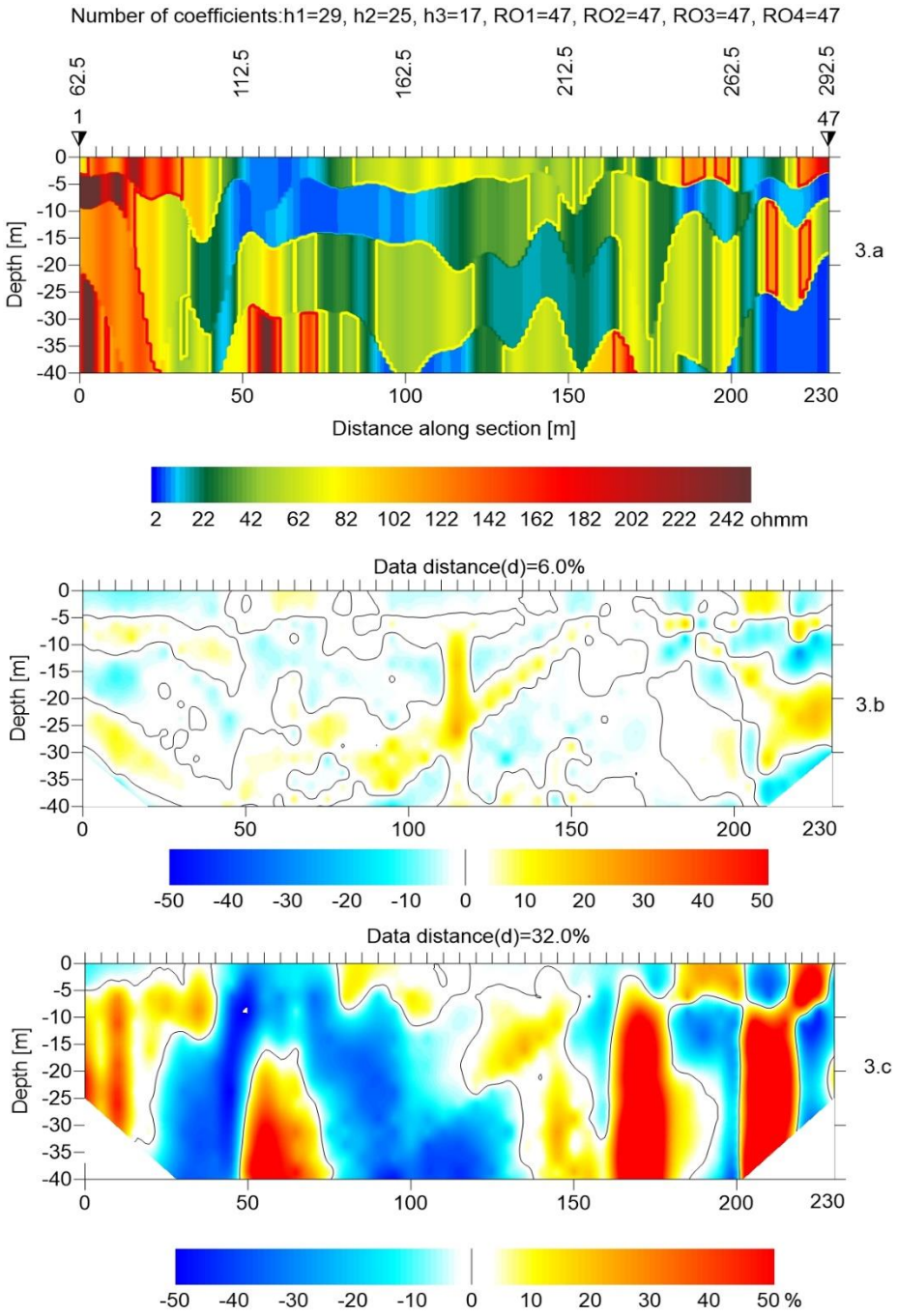

Figure 3. *a) Resistivity section estimated by VES 1.5D inversion*
b) Data distance distribution of VES 1.5D resistivity section
c) Data distance distribution at the 0th iteration of CGI resistivity section

The large data distances connected with the 0th iteration of 2D forward modeling confirm that 1.5D inversion is not able to map the 2D structure properly, because of the abrupt geological changes, in spite of the low value of mean data distance (6%). *Figures 4a* and *4b* show the result of the combined inversion procedure. The number of the coefficients is h1 = 29, h2 = 25, h3 = 17, ρ1 = 47, ρ2 = 47, ρ3 = 47, ρ4 = 47. The thicknesses vary "slowly", while the resistivities change "as fast as possible" in the CGI inversion. The maximal number of the coefficients is equal to the number of the VES stations (47).

Parameter F denotes the mean of the estimation errors, which was defined earlier in Gyulai et al. (2010).

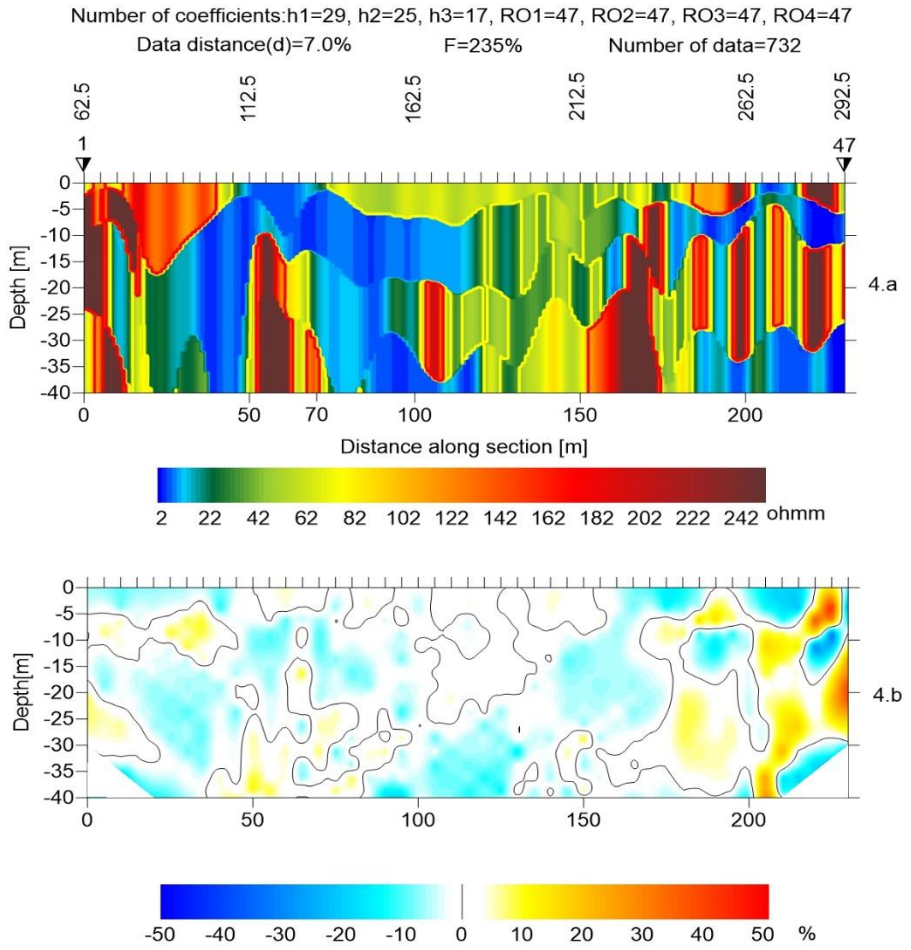

Figure 4. *a) CGI inversion result of Inversion 1*
b) Distribution of data distance along resistivity section (CGI inversion), in case of Inversion 1

The resultant section of the inversion shows big changes between 2–250 ohmm, which indicates quite good resolution. It is important to highlight a vertical structural change of about 30 m high appearing on the section between 50 and 70 m, which is indicated by a resistivity change from 2 ohmm (clay) to 200 ohmm (compact andesite).

Although earlier it was not expected that such big changes could be detected by a geoelectric method, similar changes appear in different parts of the section. The resultant section of the inversion can be correlated well with the apparent resistivity section on *Figure 1*. It is not surprising that the apparent resistivity section is considered as a final result in many cases, because it often gives better results than a "misfit"-based inversion method.

In *Figure 5*, the inversion runs can be seen as a function of iteration number, which were edited based on the inversions of *Figures 3, 4* and *6.* The figure can be divided into three parts: iteration steps 1–10: 1.5D inversion; 11–16 iterations: transition phase between 1D model and 2D model (however, forward modeling is 2D from the 11th iteration); 16–21 iterations: inversions giving a 2D solution.

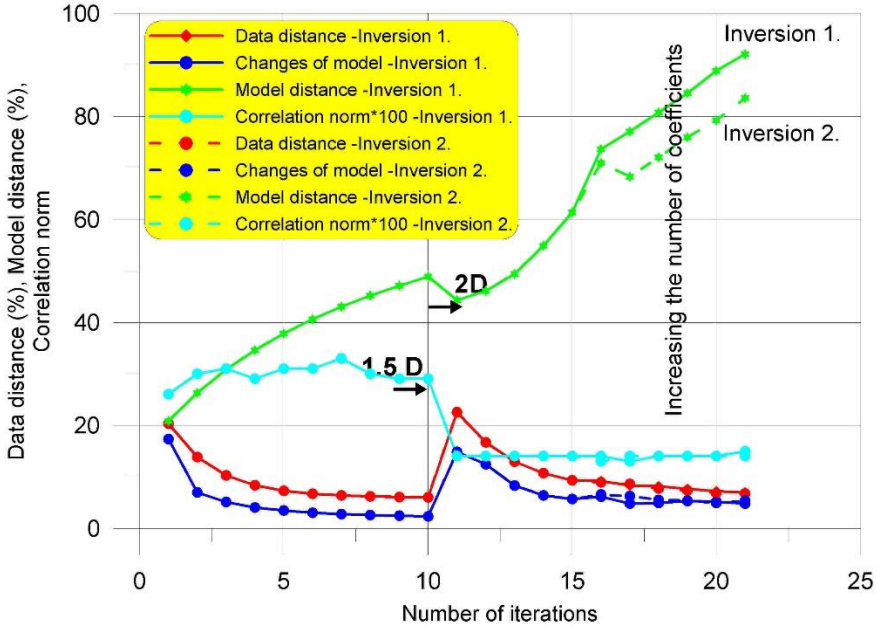

Figure 5. *Data distance (d), Model distance (D*) and Correlation norm (S) change during the CGI inversion process*

One more important phenomenon should be mentioned. In the case of a similar four-layer model, the values of correlation norm as a measure of the reliability of the inversion result are usually ~0.7 (1D), ~0.3 (1.5D) and ~0.15 (2D). The low values of the correlation norm show the real strength of CGI, which gives more precise

estimation and resolution than the earlier ones (1.5D) for similar data sets. This results in a remarkable decrease of equivalence in case of noisy data. The equivalence can be reduced effectively by involving other types of geophysical data and (with) the simultaneous inversion of them.

As was indicated at the beginning of this chapter, the inversion branched after the 16th iterative step, thus the number of the layer thickness coefficients was increased to achieve higher resolution. The number of the coefficients of layer thickness was changed to h1 = 33, h2 = 29, h3 = 29, while the coefficient numbers of the resistivities were kept at a possible maximal value (47). The results can be seen in *Figures 6a* and *6b*.

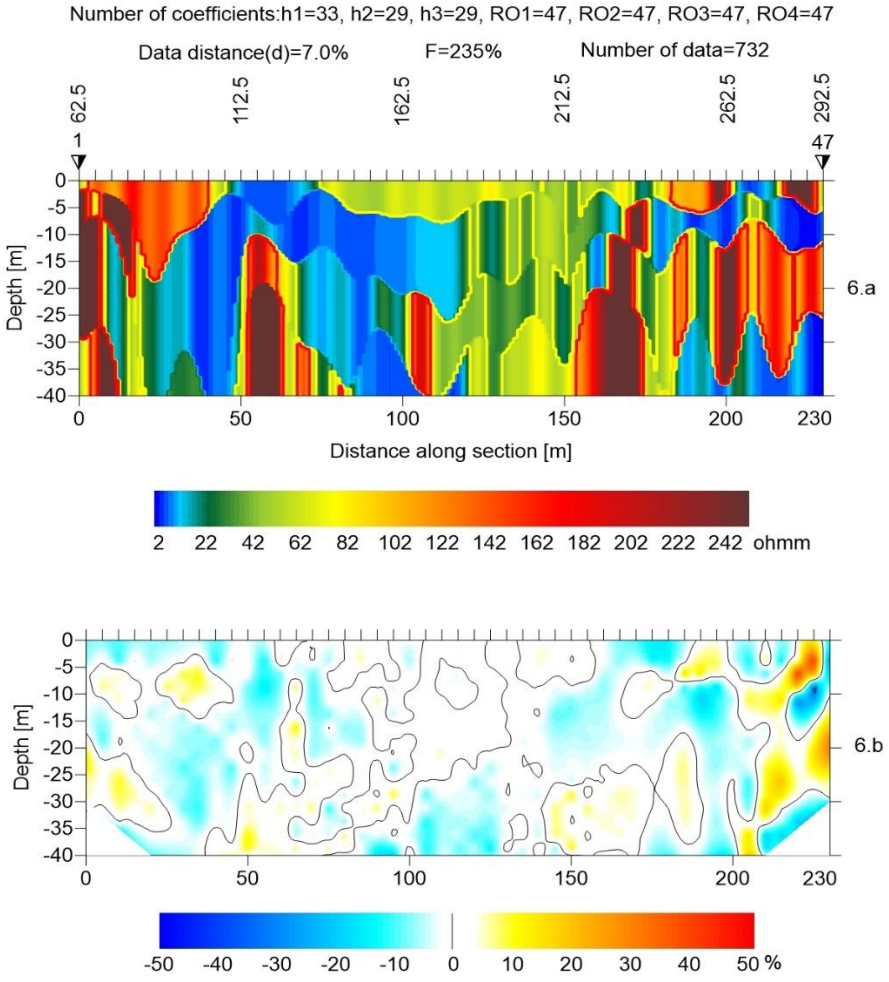

Figure 6. *a) CGI inversion result of Inversion 2*
b) The distribution of model data distance along the resistivity section (CGI inversion), in case of Inversion 2

It can be concluded that this change resulted in only an insignificant modification in geological structure, and in the model data distance distribution of the inverted profile as well. Therefore, the inversion is insensitive to the change in the expansion coefficients. The average estimation error F = 235% is a high value in geoelectric practice, which comes from the big resistivity contrast (2–250 ohmm). The deficiency of depth sampling causes further small errors, which comes from the equidistant electrode layout. The electrode spacing was five meters.

As was indicated earlier, with the application of the so-called Steiner's weighting, the simultaneous inversion of the dip- and strike directional measurement data can be performed. In the case of complex structures, if it is assumed that one part of measurements is strike directional and the other part is dip directional, the same section can be either dip directional or strike directional as input of simultaneous inversion. In case of 2D structures, the dip- and strike directional measurement data contain different information and have different parameter sensitivity to the geological structure (Gyulai 1995; Gyulai et al. 2017). The simultaneous application of them yields additional information for the determination of the parameters in the inversion. When using the CGI inversion method, – at the dip directional part of the section – the strike directional data (as being outlier data) are taken into consideration with smaller weight by the inversion. It should be performed the same way in the reverse case, – at the strike directional part of the section – the dip directional data (in this case, these are the outliers) are taken into consideration with smaller weight by the inversion. The Steiner's weighting method completed with an iterative weighting process is suitable for this aim, because the outlying data are taken into consideration only with a small weight (or absolutely none).

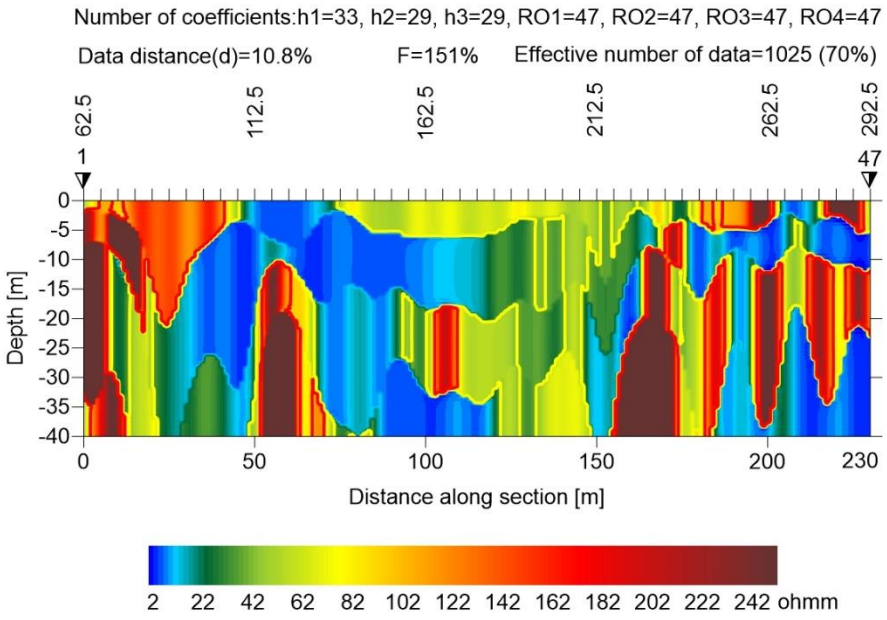

Figure 7. *Resistivity section produced by CGI inversion with Steiner's weighting method*

Figure 7 shows the result of such an evaluation method. The result of the inversion estimation scarcely differs from the results demonstrated in *Figures 4a* and *6a*. There is no noticeable difference between the presented 1.5D and CGI inversions in parameter estimation. However, an essential difference can be observed in the mean estimation errors. The mean estimation error presented on *Figure 7* is significantly lower than in case of the other two inversions. In the inverted profile shown in *Figure 7*, the shades of red represent more compact rock bodies of lower electrical conductivity. The yellowish and greenish shades indicate a transition to formations containing increasing amounts of clay. The darkest shades of blue denote zones filled with rich clay at certain parts of the inverted profile.

SUMMARY

CGI inversion of Schlumberger sounding data was presented, which was registered above a complex geological structure. The analysis of measurement data and inversion results shows that series expansion-based inversion is suitable for describing complex geological structures. The results of the two inversions (CGI and RES2DINV) show a similar character in the left side of the section, but there are significant differences between the results of the two inversion types in the right side of the section. In terms of the designation of layer boundaries, the determination of layer resistivities and the resolution of structural elements, the results of CGI are much more informative than the results of the RES2DINV program, used worldwide. Furthermore, it is important to mention that with this CGI inversion method we can improve the reliability of the determination of geological-geophysical structures using field data.

ACKNOWLEDGEMENT

The research was carried out in the framework of the GINOP-2.3.2-15-2016- 00010 *Development of enhanced engineering methods with the aim at utilization of subterranean energy resources* project of the Research Institute of Applied Earth Sciences of the University of Miskolc in the framework of the Széchenyi 2020 Plan, funded by the European Union, co-financed by the European Structural and Investment Funds.

REFERENCES

[1] Dobróka, M. (1994). *On the absorption-dispersion of Love waves propagating in inhomogeneous seismic waveguide of varying thickness; the inversion of absorption-dispersion properties*. (in Hungarian) Doctor of Science Thesis (Hungarian Academy of Science), Miskolc: Hungary.

[2] Geotomo Software. Res 2DINV 3.55. Malaysia, www.geoelectrical.com

[3] Gyulai, Á. (1995). Geoelectrical investigation of dipping beds with analytical forward modelling. *Magyar Geofizika*, Volume 36, Issue 1, pp. 40–67.

[4] Gyulai, Á. (1999). New geoelectrical inversion process for the determination of geological structures: Combined 2-D and 3-D function inversion. *Magyar Geofizika*, Volume 40, Issue 4, pp. 94–98.

[5] Gyulai, Á., Ormos, T. (1997a). Interpretation of vertical electrical sounding curves with 1.5-D inversion method. *Magyar Geofizika*, Volume 38, Issue 1, pp. 25–29.

[6] Gyulai, Á., Ormos, T. (1997b). New results in the 1.5-D inversion of VES data. *Magyar Geofizika*, Volume 38, Issue 4, pp. 257–264.

[7] Gyulai, Á.; Ormos T. (1999). A new procedure for the interpretation of VES data: 1.5-D simultaneous inversion method. *Journal of Applied Geophysics*, 41 (1), pp. 1–17.

[8] Gyulai, Á., Ormos, T., Dobróka M. (2010). A quick 2-D geoelectric inversion method using series expansion. *Journal of Applied Geophysics*, 72 (4), pp. 232–241.

[9] Gyulai, Á, Tolnai, É. (2012). 2.5D geoelectric inversion method using series expansion. *Acta Geodetica et Geophysica Hungarica*, 47 (2), pp. 210–222.

[10] Gyulai, Á., Szűcs, P., Turai, E., Baracza, M. K., Fejes, Z. (2017). Geoelectric Characterization of Thermal Water Aquifers Using 2.5D Inversion of VES Measurements. *Surveys in Geophysics*, Volume 38, Issue 2, pp. 503–526, doi:10.1007/s10712-016-9393-z

[11] Kis, M. (1998). *Investigation of near-surface structures by means of joint inversion of seismic and geoelectric data*. Ph.D. Thesis, University of Miskolc.

[12] Menke W. (1984). *Geophysical data analysis – Discrete inverse theory*. Academic Press Inc. London Ltd.

[13] Spizter, K. (1995). A 3-D finite difference algorithm for DC resistivity modeling using conjugate gradient methods. *Geophysical Journal International*, 123, pp. 902–914.

[14] Steiner, F. (1998). Most frequent value procedure (A short monograph). *Geophysical Transactions*, 34, 1998, pp. 139–260.

[15] Szabó, N. P. (2004). Global inversion of well log data. *Geophysical Transactions*, Eötvös Loránd Geophysical Institute of Hungary, Vol. 44, pp. 313−329.

Geosciences and Engineering, Vol. 6, No. 9 (2018), pp. 53–59.

IMPROVEMENT OF A SEISMIC Q MODEL

ANETT KISS[1, 2]–MIHÁLY DOBRÓKA[1, 2]

[1]*Department of Geophysics, University of Miskolc*
[2]*MTA-ME Geoengineering Research Group*
gfka@uni-miskolc.hu

Abstract: In this study, rock physical models are introduced to describe the pressure dependence of the seismic quality factor. The first model connects this phenomenon to the presence of one single inner process during loading of the rock samples that is manifested in the change of one extensive quantity, the pore volume. Therefore, it is called "Q-σ" Single Relaxation Model (SRM). Testing of the model proved that it works well in practice, i.e. the results are precise enough for engineering tasks, but in some cases it can be seen that a further development of the model could bring about a much better description of the pressure dependence of acoustic characteristics. Therefore, a new model handling the effects of two relaxation processes – the "Q-σ" Double Relaxation Model – is introduced as well. The model's applicability is tested on measured (laboratory) quality factor data published in the literature. The quality checked inversion results show that the misfits between measured and calculated data become much smaller, proving that the proposed new Double Relaxation Model can be applied well in practice and provide a better understanding of pressure dependence.

Keywords: *quality factor, relaxation model, single relaxation, double relaxation, pressure dependence*

INTRODUCTION

The investigations of acoustic parameters such as acoustic wave velocity and quality factor started more than a decade ago at the Department of Geophysics, University of Miskolc. The aim of the research was to find new rock physical models that can describe the pressure dependence of these parameters quantitatively and obtain an explanation for the physical relation between the parameters. The basic concepts link the pressure dependence of velocities and quality factors to the change in pore volume or closure of microcracks due to the increasing load, as Birch [1] or Walsh and Brace [2] proposed in their studies. This paper focuses on investigation of the pressure dependent quality factor. When increasing pressure acts on rock, grains become closer to each other (compaction occurs in the grain structure), resulting in decreasing pore volume, which causes an increase in quality factors. This is not a sudden event, but a slow process. Therefore the model presented here is considered a relaxation model and it is valid in the framework of the constant Q model. As a first approximation, only this effect was included [3]. Since the model considered one

process – change in pore volume – as the only phenomenon influencing pressure dependent quality factor, it was called the "Q-σ" Single Relaxation Model (SRM).

"Q-σ" SINGLE RELAXATION MODEL

As outlined above, the stress increase ($d\sigma$) causes a decrease in the value of an extensive quantity X according to the differential equation

$$dX = -\lambda d\sigma , \tag{1}$$

where λ is the proportionality factor. In the Single Relaxation Model the pore volume (dV) is substituted as the extensive quantity

$$dV = -\lambda d\sigma . \tag{2}$$

Let us assume a linear relationship between the change of pore volume (dV) and the change of quality factors (dQ) and introduce *Equation (3)* as model law

$$dQ = -\kappa dV , \tag{3}$$

where κ is a rock physical parameter and the negative signs represent that the decreasing pore volume results in increasing quality factor. Combining the solution of *Equation (2)* with *Equation (3)* the following relations can be written

$$dQ = \kappa\lambda V_0 e^{-\lambda\sigma} d\sigma . \tag{4}$$

The quality factor at a stress-free state (Q_0) can be measured, and so the integration constant can be calculated. Introducing the notation $\Delta Q_0 = \kappa V_0$, *Equation (4)* receives the form

$$Q = Q_0 + \Delta Q_0 (1 - e^{-\lambda\sigma}) , \tag{5}$$

where λ is the material dependent relaxation parameter. It can be seen from the three-parameter model equation that the quality factor changes exponentially with the pressure. ΔQ_0 means the quality factor drop, i.e. the difference between the quality factor at the stress-free state and at maximal stress ($Q_{\alpha\, max}$, $Q_{\beta\, max}$), when all pores are closed.

"Q-σ" DOUBLE RELAXATION MODEL

The model in Section 3 describes the main characteristics of the process [3], but it was found that some samples showed a slightly different behaviour, with the measured and estimated velocities having a somewhat larger data distance in the small and high-pressure ranges. (We also have to mention that since the determination of the quality factor is much more challenging from the point of view of measurement techniques, therefore the measured data themselves contain more error.) Thus, the further development of the model seemed to be advantageous. If the rock is exposed to increasing load, several different events may arise simultaneously: closure of microcracks and spherical pore space, friction on grain or crack surfaces, compression of matrix particles, etc. These intrinsic processes can be linked to extensive quantities that show pressure dependence. Thus, a new model is introduced to handle the effects of two pressure dependent relaxation processes. It is shown in this study that the new "Q-σ" Double Relaxation Model (DRM) characterizes the pressure dependence of quality factors more accurately than the Single Relaxation Model.

The extensive quantities (X_1, X_2) introduced in *Equation (1)* have effects on the quality factors as well, therefore in addition to *Equation (1)* the following differential equation

$$dQ_i = -\kappa_i dX_i \tag{6}$$

is also valid, where $i = 1,2$ and κ_i is a proportionality factor, a new material characteristic. *Equation (1)* declares that an increase in pressure results in the decrease of extensives, where the relaxation parameter is λ. Merging the solution of *Equation (1)* and *Equation (6)* we get

$$\left.\begin{aligned} dQ_1 &= \kappa_1\lambda_1 X_{01}\, exp(-\lambda_1\sigma)d\sigma \\ dQ_2 &= \kappa_2\lambda_2 X_{02}\, exp(-\lambda_2\sigma)d\sigma \end{aligned}\right\}.$$

We are looking for the total effect of the arising intrinsic processes, i.e.

$$dQ = dQ_1 + dQ_2 = \left\{\kappa_1\lambda_1 X_{01}\, exp(-\lambda_1\sigma) + \kappa_2\lambda_2 X_{02}\, exp(-\lambda_2\sigma)\right\}d\sigma,$$

and its solution can be defined as

$$Q = K - \kappa_1 X_{01}\, exp(-\lambda_1\sigma) - \kappa_2 X_{02}\, exp(-\lambda_2\sigma), \tag{7}$$

where K is the integration constant, which can be calculated according to $K = Q_0 + \kappa_1 X_{01} + \kappa_2 X_{02}$ (Q_0 is the quality factor measured at stress-free state, $\sigma = 0$).

The notations $\Delta Q_1 = \kappa_1 X_{01}$ and $\Delta Q_2 = \kappa_2 X_{02}$ as quality factor increments are introduced for the two relaxation processes. With them *Equation (7)* can be rewritten as

$$Q = Q_0 + \Delta Q_1 (1 - exp(-\lambda_1 \sigma)) - \Delta Q_2 (1 - exp(-\lambda_2 \sigma)).$$

The model is valid in the reversible range and it assumes that the quality factor increases from the Q_0 value to the Q_{max} quality factor at maximal pressure. This quantity can be written as the sum of quality factor at the stress-free state and the quality factor increments caused by the pressure increase $Q_{max} = Q_0 + \Delta Q_1 + \Delta Q_2$.
Applying this formula, the model equation can be defined

$$Q = Q_{max} - \Delta Q_1 exp(-\lambda_1 \sigma)) - \Delta Q_2 exp(-\lambda_2 \sigma)). \quad (8)$$

Equation (8) means the forward problem, which is solved in the framework of a quality-checked inversion procedure. The solution provides the estimates for the model parameters Q_{max}, ΔQ_1 and ΔQ_2, λ_1 and λ_2.

APPLICATION OF THE MODELS

To show the improvement and benefit of the new model, laboratory P-wave quality factor data were processed according to both the Single and Double Relaxation Models. In the case of the SRM 3 model parameters (Q_0, ΔQ_0, λ) of *Equation (5)* and for the DRM 5 model parameters (Q_{max}, ΔQ_1, ΔQ_2, λ_1, λ_2) in *Equation (8)* were estimated in separate inversion procedures. Since the inverse problem is overdetermined (the number of data N is greater than the number of model parameters M) the Gaussian Least Square Method was used. The model parameters used in the last iteration step are considered as the results of the inversion procedure. After determining the model parameters in the inversion procedure, the quality factors can be calculated for any arbitrary stresses.

The variance of the *i*-th estimated model parameter (var_i) is given by the *i*-th elements of the main diagonal in the covariance matrix ($cov(m)$)

$$var_i = \sqrt{cov(\boldsymbol{m})_{ii}}.$$

The accuracy of the inversion can be described with the misfit between the measured and calculated data, which is given by the relative distance in data space

$$D = \sqrt{\frac{1}{N}\sum_{i=1}^{N}\left(\frac{d_i^{(m)} - d_i^{(c)}}{d_i^{(c)}}\right)^2} \cdot 100\ [\%],$$

where $d_i^{(m)}$ is the *i*-th measured data and $d_i^{(c)}$ is the *i*-th calculated data.

For the determination of the P wave quality factors, data measured by Yu et al. [4] on two coal samples were processed. The "Coal-15" sample was investigated under saturated condition, and "Coal-16" was a dry sample with density 1.37 g/cm^3 and porosity 2.31%. The results are plotted in *Figures 1* and *2*: the SRM curve with blue on the left-hand side, the DRM curve with green on the right-hand side. Red dots indicate the measured quality factors. The estimated parameters and their errors, and the relative data distance are shown in *Table 1* (DRM) and *Table 2* (SRM). As can be seen graphically and from the relative data distances, the new Double Relaxation Model provides a more precise description of the pressure dependence of quality factors.

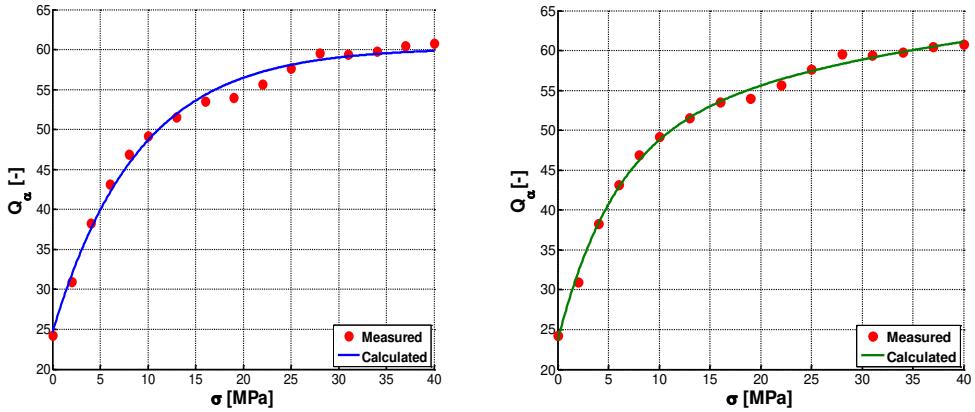

Figure 1. *Pressure dependent P wave quality factor of the wet sample "Coal-15" determined with the SRM (left curve) and DRM (right curve)*
Measured data (red dots) by Yu et al. [4]

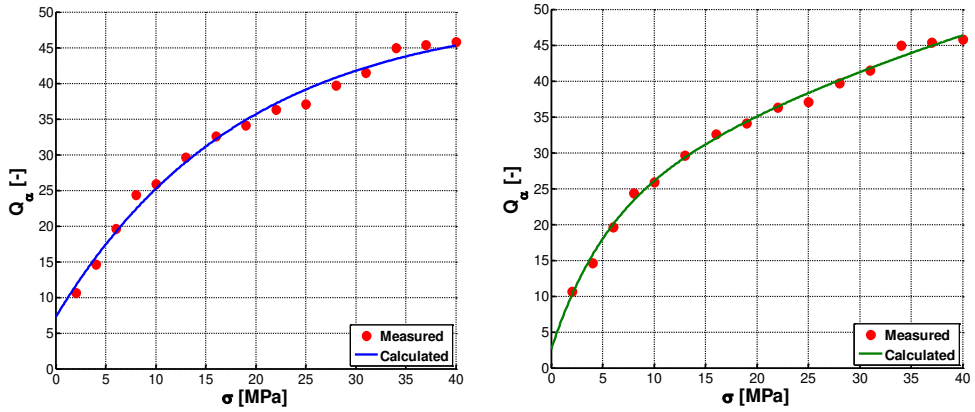

Figure 2. *Pressure dependent P wave quality factor of the dry sample "Coal-16" determined with the SRM (blue curve) and DRM (green curve)*
Measured data (red dots) by Yu et al. [4]

Table 1

Estimated model parameters with their error, relative data distances in the last iteration step (D) with the use of the "Q-σ" SRM

Sample	Q_0 [–]	ΔQ_0 [–]	λ [1/MPa]	D [%]
Coal – 15 (wet)	24.65 (±0.78)	35.60 (±0.79)	0.1122 (±0.0064)	1.95
Coal – 16 (dry)	7.22 (±1.14)	43.01 (±0.05)	0.0541 (±0.0060)	4.30

Table 2

Estimated model parameters with their error, relative data distances in the last iteration step (D) with the use of the "Q- σ" DRM

Sample	Q_{max} [–]	ΔQ_1 [–]	ΔQ_2 [–]	λ_1 [1/MPa]	λ_2 [1/MPa]	D [%]
Coal – 15 (wet)	69.33 (±20.77)	24.88 (±9.14)	20.79 (±12.02)	0.1808 (±0.0510)	0.0232 (±0.0480)	1.53
Coal – 16 (dry)	79.54 (±65.57)	18.24 (±8.09)	58.70 (±56.34)	0.1947 (±0.1117)	0.0143 (±0.0263)	2.96

CONCLUSIONS

Examples in this paper proved that the suggested "Q-σ" Single Relaxation Model including the effect of one intrinsic process on the pressure dependence of acoustic quality factor can be applied well in practice. Although the results were satisfying for engineering problems (relative data distance smaller than 5%), further development seemed to be desirable. Thus, the new "Q-σ" Double Relaxation Model considers a second relaxation process connecting to a second internal phenomenon during the loading of the rock samples as well. Comparison of the results obtained from SRM and DRM confirmed that the new model provides a more precise description of the pressure dependence of acoustic quality factor. The relative data distances were almost two times smaller for this model.

ACKNOWLEDGMENTS

The described article was carried out as part of the EFOP-3.6.1-16-2016-00011 *Younger and Renewing University – Innovative Knowledge City – institutional development of the University of Miskolc aiming at intelligent specialization* project implemented in the framework of the Szechenyi 2020 program. The realization of this project is supported by the European Union, co-financed by the European Social Fund.

LIST OF SYMBOLS

Symbol	Description	Unit
cov(m)	covariance matrix in parameter space	–
D	relative data distance	%
$d_i^{(c)}$	calculated data at the i-th pressure value	–
$d_i^{(m)}$	measured data at the i-th pressure value	–
$d\sigma$	stress increase	MPa
K	integration constant	–
N	number of measured points	–
M	number of model parameters	–
X	extensive quantity	–
X_0	extensive quantity at stress-free state	–
Q	quality factor	–
Q_0	quality factor at stress-free state	–
Q_{max}	quality factor at maximum pressure	–
var	variance	–
ΔQ	quality factor -drop at pressure σ	–
κ	proportionality factor	–
λ	relaxation parameter	1/MPa
σ	stress	MPa

REFERENCES

[1] Birch, F. (1960). The velocity of compression waves in rocks to 10 kilobars, Part 1. *Journal of Geophysics Research*, 65, pp. 1083–1102.

[2] Walsh, J. B., Brace, W. F. (1964). A fracture criterion for brittle anisotropic rock. *Journal of Geophysical Research*, 69, pp. 3449–3456.

[3] Somogyi Molnár, J., Kiss, A., Dobróka, M. (2015). Petrophysical models to describe the pressure dependence of acoustic wave propagation characteristics. *Acta Geodaetica et Geophysica*, 2015, Doi: 10.1007/s40328-014-0074-4.

[4] Yu, G., Vozoff, K., Durney, D. W. (1993). The influence of confining pressure and water saturation on dynamic elastic properties of some Permian coals. *Geophysics*, 58 (1), pp. 30–38.

Geosciences and Engineering, Vol. 6, No. 9 (2018), pp. 60–74.

TOWARDS TO THE GEOID – A SHORT OVERVIEW OF THE HISTORY OF GRAVIMETRIC MEASUREMENTS IN GEODESY

GÁBOR TIMÁR[1]–DEZSŐ DRAHOS[1]–GÁBOR MOLNÁR[2, 3]–PÉTER VARGA[4]

[1]*Department of Geophysics and Space Science, Eötvös University, Budapest, Hungary*
[2]*MTA-ELTE Geological, Geophysical and Space Sciences Research Group, Budapest, Hungary*
[3]*MTA Research Centre for Astronomy and Earth Sciences, Geodetic and Geophysical Institute, Sopron, Hungary*
[4]*MTA Research Centre for Astronomy and Earth Sciences, Kövesligethy Radó Seismological Observatory, Budapest, Hungary*

Abstract: Horizontal geodesy, producing topographic maps from the 18th century, needs no gravimetric components; it can operate on the basis of angle and some length measurements. Gravimetry appears in geodesy in two specific fields: to define the shape of the Earth and to measure the elevation of specific points to be shown on maps. The earliest gravity measurements led to the refinement of our knowledge about the Earth's shape from the sphere to the ellipsoid of revolution in the 17th century. However, the practical need to apply gravimetry in geodesy appeared in the mid-19th century as Stokes formulated the connection between the shape of the Earth and the local gravity measurements, and also when gravity was confirmed to be crucial to solving the ambiguities in precise levelling. In practice, the usage of the formula of Stokes was delayed by a century, as the number of local measurements increased rapidly and covered also the oceans. In addition, the original formula had to be interpreted in summarizing form to apply to real geoid computation. This led to a wholly gravimetric solution of the geoids in 1952 (in the USSR) and in 1957 (in the USA); the latter occurred in the same year of the first spacecraft launch, offering a new tool for determination of the Earth's shape. Nowadays, gravimetry provides the fine, high order and rank components of global geoid models.

Keywords: *gravimetry, geodesy, historical geodesy, history of gravimetry, physical geodesy*

INTRODUCTION: THE GOALS OF GEODESY, MEASUREMENT TYPES

Geodesy has had two important goals throughout history:

1. To determine the size and shape of the Earth, and
2. To determine the position of terrain objects, according to the Earth model.

The practical need for geodesy was in producing maps of the Earth's surface. This is done by defining geodetic base points: defining well-identified points on the mapped surface and giving their coordinates. A set of these points unified in one system is called a geodetic frame or geodetic datum. The base points are drawn on the map, while the terrain between them is filled by local detail measurements. The quality of the horizontal control of the maps is based on the quality of the geodetic frame.

In fact, the two above tasks of geodesy – remaining strictly at horizontal purposes, not applying height measurements – can be completed solely by angle and length measurements (for direct geographic longitude determinations, measurement of local time and/or time differences is also applied). Since the accuracy of angle measurements was much more precise than the determination of length, the majority of the field surveys were determinations of angles. However, similarly to triangles, which cannot be defined by their angles alone, the scale of the networks was determined by baseline measurements. Even the long-distance arc surveying campaigns of Snell (1617) and Cassini (1720) were accomplished by this method. The difference between the accuracy of these methods in practice was acknowledged by Bessel & Baeyer (1838), who proposed using shorter baselines.

The first gravity measurements were the determination of the period of a pendulum. The pendulum clock was invented by Christiaan Huygens (1673), who also gave the relationship between its time period and the time of a falling object from the half height of the pendulum length. The pendulum clock was so much more precise than any earlier method for time measurement that it immediately became the standard tool for any timing, also in astronomy. So when Jean Richer was sent to Cayenne to take measurements about the celestial position of the planet Mars, there he re-calibrated his pendulum clock, which had been set up in Paris earlier. He detected and later published (Richer, 1679) that the pendulum is slower in lower latitudes *(Figure 1)*. This was the first hint that the shape of the Earth was not a perfect sphere but rather an ellipsoid of revolution. This was the first occasion when gravity measurements – in fact, the very first ones – contributed to the knowledge of geodesy, especially to Point 2 above. Some years later, in 1676, the observation was confirmed by E. Halley on the Island of St. Helena (Halley & MacPike, 1937), supporting the theory of gravity by Newton (1687) and also the concept of Huygens (1690) describing the sea surface as an ellipsoid of revolution.

CHAPITRE X.

OBSERVATIONS PHYSIQUES.

ARTICLE I.

De la longueur du pendule à ſecondes de temps.

L'UNE des plus conſiderables Obſervations que j'ay faites, eſt celle de la longueur du pendule à ſecondes de temps, laquelle s'eſt trouvée plus courte en Caïenne qu'à Paris: car la meſme meſure qui avoit eſté marquée en ce lieu-là ſur une verge de fer, ſuivant la longueur qui s'eſtoit trouvée neceſſaire pour faire un pendule à ſecondes de temps, ayant eſté apportée en France, & comparée avec celle de Paris, leur difference a eſté trouvée d'une ligne & un quart, dont celle de Caïenne eſt moindre que celle de Paris, laquelle eſt de 3. pieds 8. lignes $\frac{1}{4}$. Cette Obſervation a eſté réïterée pendant dix mois entiers, où il ne s'eſt point paſſé de ſemaine qu'elle n'ait eſté faite pluſieurs fois avec beaucoup de ſoin. Les vibrations du pendule ſimple dont on ſe ſervoit, eſtoient fort petites, & duroient fort ſenſibles juſques à cinquante-deux minutes de temps, & ont eſté comparées à celles d'une horloge tres-excellente, dont les vibrations marquoient les ſecondes de temps.

Figure 1. *Excerpt the report of Richer (1679) about the different period of the same pendulum in Paris and Cayenne*

OFFSPRING TO GEODESY: FROM A SPHERE TO AN ELLIPSOID

The traditional angular and length survey in France aiming to determine the size of the Earth (Picard 1671) was burdened by some errors, so at first it appeared that the polar radius might be longer than the equatorial one (Cassini 1720), which was obviously against the new theory of Newton (1687). To solve this contradiction, the Royal French Academy sent two expeditions to distant regions of the planet; one near to the Equator, the other to the polar region. These surveys clarified the situation, verifying the concept of the flattened ellipsoid (without real gravity measurements). A staff member of the polar expedition, Alexis Clairaut, used his idle time while measuring in the sparsely populated Finnish-Swedish border area (Maupertuis 1738) to deriving a connection between the geometric flattening of the terrestrial ellipsoid and the ratio of the equatorial and polar gravities (in more precise terms: gravity accelerations; Clairaut 1743; *Figure 2*). This formula is the base of the description of normal gravity acceleration as a function of the geodetic latitude, which was in the forefront of geodesy in the first half of the 20th century, 200 years after the work of Clairaut. His name was even cited in the publication stream concerning the gravitational shape of the planet (Stokes 1849a; *cf.* also Fasching 1931; Nagy 1999).

250 FIGURE

précedente par Π, nous pourrons nous contenter de la diviſer par $2cA$, qui exprime la peſanteur ſur le Globe compoſé de la même maniere que le Spheroïde. Nous aurons donc

$$2\delta + \varphi - \frac{3D}{5A} = \frac{P-\Pi}{\Pi}.$$

Si on ſe rappelle préſentement qu'on a prouvé dans le §. XXXVII. qu'afin que le Fluide placé ſur la ſurface du Spheroïde pût être en équilibre, il falloit que $10\delta A - 2D = 5A\varphi$, on verra qu'on peut mettre dans la quantité précedente $3\delta - \frac{3}{2}\varphi$ à la place de $\frac{3D}{5A}$. La ſubſtitution faite, il viendra $\frac{5}{2}\varphi - \delta = \frac{P-\Pi}{\Pi}$. Or $\frac{5}{4}\varphi$ eſt §. XXX. la valeur de ϵ ou de l'ellipticité du Spheroïde homogene : donc $\frac{P-\Pi}{\Pi} = 2\epsilon - \delta$.

Figure 2. *The original publication of the theorem of Clairaut (1643), the connection between the geometric and gravimetric flattening of the Earth*

THE GEOID APPEARS

The realization that the physical shape of the Earth is not a perfect ellipsoid originated again from angular measurements. Triangulated geodetic coordinates of a point (derived from an astronomical 'fundamental point' by field triangulation) were different from the astronomic locations determined directly at these points. These differences were first identified by Boscovich (1760) and measured by Laplace (1799) at the endpoints of the French meridian arc, and first systematically interpreted by Gauss (1828) to mean that the equipotential surface of our planet forms a more complex shape, later called a geoid (Listing 1872).

However, we repeat, the horizontal control of traditional geodesy applied in topographic mapping till the end of the 20th century can be carried out flawlessly by a combination of angular measurements (astronomical observations and triangulation) and baseline measurements. The standard method was summarized in a clear and ambitious book of Helmert (1880) – its content can be applied even nowadays, if we prefer not to apply space geodesy and GPS. Even the handling of the geoid shape was solved by these methods and their standard processing (Helmert 1872).

694 MR. STOKES, ON THE VARIATION OF GRAVITY

Integrating by parts, and observing that γ vanishes with ζ, we get

$$\gamma = 2\zeta^{-1}Z + 3\int_0^\zeta \zeta^{-2} Z\, d\zeta.$$

The last integral may be obtained by rationalization. If we assume $R = w - \zeta$, and observe that $Q_0 = 1$, $Q_1 = \cos\psi$, and that $w = 1$ when ζ vanishes, we shall find

$$\int_0^\zeta \zeta^{-2} Z d\zeta = \cos\psi \,.\, \log\frac{w - \cos\psi}{1 - \cos\psi} - (1 + \cos\psi)\frac{w-1}{w+1} - 2\cos\psi \,.\, \log\frac{w+1}{2}.$$

When $\zeta = 1$ we have $Z = (2 - 2\cos\psi)^{-\frac{1}{2}} - (1 + \cos\psi)$, $w = 1 + 2\sin\frac{\psi}{2}$, and

$$\int_0^\zeta \zeta^{-2} Z d\zeta = -2\sin\frac{\psi}{2}\left(1 - \sin\frac{\psi}{2}\right) - \cos\psi \log\left\{\sin\frac{\psi}{2}\left(1 + \sin\frac{\psi}{2}\right)\right\}.$$

Putting $f(\psi)$ for the value of γ when $\zeta = 1$, we have

$$f(\psi) = \operatorname{cosec}\frac{\psi}{2} + 1 - 6\sin\frac{\psi}{2} - 5\cos\psi - 3\cos\psi \log\left\{\sin\frac{\psi}{2}\left(1 + \sin\frac{\psi}{2}\right)\right\} \ldots\ldots (45)$$

In the expression for Δu, we may suppose the line from which θ' is measured to be the radius vector of the station considered. We thus get, on replacing $F(\theta', \phi')$ by $G^{-1}\Delta g$, and employing the notation of Art. 22,

$$\Delta u = \frac{1}{4\pi G}\int_0^\pi \int_0^{2\pi} \Delta g \,.\, f(\psi) \sin\psi\, d\psi\, d\chi. \ldots\ldots\ldots\ldots\ldots\ldots\ldots\ldots (46)$$

32. Let $\Delta g = g' + \Delta' g$. Then $\Delta' g$ is the excess of observed gravity reduced to the level of the sea by Dr. Young's rule over calculated gravity; and of the two parts g' and $\Delta' g$ of which Δg consists, the former is liable to vary irregularly and abruptly from one place to another, the latter varies gradually. Hence, for the sake of interpolating between the observations taken at different stations, it will be proper to separate Δg into these two parts, or, which comes to the same, to separate the whole integral into two parts, involving g' and $\Delta' g$ respectively, so as to get the part of Δu which is due to g' by our knowledge of the height of the land and the depth of the sea, and the part which depends on $\Delta' g$ by the result of pendulum-experiments. It may be observed that a constant error, or a slowly varying error, in the height of the land would be of no consequence, because it would enter with opposite signs into g' and $\Delta' g$.

Figure 3. *The original publication of Stokes (1849b); Equation (46) on this page is the connection between the observed gravity acceleration (Δg) and geoid undulation (Δu)*

Meanwhile, Stokes (1849b) had revealed a formula that is surprising at first sight: the connection between the 'geoid height' (the vertical distance of the geoid surface from the fitting ellipsoid) and the distribution of the measured gravity acceleration data *(Figure 3)*. At that time, this was a purely theoretic rule: it contains the surface integral of gravity from the entire Earth surface (Helmert 1910) and the geoid heights (in modern terms: the geoid undulations) were expressed from an ellipsoid, whose geometric center was at the mass center of the planet. Both things seemed beyond any reality. Although this method seemed more appropriate globally than the one proposed by Helmert (1880; 1884; the line integral of the deflections of vertical), for its practical solution many improvements to gravimetry were required.

THE THIRD DIMENSION: HOW TO DEFINE THE SEA LEVEL IN THE CONTINENTS

The main task of topographic maps was and is to aid movement in the field (especially military maneuvers). Therefore, besides the signs of planar topographic elements, elevations of the terrain also have great importance. Indication elevations of distinct points or giving relief characteristics of the terrain by hachures or by contour lines need height measurements, called levellings. This kind of survey needs a zero level (vertical datum) and a method to measure the heights above (or below) the datum. Sea level was selected as the vertical datum long ago, and its local variations were handled by defining distinct 'zero points' along the shoreline, generally in important harbors of the different countries. Measuring the elevation above these points was a harder nut to crack. The field survey settled on measuring the height differences along the local vertical and summarizing them. However, as the equipotential surfaces of the Earth are not exactly parallel to each other, this method leads to ambiguities; the measure height of a summit depends on the line of levelling.

Of course, adjustment methods of these measured data were applied shortly. However, a Czech-born Austrian military engineer, Robert Daublebsky von Sterneck, offered a theoretically correct solutionthat could also be applied in the field. Since the 'distance between the equipontential surfaces' is a function of gravity acceleration, this latter quantity should also be measured along the survey line. By multiplying the elementary height differences by the local gravity, we can sum up the potential differences between the end points, practically between the 'zero elevation point' and our target (Sterneck 1881). Sterneck (1887) even invented a new pendulum apparatus to make

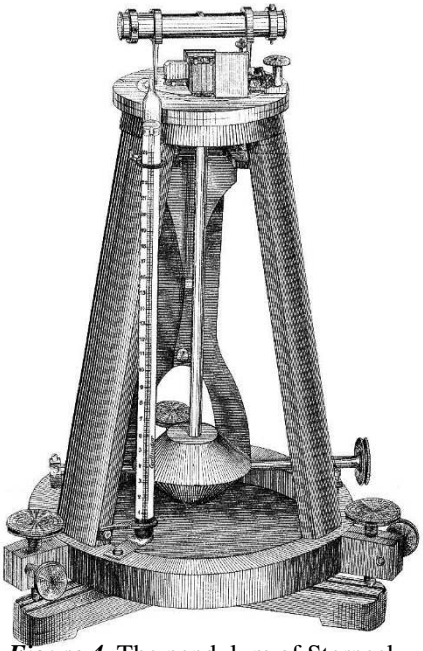

Figure 4. The pendulum of Sterneck (1887), a leap to higher accuracy in field gravity measurements

field gravity observations more feasible *(Figure 4)*. To obtain the metric height from the geopotential value needs a procedure of local gravity function with the elevation, which is a model leading to normal or to orthomertic heights, depending on this model. The whole method is the first obvious demand for gravity measurements directly for geodetic field survey purposes.

STOKES IN PRACTICE 1: MEASURE MORE

The first of the two problems mentioned above that prevented application of the formula of Stokes in practice is the territorial cover of the gravity measurements. In the late 19th and early 20th century, only some parts of the planet had – sparse – cover of gravity measurements (Borass 1911). Moreover, the methods could be applied only to the continents, only about one third of the whole surface.

Seaborne measurements started in the early years of the 20th century (Hecker 1910; Briggs 1916). An important improvement was to move these measurements from surface ships to submarines, decreasing the noise from surface waves (Vening Meinesz 1925; *Figure 5*). Up until the 1960s, the US Navy commissioned all nuclear submarine staffs to gather relative gravimetric data when cruising, independently from their current military tasks (Warner 2002; Clifford J. Mugnier, pers. comm. 2018).

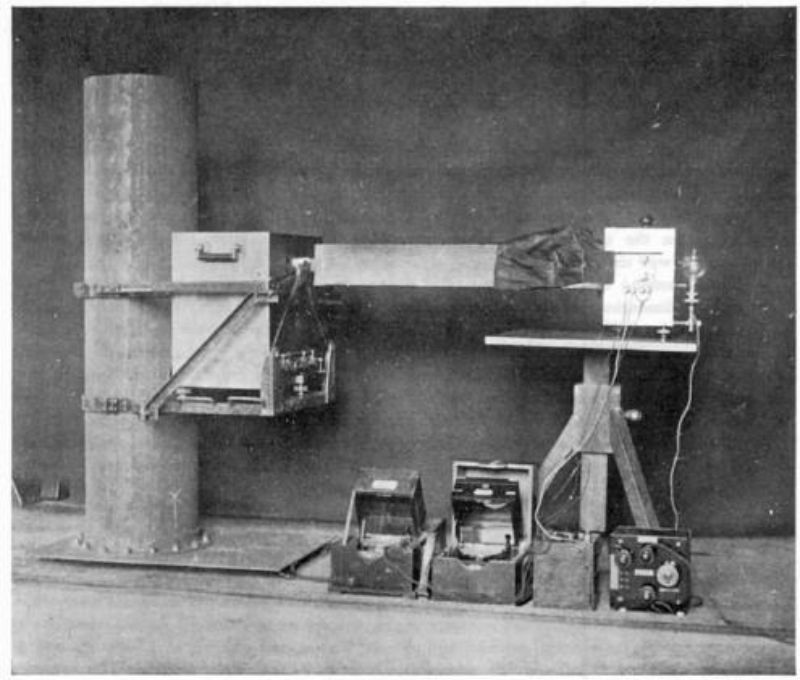

New Pendulum Apparatus.
Left: New Pendulum Apparatus in its cradle.
Right: Recording and Light Apparatus.
Below: Chronometer and Resistance of Swan Electric Arc Lamp.

Figure 5. *The double pendulum apparatus of Vening Meinesz (1932) applied on board a submarine*

The 20th century brought a great leap in the technology of gravimetric measurement. The traditional pendulum was first challenged by the torsion balance (Eötvös 1906) and later by the relative gravimeters (LaCoste 1935; LaCoste & Romberg 1945), both encouraged by the oil industry. The LaCoste-Romberg type gravimeters were applied also in vehicle-mounted mode, allowing the very rapid extension of the gravity measurements, both on land and sea (Hirvonen 1956). Thus, the territorial cover became nearly global. Meanwhile, the theory could be applied without fully global cover of the data (Heiskanen 1957; Biró 1981; Kenyeres 1993). Of course, in the present-day geophysics, geodesy and gravimetry, the above-mentioned tools are more or less obsolete. Modern gravity measurements apply rather to airplane and satellite-borne detection; the impact of satellite geodesy was a real revolution, offering a different way of geoid determination, no longer connected to field gravity measurements.

STOKES IN PRACTICE 2: INTEGRATION OF DISCRETE MEASUREMENTS

The formula of Stokes gives the elevation of the geoid above the ellipsoid (the geoid height, also termed the geoid undulation) as a surface integral of multiplication of the observed free-air corrected gravity by a core function. In theory, to solve it we need the free-air gravity measurements from all points of the surface, both from continents and oceans. This cannot be provided, of course, as the gravity measurements represent only points, albeit a lot of points worldwide. The problem captured the imagination of Weikko A. Heiskanen, a leader of the Finnish geodetic efforts between the world wars (Kakkuri 2001), who gave this exercise to his doctoral students. In practice, the original integral formula was translated to a summation according to the measurements, or more precisely, the sets of measurement organized into latitude-longitude quadrangles (Hirvonen 1934). This way, the original integral was replaced by a finite convolution, which could be accomplished even without computers.

This method was later applied to estimate the real geoid part of the Mediterranean area and some adjacent territories, with application of isostatic considerations by another colleague of Heiskanen (Tanni 1948), and his work can be acknowledged as the first application of the geoid models in geodynamic interpretations.

GLOBAL 3D GEODESY

Already in the USA, working at Ohio State University, Heiskanen (1951) outlined the problem of the World Geodetic System – a unified geodetic datum in 3D sense, practically a unification of the existing and constructed continental datums. From the geophysical point of view, the problem was the placement of a well-defined ellipsoid with respect to the physical Earth. It intended to place the geometric center of the ellipsoid at the mass center of the planet. In the practice, this can be done by defining a set of base points on the surface and giving their geodetic coordinates in this ellipsoid, in the World Geodetic System.

Heiskanen led this project, providing the global gravimetric geoid based on the work of Hirvonen (1933) and Tanni (1948), and also using the exponential expansion of the local gravimetric measurements available from the whole world in the 1950s

(Hirvonen, 1956). Similarly to the space race, the USSR reached the 'first prize', providing the first gravimetric geoid (Zhongolovich 1952; *Figure 6*). This geoid

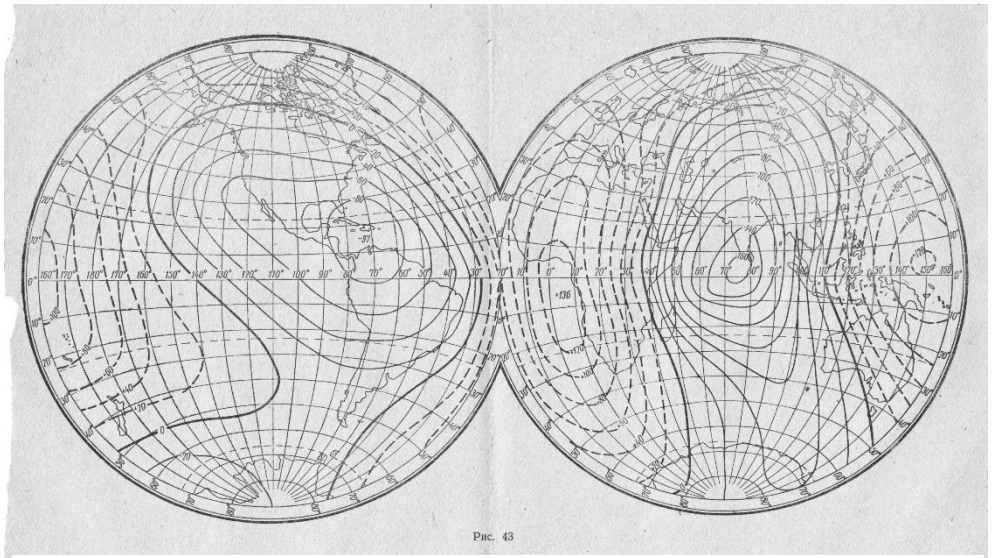

Figure 6. *The first global geoid model, derived purely from gravimetric data* (Zhongolovich 1952)*, based on a base ellipsoid with a flattening of 1:296.6* (reached in Bronar et al. 1961)

model had global coverage, based on the spherical harmonic solution, a tool first proposed to use to describe the shape of the Earth by Jeffreys (1924), up to the order and rank of eight, the top product of the gravimetric geodesy (or in Heiskanen's terms, the 'physical geodesy'). The American solution was the 'Columbus geoid' (Ohio State University is located in Columbus, capital city of Ohio; Heiskanen 1957; see *Figure 7*). Albeit not providing a full coverage of geoid heights of the world, the Columbus geoid was appropriate data to define the first real World Geodetic Systems (WGSs).

One of the most important problems to be solved was the spatial displacement of the base ellipsoid, serving as a 'zero' surface for geoid undulation calculations. The starting point was, of course, to use local continental datums for different continents (for a summary, see Fischer 1959). However, for a global solution the continental datums have to be connected into one, global system (Fischer 1975). The applied methods were direct (radio signals), semi-indirect (astronomic) and indirect – the latter is based purely on gravimetry (Heiskanen 1955). The final displacement of this surface occurred at, according to *Figure 7* of Heiskanen (1957), the point where the numbers of the positive and negative 5° × 5° average free-air anomaly values are not so far from each other (536 vs. 422; *Figure 8*). The solution has forms an important parameter of the flattening of the datum ellipsoid: through the Clairaut formula it affects the gravimetric flattening, a main parameter of the gravimetric normal formula, used for free-air corrections.

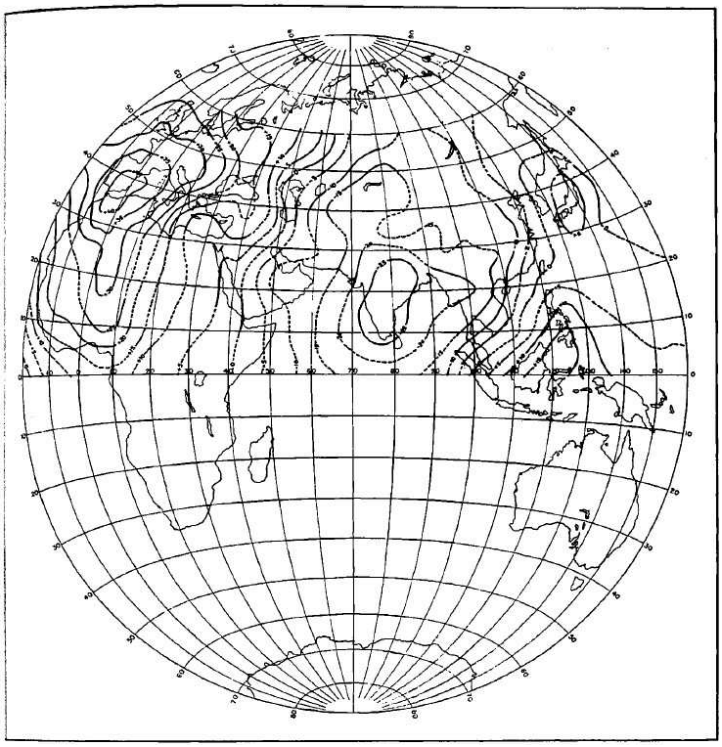

Figure 7. *The eastern hemisphere part of the Columbus geoid* (Heiskanen 1957), *based also on gravimetric data, computed with flattening of 1/297.4 of the base ellipsoid. The geoid pattern is similar in big features but different in details than that in Figure 6 because of the different ellipsoid parameters*

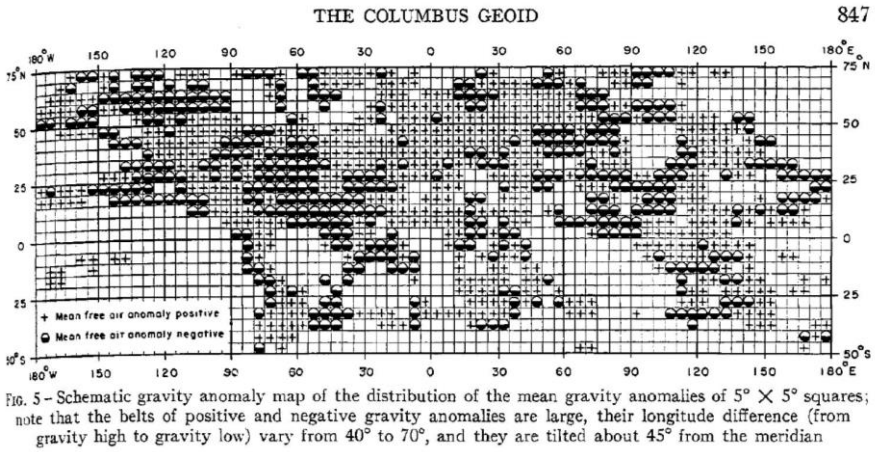

FIG. 5 – Schematic gravity anomaly map of the distribution of the mean gravity anomalies of 5° × 5° squares; note that the belts of positive and negative gravity anomalies are large, their longitude difference (from gravity high to gravity low) vary from 40° to 70°, and they are tilted about 45° from the meridian

Figure 8. *One of the input datasets of the Columbus geoid; the 5° × 5° averaged free-air gravity datasets (blank rectangles refer to no data, plus signs indicate positive values, round signs indicate negative values). Note the almost equalized number (536 vs 422) of the positive and negative cells* (Heiskanen 1957)

The first spacecraft was launched by the Russians in the year of the publication of the Columbus geoid, followed shortly by the first American satellite. This offered a new, absolute method to survey the shape of the Earth, and also the geoid undulations. The very first results came instantly, with the third order and rank geoid model showing a 'pear shape' of the Earth (O'Keefe et al. 1959). From this date, geoid models were based on the combination of satellite and surface gravity data. Low order and rank coefficients are from computed using the changes of satellite orbit elements while high spatial frequency elements are provided by local gravity measurements, if available (Lemoine et al. 1998).

However, gravimetry offered one more service to space programs. The first global geodetic datum, verified by the U. S. Department of Defense (DoD WGS 1960; Fischer 1960) used the data of Heiskanen (1957). This was the geodetic datum used for locating the spacecraft control stations of the Mercury, the first human spaceflight program in America – which explains the *vulgo* name of this reference system, the 'Mercury Datum'. Simultaneously to these achievements, satellite Doppler technology offered the first possibility to define local geodetic base points in a real Earth-centered coordinate system (Drahos et al. 1970). Modern geoid solutions (e.g. Tóth et al. 2009) use both satellite and gravity input data, and Eötvös-type gravity gradients (Tóth et al. 2002; Szafián et al. 2006) and directly measured deflections of vertical (Tóth & Völgyesi, this volume) are also applied.

NOWADAYS: GLOBAL 4D GEODESY

Progress, however, has not stopped with satellite gravimetry and geodesy. On the contrary, modern technologies allow us to determine also the temporal variations of the potential field, thus of the geoid surface. To avoid repeated worldwide field gravity campaigns, which are extremely difficult to organize, the measurements are made by satellite-borne detectors (see e.g. Seeber 2003; Csapó & Földváry 2006; Tóth & Földváry 2015). The 'breathing' of the geoid can be detected to millimeter-centimeter accuracy and data representation, while non-periodic processes can also be mapped, such as the effects of vertical crustal movements (Wang et al. 2009).

For more detailed historic reviews of the progress of gravity measurements and identifying the shape of the Earth, we suggest reading Fischer (1975) and Torge (2001).

REFERENCES

[1] Bessel, F. W., Baeyer, J. J. (1838). *Gradmessung in Ostpreussen und ihre Verbindung*. Berlin: Königlichen Akademie der Wissenschaften, p. 452.

[2] Biró, P. (1981). Zur Anwendung der Stokes'schen Formel für zeitliche Schwereänderungen. *Zeitschrift für Vermessungswesen*, 106, pp. 523–531.

[3] Borrass, E. (1911). *Bericht über der relative Messungen der Schwerkraft mit Pendelapparaten in der Zeit von 1808 bis 1909: und über ihre Darstellung im Potsdamer Schweresystem*. Berlin: G. Reimer, p. 288.

[4] Boscovich, R. J. (1760). *De recentissimis graduum dimensionibus et figura, ac magnitudine Terrae inde derivanda*. Supplementum ad nota min Vers. 667, Philosophiae Recentioris e Benedicto Stay, Libri X, Tomus II, Roma, pp. 406–426.

[5] Briggs, L. J. (1916). A new method of measuring the acceleration of gravity at sea. *Proceedings of the National Academy of Sciences of the United States of America*, 2 (7), pp. 399–407.

[6] Bronar, V. V., Magnitskiy, V. A., Shimberev, B. P. (1961). Теория фигуры Земли. Москва: Геодезиздат, p. 256.

[7] Cassini, J. (1720). *De la grandeur et de la figure de la Terre*. Paris: De l'Imprimeire Royale, p. 306.

[8] Clairaut, A. (1743). *Théorie de la figure de la Terre, tirée des principes de l'hydrostatique*. Paris: Durant Libraire, p. 305.

[9] Csapó G., Földváry L. (2006). A magyarországi gravimetria története napjainkig. *Geodézia és Kartográfia*, 59 (7), pp. 23–30.

[10] Drahos, D., Ferencz, Cs., Ferencz, I., Horváth, F., Tarcsai, Gy. (1970). Some theoretical contributions concerning Doppler geodetical measurements. *Space Research*, 10, pp. 43–53.

[11] Eötvös, R. (1906). *Bestimmung der Gradienten der Schwerkraft und ihrer Niveauflächen mit Hilfe der Drehwaage. Verhandl. d. XV. allg. Konferenz der Internat. Erdmessung in Budapest, Bd. I.*, pp. 319–350.

[12] Fasching, A. (1931). Les diagrammes de la formule de Clairaut (1743) pour la variation de la pésanteur normale. *Bulletin Géodesique*, 29, pp. 6–19.

[13] Fischer, I. (1959). A tentative world datum from geoidal heights based on the Hough ellipsoid and the Columbus geoid. *Journal of Geophysical Research*, 64 (1), pp. 73–84.

[14] Fischer, I. (1960). An astrogeodetic world datum from geoidal heights based on the flattening f=1/298.3. *Journal of Geophysical Research*, 65 (7), pp. 2067–2076.

[15] Fischer, I. (1975). The figure of the Earth – Changes in concepts. *Geophysical Surveys*, 2, pp. 3–54.

[16] Gauss, C. F. (1828). *Bestimmung des Breitenunterschiedes zwischen den Sternwarten von Göttingen und Altona*. Göttingen: Vandenhoeck und Ruprecht, p. 84.

[17] Halley, E., MacPike, E. F. (1937). *Correspondence and Papers of Edmond Halley*. Oxford, Clarendon Press, pp. 39–41.

[18] Hecker, O. (1910). Bestimmung der Schwerkraft auf dem Schwarzen Meere und an dessen Küste sowie neue Ausgleichung der Schwerkraftmessungen auf dem Atlantischen, Indischen und Groszen Ozean. *Zentralbureau der Internationalen Erdmessung, Veröffentlichungen N. F.*, 20, pp. 1–160.

[19] Heiskanen, W. (1951). On the world geodetic system. *Publications of the Finnish Geodetic Institute*, 39, pp. 1–25.

[20] Heiskanen, W. A. (1955). Intercontinental connection of geodetic systems. *International Hydrographic Review*, 23 (1), pp. 141–156.

[21] Heiskanen, W. A. (1957). The Columbus geoid. *EOS Transactions of American Geophysical Union*, 38 (6), pp. 841–848.

[22] Helmert, F. R. (1872). *Die Ausgleichungsrechnung nach der Methode der kleinsten Quadrate mit Anwendungen auf die Geodäsie, die Physik und die Theorie der Messinstrumente*. Leipzig: Teubner, p. 348.

[23] Helmert, F. R. (1880). *Mathematischen und physikalischen Theorieen der höheren Geodäsie, Teil I: Die mathematischen Theorieen*. Leipzig: Teubner, p. 631.

[24] Helmert, F. R. (1884). *Mathematischen und physikalischen Theorieen der höheren Geodäsie, Teil II: Die physikalischen Theorieen, mit Untersuchungen über die mathematische Erdgestalt auf Grund der Beobachtungen*. Leipzig: Teubner, p. 610.

[25] Helmert, F. R. (1910). Die Schwerkraft und die Massenverteilung der Erde. In: Furtwängler, Ph., Wiechert, E. (eds.): *Encyklopädie der mathematischen Wissenschaften mit Einschluss ihrer Anwendunge – Geodäsie und Geophysik*. Leipzig: Teubner, pp. 85–177.

[26] Hirvonen, R. A. (1934). The continental undulations of the geoid. *Publications of the Finnish Geodetic Institute*, 29, pp. 1–89.

[27] Hirvonen, R. A. (1956). On the precision of the gravimetric determination of the geoid. *EOS Transactions of American Geophysical Union*, 37 (1), pp. 1–8.

[28] Huygens, C. (1673). Horologium oscillatorium siue de motu pendulorum ad horologia aptato demonstrationes geometricae. Paris: Muguet, p. 161.

[29] Huygens, C. (1690). *Traité de la lumière: avec un Discours de la cause de la pesanteur*. Leiden: Pierre Vander, p. 180.

[30] Jeffreys, H. (1924). *The Earth – Its Origin, History and Physical Constitution*. Cambridge: Cambridge University Press, p. 278.

[31] Kakkuri, J. (2001). Geodetic research in Finland in the 20th century. *Geophysica*, 37 (1–2), pp. 33–77.

[32] Kenyeres, A. (1993). Detailed geoid determination using the combination of truncated global integrals and geopotential models. *Periodica Polytechnica Ser. Civ. Eng.*, 37 (2), pp. 91–108.

[33] LaCoste, L. J. B. jr. (1935). A simplification in the conditions for the zero-length-spring seismograph. *Bulletin of the Seismological Society of America*, 25 (2), pp. 176–179.

[34] LaCoste, L. J. B., Romberg, A. (1945). *Force measuring instrument*. US Patent no. 2,377,889.

[35] Laplace, P. S. (1799). *Traité de Mécanique Céleste*. Tome Second. Paris: Crapelet, p. 382.

[36] Lemoine, F. G., Kenyon, S. C., Factor, J. K., Trimmer, R. G., Pavlis, N. K., Chinn, D. S:, Cox, C. M., Klosko, S. M., Luthcke, S. B., Torrence, M. H., Wang, Y. M., Williamson, R. G., Pavlis, E. C., Rapp, R. H., Olson, T. R. (1998). *The development of the joint NASA GSFC and NIMA geopotential model EGM96*. NASA/TP-1998-206861, NASA Goddard Space Flight Center, Greenbelt, MD USA, p. 575.

[37] Listing, J. B. (1872). *Über unsere jetzige Kenntniss der Gestalt und Grösse der Erde (aus Nachrichten der K. Ges. des Wiss.).* Göttingen: Deiterich, p. 66.

[38] Maupertuis, P. L. M. de (1738). *La Figure De La Terre: Déterminée Par Les Observations De Messieurs De Maupertuis, Clairaut, Camus, Le Monnier, de l'Académie Royale des Sciences, & de M. l'Abbé Outhier, Correspondant de la même Académie, Accompagnés de M. Celsius, Professeur d'Astronomie à Upsal, Faites Par Ordre Du Roy Au Cercle Polaire.* Paris: De L'Imprimerie Royale, p. 184.

[39] Nagy, D. (1999). Theoretical gravity formulae and a mean gravity value. *Acta Geodaetica et Geophysica Hungarica*, 34 (1–2), pp. 23–31.

[40] Newton, I. (1687). *Philosophiae naturalis – Principia mathematica*. London: Pepys, p. 510.

[41] O'Keefe, J. A., Eckels, A., Squires, R. K. (1959). Vanguard measurements give pear-shaped component of Earth's figure. *Science*, 129 (3348), pp. 565–566.

[42] Picard, J. (1671). *Measure de la Terre*. Paris: De l'Imprimeire Royale, p. 30.

[43] Richer, J. (1679). *Observations astronomiques et physiques faites en l'Isle de Caïenne*. Paris: De l'Imprimeire Royale, p. 71.

[44] Seeber, G. (2003). *Satellite geodesy*. Berlin–New York, de Gruyter, p. 589.

[45] Snell, W. (1617). *Eratosthenes Batavus de terrae ambitus vera quantitate.* Leyden: Apud Iodacum à Colster, p. 263.

[46] Sterneck, R. von (1881). Untersuchungen über die Schwere auf der Erde. *Mittheilungen des k. u. k. Militär-Geographischen Institutes*, 1, pp. 89–155.

[47] Sterneck, R. von (1887). Der neue Pendelapparat des k. u. k. Militär-Geographischen Institutes. *Mittheilungen des k. u. k. Militär-Geographischen Institutes*, 7, pp. 83–116.

[48] Stokes, G. G. (1849a). On attractions and on Clairaut's theorem. *The Cambridge and Dublin Mathematical Journal*, 4, pp. 194–219.

[49] Stokes, G. G. (1849b). On the variation of gravity at the surface of the Earth. *Transactions of the Cambridge Philosophical Society*, 8 (5), pp. 672–695.

[50] Szafián P., Timár G., Horváth F. (2006). Régi adat nem vén adat – Az Eötvös-ingás mérési eredmények újraélesztéséről. *Magyar Geofizika*, 46 (4), pp. 146–151.

[51] Tanni, L. (1948). On the continental undulation of the geoid as determined from present gravity materials. *Publications of the Isostatic Institute of I.A.G.*, 18, pp. 1–78.

[52] Torge, W. (2001). *Geodesy*. 3rd edition, Berlin–New York de Gruyter, p. 416.

[53] Tóth, Gy. (2009). New combined geoid solution HGTUB2007 for Hungary. In: Sideris, M. G. (ed.): *Observing our changing Earth*. IAG Symposia 113, pp. 405–412.

[54] Tóth Gy., Földváry L. (2015). Új magyarországi geoidmeghatározás az ötödik generációs GOCE nehézségi erőtér modellek segítségével. *Geomatikai Közlemények*, XVIII/2., pp. 63–74.

[55] Tóth, Gy., Völgyesi, L. (2018). Experiences of QDaedalus measurements. *Geoscience and Engineering*, this volume.

[56] Tóth, Gy., Rózsa, Sz., Ádám, J., Tziavos, I. N. (2002). Gravity field recovery from torsion balance data using collocation and spectral methods. *IGES Bulletin*, 13, pp. 41–49.

[57] Vening Meinesz, F. A. (1925). The determination of gravity at sea in a submarine. *The Geographical Journal*, 65 (6), pp. 501–514.

[58] Vening Meinesz, F. A. (1932). *Gravity expeditions at sea 1923–1930. Vol. I. The expeditions, the computations and the results*. Delft: N.V. Technische Boekhandel en Drukkerij Waltman, p. 109.

[59] Wang, Y. M., Saleh, J., Li, X., Roman, D. R. (2009). The US Gravimetric Geoid of 2009 (USGG2009): model development and evaluation. *Journal of Geodesy*, 86 (3), pp. 165–180.

[60] Warner, D. J. (2002). Politicalgeodesy: the Army, the Air Force and the World Geodetic System of 1960. *Annals of Science*, 59, pp. 363–389.

[61] Zhongolovich, I. D. (1952). Внешнее гравитационное поле Земли и связанные с ним фундаментальные константы. *Труды Институт теоретической астрономии*, с. 3, p. 129.

Geosciences and Engineering, Vol. 6, No. 9 (2018), pp. 87–97.

PARTICLE SWARM OPTIMIZATION ASSISTED FACTOR ANALYSIS FOR SHALE VOLUME ESTIMATION IN GROUNDWATER FORMATIONS

ARMAND ABORDÁN[1, 2*]–NORBERT PÉTER SZABÓ[1, 2]

[1]Department of Geophysics, University of Miskolc,
3515 Miskolc-Egyetemváros, Hungary
[2]MTA-ME Geoengineering Research Group, University of Miskolc,
3515 Miskolc-Egyetemváros, Hungary
[*]gfaa@uni-miskolc.hu

Abstract: Shale volume of different geological formations can be effectively calculated by means of factor analysis. In this study, factor analysis is used to estimate the shaliness of shallow aquifers located in Baktalórántháza, North-East Hungary. For improving the fit between the measured and theoretical wireline logs calculated by the extracted factor model, a global optimization based factor analysis is suggested. Along a section of a thermal water borehole, shale volume is directly calculated from the factor log with a linear relation. By implementing the Particle Swarm Optimization (PSO) procedure in factor analysis, the estimation of the theoretical values of the observed data becomes possible. The result of the global optimization based factor analysis is compared and verified by an independent estimate of natural gamma-ray log based deterministic modeling and core data. A comparative study indicates that there is a strong linear relation between the shale volume and first factor in water-bearing formations, which is also confirmed by earlier results from oilfield wells. The study shows that factor analysis solved by PSO provides reliable in situ estimates of shale content, which may improve the geological modeling of groundwater formations.

Keywords: *Factor analysis, particle swarm optimization, shale volume, global optimization, aquifer, Hungary*

INTRODUCTION

Multivariate statistical methods act powerful tools in applied geosciences. One application is lithology determination in boreholes based on wireline log data. Factor analysis allows us to extract unobserved, hidden petrophysical information from well logging data. With the correlation of the extracted factors to petrophysical parameters, new methods can be developed for advanced lithological modeling. Bücker et al. [1] utilized factor analysis for the evaluation of lithology from logging while drilling data. Hoseinpoor and Aryafar [2] applied factor analysis on compositional geochemical data for the recognition of anomaly zones for the given elements. Szabó [3] used factor analysis for shale volume calculation in freshwater formations, while

Szabó et al. [4] confirmed the results of factor analysis based shale volume estimation by core data.

Factor analysis in its traditional form normally solves a maximum likelihood problem to extract the statistical factors [5]. In this study, we present a novel approach that treats factor analysis as a global inverse problem. In the solution, the measured well logs are approximated by theoretical data directly computed from the factor scores, and the misfit between them is continuously reduced in an optimization procedure.

Nowadays, global optimization methods are one of the most effective tools in solving multivariate optimization problems. Shaw and Srivastava [6] used PSO for the inversion of direct current, induced polarization and magnetotelluric data. Yin and Hodges [7] inverted electromagnetic data using the Simulated Annealing technique to eliminate the starting model dependent nature of linearized inversion algorithms, such as the Marquardt algorithm [8]. Martínez et al. [9] showed that PSO could effectively solve the inverse problem of vertical electrical sounding in a coastal aquifer. Grandis and Maulana [10] utilized PSO for the solution of the magnetotelluric inverse problem.

In this study, we modify the mathematical background of factor analysis with the implementation of PSO to calculate the factor logs more accurately and reduce the misfit between the observed and calculated well logs to a minimum level. It is demonstrated that with proper settings of the control parameters, PSO allows the estimation of the factors in a more accurate and effective way.

TRADITIONAL METHOD OF FACTOR ANALYSIS

Factor analysis is normally used to describe numerous observed quantities with fewer derived variables. In wireline log analysis, the measured logs represent the input variables, which are processed simultaneously to extract the factors. With regression analysis, the factor scores of a given factor can be associated with petrophysical parameters [11]. In this study, we derive the shale volume from the factor logs in a Hungarian freshwater formation.

First, the measured wireline logging data are standardized and collected into the data matrix **D**, so that each column contains the data of different logging tools

$$\mathbf{D} = \begin{pmatrix} D_{11} & D_{12} & \cdots & D_{1K} \\ D_{21} & D_{22} & \cdots & D_{2K} \\ \vdots & \vdots & \vdots & \vdots \\ D_{i1} & D_{i2} & \cdots & D_{iK} \\ \vdots & \vdots & \vdots & \vdots \\ D_{N1} & D_{N2} & \cdots & D_{NK} \end{pmatrix}, \tag{1}$$

where K denotes the number of well log types and N is the total number of measured depth points. Factor analysis is based on the following matrix decomposition

$$\mathbf{D} = \mathbf{F}\mathbf{L}^{\mathrm{T}} + \mathbf{E}, \tag{2}$$

where $\mathbf{F}$ is the N-by-M matrix of factor scores, M is the number of calculated factors. $\mathbf{L}$ denotes the K-by-M matrix of factor loadings and $\mathbf{E}$ is the N-by-K matrix of residuals. According to *Equation (2)*, the measured variables are derived as the linear combination of the factors. The factor loadings show the amount of correlation between the observed variables and the extracted factors. Most of the data variance is represented by the first column of matrix $\mathbf{F}$, which is usually referred to as the first factor log. If the factors are linearly independent, the correlation matrix of the standardized original data is

$$\mathbf{R} = N^{-1}\mathbf{D}^{\mathrm{T}}\mathbf{D} = \mathbf{L}\mathbf{L}^{\mathrm{T}} + \boldsymbol{\Psi}, \tag{3}$$

where $\boldsymbol{\Psi}$ denotes a diagonal matrix of specific variances, which are independent of the variances of the common factors represented in matrix $\mathbf{F}$. The factor loadings can be calculated by the non-iterative approach suggested by Jöreskog [12]

$$\mathbf{L} = \left(diag\mathbf{S}^{-1}\right)^{-1/2}\boldsymbol{\Omega}\left(\boldsymbol{\Gamma} - \theta\mathbf{I}\right)^{1/2}\mathbf{U}, \tag{4}$$

where $\boldsymbol{\Gamma}$ denotes the diagonal matrix of the first M number of eigenvalues of the sample covariance matrix $\mathbf{S}$ and $\boldsymbol{\Omega}$ is the matrix of the first M number of eigenvectors, and $\mathbf{U}$ is an arbitrarily chosen M-by-M orthogonal matrix. In traditional approaches, the factor scores are calculated by the maximum likelihood method. By assuming the hypothesis of linearity, the equation

$$\mathbf{F}^{\mathrm{T}} = \left(\mathbf{L}^{\mathrm{T}}\boldsymbol{\Psi}^{-1}\mathbf{L}\right)^{-1}\mathbf{L}^{\mathrm{T}}\boldsymbol{\Psi}^{-1}\mathbf{D}^{\mathrm{T}} \tag{5}$$

gives an unbiased estimate to the factor scores [13]. Since *Equation (5)* represents a least squares solution weighted by the specific variances, it usually remains sensitive to the level and distribution of instrumental (data) noises and the localities of the objective function to be minimized.

PARTICLE SWARM OPTIMIZATION ASSISTED FACTOR ANALYSIS

PSO is a global optimization technique that is inspired by the social behavior of bird flocking and fish schooling. The basic method was originally developed by Eberhart and Kennedy [14]. PSO is widely used for its easy implementation and efficiency compared to other metaheuristic optimization approaches such as the genetic algorithm. PSO can be effectively used for non-linear inverse problems with large search

domains. In the algorithm of PSO, each particle modifies its own movement and position according to its own best experience and to the whole swarm's best experience. The two equations that define the movement of particles are the position update equation and velocity update equation. By updating these equations iteratively, PSO can converge to the optimal solution.

Given an n-dimensional search space, the *i*-th particle of the swarm can be denoted by an n-dimensional vector, $\mathbf{x}_i = (x_{i1}, x_{i2}, \ldots, x_{in})^T$. The velocity of the particle can also be denoted by an n-dimensional vector, $\mathbf{v}_i = (v_{i1}, v_{i2}, \ldots, v_{in})^T$. The previously visited best position of the *i*-th particle is represented as $\mathbf{p}_i = (p_{i1}, p_{i2}, \ldots, p_{in})^T$. The velocity of the *i*-th particle is refined using the position and velocity update equations

$$\mathbf{x}_i(t+1) = \mathbf{x}_i(t) + \mathbf{v}_i(t+1), \tag{6}$$

$$\mathbf{v}_i(t+1) = w\mathbf{v}_i(t) + r_1c_1(\mathbf{p}_i(t) - \mathbf{x}_i(t)) + r_2c_2(\mathbf{g}(t) - \mathbf{x}_i(t)), \tag{7}$$

where $t = 1, \ldots, T$ denotes the iterations, T is the maximal number of iterations and $I = 1, 2, \ldots, H$ represents the particle index (H is the size of the swarm). Constants c_1 and c_2 are previously set, where c_1 is the so-called cognitive scaling parameter and c_2 is the social scaling parameter. In *Equation (7)*, parameters r_1 and r_2 are uniformly distributed random numbers from the range of 0 and 1. In the same equation, w represents an inertia weight that was introduced by Shi and Eberhart [15] to control the optimization procedure more effectively. Vector $\mathbf{g}$ represents the best position in the search space found by the swarm until the current iteration step. *Figure 1* shows how particle $\mathbf{x}_i(t)$ gets to its new position $\mathbf{x}_i(t + 1)$ by utilizing its own personal best position $\mathbf{p}_i(t)$, the best position found by the whole swarm $\mathbf{g}(t)$ and $\mathbf{v}_i(t)$.

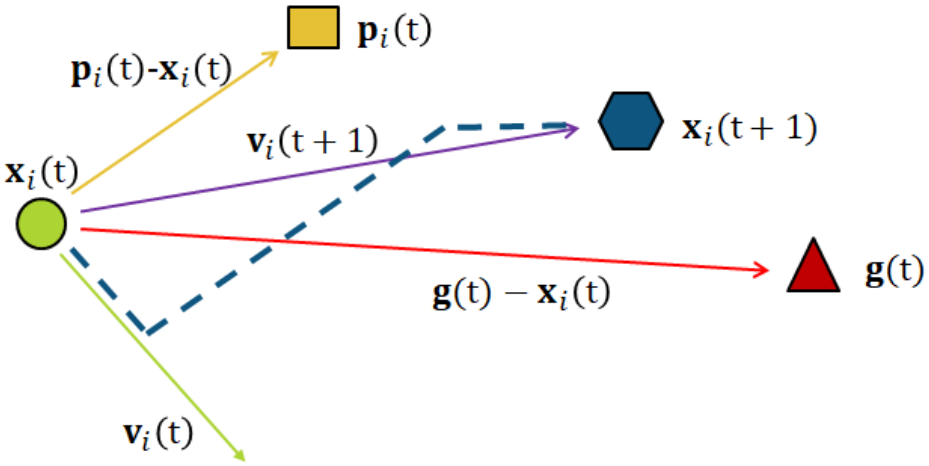

***Figure 1**. Graphical illustration of the searching mechanism of the PSO algorithm*

We alter the traditional method of factor analysis by using the PSO algorithm to estimate the factor scores. We call this PSO based factor analysis FA-PSO. First, the model of factor analysis defined in *Equation (2)* is rearranged as

$$\mathbf{d} = \tilde{\mathbf{L}}\mathbf{f} + \mathbf{e}, \tag{8}$$

where **d** denotes the *KN* length vector of measured (standardized) data, $\tilde{\mathbf{L}}$ denotes the *NK*-by-*NM* matrix of factor loadings, **f** is the *MN* length vector of factor scores and **e** represents the *KN* length vector of residuals. Then the observed data are put into a column vector, from where the matrix of factor loads $\tilde{\mathbf{L}}$ is estimated by *Equation (4)* and then rotated with the varimax algorithm developed by Kaiser [16] for easier interpretation. Then the vector of factor scores **f** are estimated by the PSO algorithm using *Equations (6)–(7)* instead of *Equation (5)*. For solving the inverse problem an objective function has to be defined, which is minimized for finding the optimal solution. In this study, the objective function was chosen based on the L_2 norm as

$$E = \frac{1}{NK}\sum_{i=1}^{NK}\left(d_i^{(m)} - d_i^{(c)}\right)^2 = \min\ , \tag{9}$$

where $\mathbf{d}^{(m)}$ and $\mathbf{d}^{(c)}$ denote the observed and calculated (standardized) well-logging data (column) vectors, respectively. In the frame of the global optimization problem, $\tilde{\mathbf{L}}\mathbf{f}$ represents the calculated data and **d** denotes the measured data. The former product allows the estimation of the theoretical values of well logs, which can also be considered as the solution of the forward problem. During the inversion procedure, we keep the values of factor loadings constant to minimize CPU time, and only the factor scores are updated.

In the first step of finding the optimal values of the factor scores **f,** a random population of particles (250 particles in this study) with uniform distribution is generated within the search space previously given by solving *Equation (5)*. In this case, the boundaries of factor scores are found between –6 and 6. In *Equation (7)* both c_1 and c_2 are set as 2 in the whole iteration process. We set the inertia weight *w* in each iteration step according to Feng et al. [17]. They suggested the use of chaotic descending inertia weight, which is calculated in 3 steps: first a random number *z* is generated in the range between 0 to 1. Then by logistic mapping, *z* is set according to $z = 4z(1 - z)$ and finally

$$w = (w_1 - w_2)(q_{\max} - q)/q_{\max} + w_2 z\ , \tag{10}$$

where w_1 and w_2 are the initial and the final value of inertia weight respectively ($w_1 = 0.3$ and $w_2 = 0.08$). In *Equation (10)*, q_{max} and q are the maximal number of iteration steps and current iteration step respectively, in this case $q_{max} = 300{,}000$. Then in each iteration step, the positions of the particles are updated according to *Equations (6)–(7)*, and *Equation (9)* is recalculated with the new values of factors **f**. The particles are updated in each iteration step until a pre-defined number of iteration

steps is reached and then the final values of the factor scores are accepted as the solution. The factors calculated by the FA-PSO algorithm can be directly used to reveal hidden petrophysical information from the wireline logging data set. It was previously shown that for shorter intervals (max. 100–150 m), shale volume V_{sh} (given in percent) correlates linearly to the first factor log [11], [18]

$$V_{sh} = aF_1 + b, \tag{11}$$

where a is the slope of the regression line and b is the intercept. The first factor (F_1) is practically scaled into the range of 0 and 100.

FIELD EXAMPLE

The FA-PSO method is tested in a thermal water well (Well-1) in Baktalórántháza, north-east Hungary *(Figure 2)*. The well is 1,197 m deep and in the upper portion of it upper Pleistocene aquifers with varying grain sizes can be found. The mainly horizontal porous layers are bordered by shales. In the range of 100 to 160 m, mostly sandy layers are located, below it 10 to 15 m thick coarse-grained beds were deposited. The investigated interval is 93.1 m long, from 100 m to 193.1 m. As the input of factor analysis, we utilized the natural gamma-ray intensity (GR), density (GG), shallow resistivity (RS), spontaneous potential (SP) and neutron-porosity (NN) logs.

First, the factor loadings are calculated by Jöreskog's non-iterative approach using *Equation (4)*. *Table 1* contains the resultant factor loadings representing the correlation between the different well logs and extracted factors. By calculating three factors for this 93.1 m long section, which has 932 measured depth points, the vector of factor scores **f** is obtained with a dimension of 2,796 data points. This means that the algorithm of PSO has to find the global optimum by finding the optimal values of 2,796 variables along the borehole, i.e. factor scores.

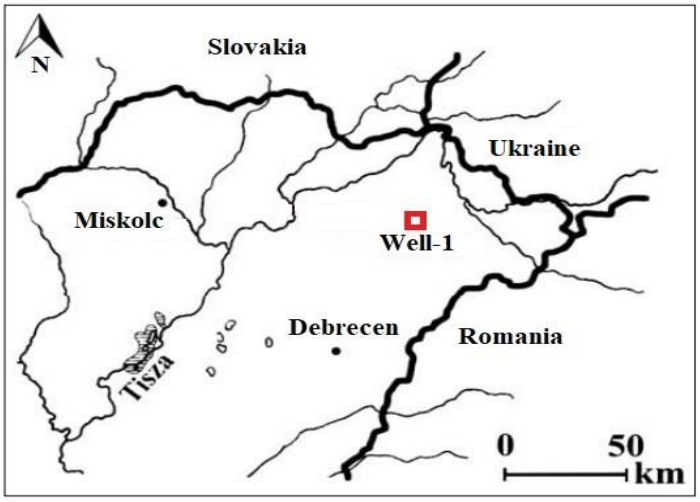

Figure 2. *Location of the water prospecting well used for testing the FA-PSO procedure*

Table 1

Rotated factor loadings estimated by the FA-PSO method in Well-1

Well logs	***Factor 1***	***Factor 2***	***Factor 3***
GR	0.7515	–0.1836	0.0127
SP	–0.0380	–0.7396	–0.0893
NN	0.0580	–0.1184	–0.5976
GG	–0.5930	–0.0948	0.3062
RS	–0.4955	0.6537	–0.0081

As *Table 1* shows, the natural gamma-ray log has the highest load and both the shallow resistivity and density logs have moderate loads on the first factor and the loads of the SP and neutron porosity logs are negligible. It is concluded that the first factor is mainly influenced by lithological properties of groundwater formations.

In the next step, the factor scores are estimated by the FA-PSO algorithm as detailed above. *Figure 3* shows the continuous decrease of the objective function values that is defined in *Equation (9)*. It reaches a minimum at about one hundred thousand iterations, which took approximately thirty minutes on a quad-core workstation. The steady decrease of the objective function indicates that the method is highly stable.

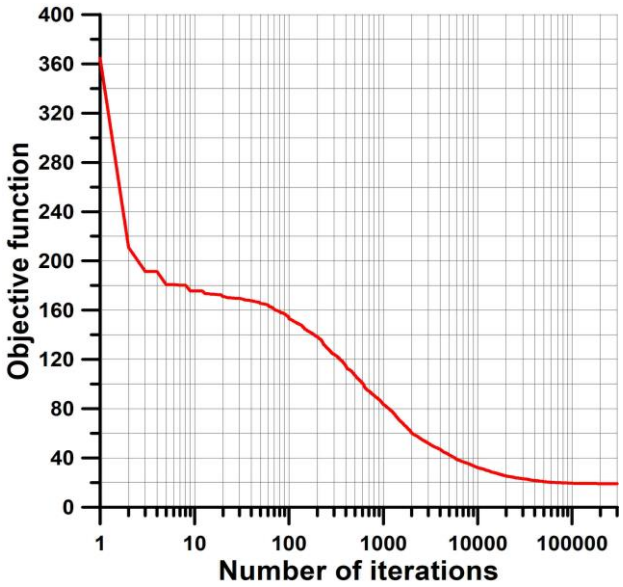

Figure 3. *Development of convergence of the FA-PSO procedure in Well-1*

Figure 4 presents the linear regression relation between the scaled first factor and the shale volume estimated by the FA-PSO method utilizing *Equation (11)*. In the given example, the regression coefficients with 95% confidence bounds are $a = 0.611$ [$a_{min} = 0.5863$, $a_{max} = 0.6353$] and $b = -1.299$ [$b_{min} = -2.435$, $b_{max} = -0.1632$].

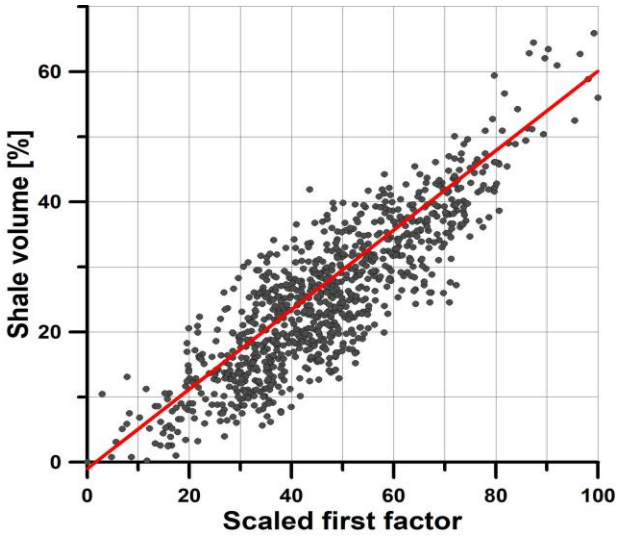

Figure 4. *Regression relation between the first factor and shale volume in Well-1*

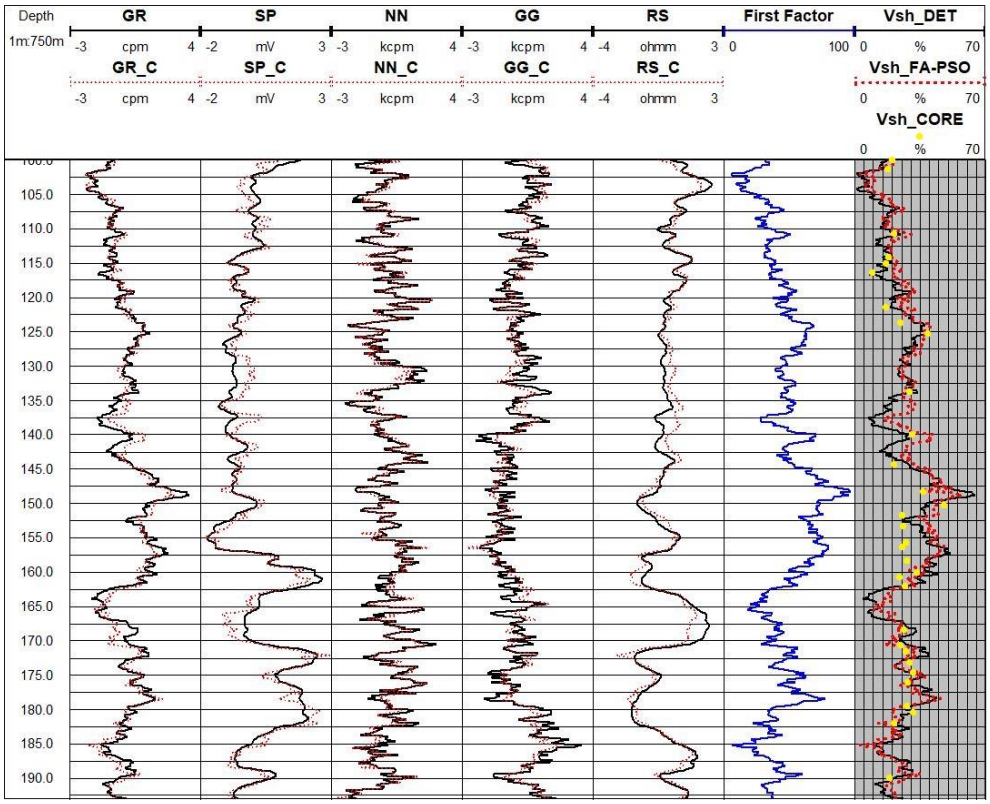

Figure 5*. The results of the FA-PSO procedure in Well-1*

The observed well logs and those calculated by the FA-PSO method are shown in *Figure 5*. On tracks 1 to 5, the standardized (input) well logs (black solid line) and the calculated logs (red dotted line) can be seen. Track 6 represents the extracted first factor log.

The fit between the measured and calculated data is quite good. The theoretical well logs drawn by red dotted lines are directly calculated as the multiplication of the rotated factor loadings and factor scores in *Equation (8)*. On track 7, the shale volume calculated from the first factor log (red dotted line) is compared to core data (yellow dots) and to that calculated by deterministic modeling suggested by Larionov [19] using the GR log (black solid line), where first the gamma ray index is calculated

$$I_{GR} = \frac{GR - GR_{MIN}}{GR_{MAX} - GR_{MIN}}, \tag{12}$$

where GR is the gamma ray reading of the formation, GR_{MIN} is the gamma ray reading in clean sand and GR_{MAX} is the reading in shale. Then shale volume is calculated as

$$V_{sh} = 0{,}083(2^{3{,}7 I_{GR}} - 1). \tag{13}$$

It can be seen that the shale volume calculated by the suggested statistical method also agrees well with the results of deterministic analysis and core data. These results indicate the applicability of the FA-PSO method for shale volume estimation in water bearing formations. The result of traditional factor analysis was earlier confirmed by core laboratory measurements in the same well [4].

CONCLUSIONS

This paper presents the first results of a newly developed well-log-analysis method. The Particle Swarm Optimization based factor analysis effectively transforms the observed wireline logging data into factor logs. It was found that the first factor log extracted by the FA-PSO method linearly correlates with the independently calculated shale volume of the investigated aquifer. The use of PSO in the frame of factor analysis allows also the estimation of the theoretical values of well logs, where the estimation neglects any preliminary knowledge of zone parameters or other petrophysical information. The method is very stable in the iteration process and provides reliable results within half an hour for a section of a hundred meters. Thus, the developed method can serve as an alternative tool for shale volume calculation in practical applications. The information obtained by the statistical method will be used in forthcoming studies to increase the overdetermination of inversion procedures. Namely, by fixing the factor analysis derived shale volume during the inversion procedure, an increase in accuracy and reliability of other model parameters can be achieved.

ACKNOWLEDGEMENTS

The research was carried out within the GINOP-2.3.2-15-2016-00031 *Innovative solutions for sustainable groundwater resource management* project of the Faculty of

Earth Science and Engineering of the University of Miskolc in the framework of the Széchenyi 2020 Plan, funded by the European Union, co-financed by the European Structural and Investment Funds.

REFERENCES

[1] Bücker, C., Shimeld, J., Hunze, S., Brückmann, W. (2000). 2. Data Report: Logging while drilling data analysis of Leg 171A, a multivariate statistical approach. *Proc. Ocean. Drill. Prog. Sci. Results., Scientific Results*, Vol. 171A.

[2] Hoseinpoor, M. K., Aryafar, A. (2014). The Use of Robust Factor Analysis of Compositional Geochemical Data for the Recognition of the Target Area in Khusf 1:100000 Sheet, South Khorasan, Iran. *International Journal of Mining & Geo-Engineering*, 48 (2), pp. 191–199.

[3] Szabó, N. P., Kormos, K. (2012). Édesvíztároló rétegek agyagtartalmának meghatározása fúrólyukszelvények faktoranalízise alapján. *Magyar Geofizika*, 53 (2), pp. 1–11.

[4] Szabó, N. P., Dobróka, M., Turai, E., Szűcs, P. (2014). Factor analysis of borehole logs for evaluating formation shaliness: a hydrogeophysical application for groundwater studies. *Hydrogeol. J.*, 22, pp. 511–526.

[5] Stocia, P., Jansson, M. (2009). On maximum likelihood estimation in factor analysis: an algebraic derivation. *Signal Processing*, Vol. 89 (6), pp. 1260–1262.

[6] Shaw, R., Srivastava, S. (2007). Particle swarm optimization: A new tool to invert geophysical data. *Geophys.*, 72 (2), pp. F75–F83.

[7] Yin, C. & Hodges, G. (2007). Simulated annealing for airborne EM inversion. *Geophys.*, 72 (4), pp. F189–F195.

[8] Marquardt, D. W. (1963). An algorithm for least-squares estimation of nonlinear parameters. *J. Soc. Indust. Appl. Math.*, 11 (2), pp. 431–441.

[9] Fernandez-Martinez, J. L., Fernández-Alvarez, J. P., García-Gonzalo, M. E., Menéndez Pérez, C. O. & Kuzma, H. A. (2008). Particle Swarm Optimization (PSO): a simple and powerful algorithm family for geophysical inversion. *SEG Technical Program Expanded Abstracts*, pp. 3568–3571.

[10] Grandis, H., Maulana, Y. (2017). Particle Swarm Optimization (PSO) for Magnetotelluric (MT) 1D Inversion Modeling. *IOP Conf. Ser.: Earth Environ. Sci.*, 62 012033.

[11] Szabó, N. P. (2011). Shale volume estimation based on the factor analysis of well-logging data. *Acta Geophys.*, 59, pp. 935–953.

[12] Jöreskog K G.: Factor analysis and its extensions. In: Cudeck R, MacCallum RC (eds) Factor analysis at 100: historical developments and future directions. Erlbaum, Mahwah, 2007, pp 47–77.

[13] Bartlett, M. S. (1937). The statistical conception of mental factors. *Br. J. Psychol.*, 28, pp. 97–104.

[14] Kennedy, J., Eberhart, R. C. (1995). Particle swarm optimization. *Proceedings of IEEE international conference on neural networks*, 4, pp. 1942–1948.

[15] Shi, Y. & Eberhart, R. A. (1998). modified particle swarm optimizer, Evolutionary Computation Proceedings. IEEE World Congress on Computational Intelligence. *The 1998 IEEE International Conference on*, pp. 69–73.

[16] Kaiser, H. F. (1958). The varimax criterion for analytical rotation in factor analysis. *Psychometrika*, 23, pp. 187–200.

[17] Feng, Y., Teng, G. F., Wang, A. X. & Yao, Y. M. (2007). Chaotic Inertia Weight in Particle Swarm Optimization. *In Innovative Computing, Information and Control.*

[18] Szabó, N. P., Dobróka, M. (2011). Geostatistical Approach for Shale Volume Estimation in Water-bearing Formations, Near Surface – *17th European Meeting of Environmental and Engineering Geophysics*, Leicester, UK, 12–14 September 2011.

[19] Larionov, V. V. (1969). Radiometry of boreholes. (In Russian), Moscow: Nedra.

Geosciences and Engineering, Vol. 6, No. 9 (2018), pp. 98–117.

A SYSTEMATIC DEPENDENCE OF ACOUSTIC VELOCITY ON INTERNAL PORE STRUCTURE IN SANDSTONE

MUHAMMAD NUR ALI AKBAR

MSc Petroleum Geoengineering – University of Miskolc
mn.aliakbar@gmail.com

Abstract: In spite of extensive research on relating acoustic velocity in porous rocks to the porosity and permeability of the rocks, there is still a lack of understanding on how those properties are significantly controlled by internal pore structure. It is in fact well known that rock permeability is determined not only by porosity but also by geometric details of the pore system. It is thus expected that acoustic velocity should be strongly influenced by the textural properties of rocks. The purpose of this study is to present results of a study on the relation of acoustic velocity to internal pore structure, porosity and permeability.

The approach used utilizes the Kozeny equation as presently it is the only one that accounts for almost all pore geometric details in determining rock permeability. Re-arrangement made on the Kozeny equation leads to rock grouping on the basis of pore structure similarity, similar to the value of Kozeny constant. This constant is the product of multiplying the pore shape factor F_s by tortuosity τ. The specific internal surface area S_b plays a role as a parametric variable for a given rock group. This method of rock grouping enables one to investigate the main influential factors that systematically control acoustic velocity in porous rocks.

This study employs laboratory core analysis datasets of P-wave velocity V_p, porosity ϕ, and permeability k measured on 67 sandstone samples available from several formations. Implementation of the rock grouping technique to the plugs results in several rock groups for each lithology. Each group has its own Kozeny constant. Based on the data available, the relations of V_p versus ϕ, k, $(k/\phi)^{0.5}$, or (k/ϕ^3) were constructed. The important finding is that each relation among the rock groups of each lithology is clearly separated. V_p tends to increase with an increase in Kozeny constant. However, for a given ϕ for all the groups, V_p increases remarkably with a decrease in Kozeny constant. These all mean that V_p increases with either an increase in the complexity of pore systems or, at the same pore complexity, a decrease in specific internal surface area.

Further analysis carried out on either the $V_p - (k/\phi)^{0.5}$ or the $V_p - (k/\phi^3)$ relation has resulted in a method for estimating matrix V_p. A reliable result is obtained for the sandstone samples. In conclusion, this work improves the knowledge about the effect of internal pore structure on V_p. The Kozeny constant systematically controls the relation of V_p to ϕ and k. The developed method and analysis can be implemented in an arbitrary well having sonic logging data to determine the matrix V_p at the reservoir conditions. For the surrounding wells with no sonic log data, it is possible to generate V_p versus depth once results of the well log analysis provide the k and ϕ values.

Keywords: *rock typing, compressional velocity, pore geometry, pore structure, matrix velocity, permeability*

INTRODUCTION

Studies examining the relationship between velocity and porosity has been conducted by many researchers and they showed that this relationship is not linear, while at first it was believed that this relationship was linear (Wyllie et al. 1956). It was demonstrated that the relationship between velocity and porosity is non-linear for porosity greater than 47%. This non-linear behavior is certainly expected from the presence of heterogeneity parameters such as clay content and distribution which in turn affect the size, shape and relationships or connectivity between the pore, uniformity of grain size and grain arrangement, and the different type of mineral compositions (Milad and Slatt 2018). For instance, an investigation by Han et al. (1986) explained that the velocity and porosity have a linear relationship and can be distinguished based on the volume of clay. Raymer et al. (1980) presented findings showing that the highest value of sonic velocity is at zero porosity, which means that the velocity measured is mineral velocity, commonly known as matrix velocity. In contrast, the velocity will be minimum when the volume of solid material decreases and volume of pore space is high. However, this complex architecture of porous rock requires extensive research for better understanding on how the acoustic wave propagates through this medium and how the pore geometric details show the correlation not only between velocity and porosity, but also velocity and permeability.

Other investigators have conducted similar studies but in more detail about the effect of velocity on the petrophysical characteristics of pore systems. For instance, Prasad (2003) presented the relationship between velocity and permeability with rock grouping method based on hydraulic flow units which represent similarity in pore geometry. Depositional texture also controls the petrophysical properties and wave velocity behaviors of the rock (Fabricius et al. 2007, 2010; Mokhtar et al. 2010). Other extensive studies by Weger and Eberli (2009), Xu and Payne (2009), Verwer et al. (2010), Milad et al. (2018), Rahman and Pierson (2011) and Bashah and Pierson (2012) demonstrated that the main factor in P-wave velocity behavior is the complexity of pores. They quantified and investigated the relationship between wave velocity and the pore geometry by pore-type variations and parameters of pore space that are expressed by dominant pore size, roundness (γ), aspect ratio (AR), and pore network complexity or perimeter over area (POA) obtained from petrographic analysis.

Research into the relationship between pore geometry and pore structure (Wibowo and Permadi 2013) derived from parameters of porosity and permeability led to the rock grouping method of the PGS (Pore Geometry-Structure) plot. Prakoso et al. (2016) based an explanation of the relationship between P-wave velocity with pore geometry and pore structure on the basis of PGS method. This study explains that rock samples with similar pore geometry and pore structure have their own group, referred to as rock type, and have different relationships between velocity and porosity. However, datasets of their study were acquired by using dry core samples in ambient condition, which did not represent the real reservoir circumstances in the subsurface.

This paper presents the effects of P-wave velocity on the basis of pore geometry and pore structure rock types (i.e. PGS) using core samples under pressurized and

saturated conditions. Furthermore, these relationships can be used to estimate P-wave matrix velocity and to generate P-wave velocity versus depth once results of the well log analysis provide the necessary permeability and porosity values.

METHODS AND DATA

Rock typing – PGS

Pore geometry-structure (PGS) was proposed by Permadi and Susilo (2009) and then updated with simpler rock type determination using a PGS rock type curve by Wibowo and Permadi (2013). Pore geometry here is simply an equivalent to mean hydraulic radius (Harmsen 1955) and pore structure is a pore attribute that is influenced by pore shape, pore tortuosity, and internal surface area, which all make up the architecture of the pore system. The idea for this method was adopted from the study of El-Khatib (1995) explaining that rock samples which have a similar capillary pressure curve should have similar pore size distributions, meaning similar pore geometry and pore structure. Thus, it will have the same value of tortuosity and irreducible water saturation. The similarity in pore architecture is manifested by the similarity in the pore shape factor and tortuosity. The product of these two pore attributes is well known as the Kozeny constant (Kozeny 1927). The only difference among the rock samples having a similar Kozeny constant is the pore size in terms of the mean hydraulic radius. Following is the Kozeny equation re-written in two forms:

$$\left(\frac{k}{\phi}\right)^{0.5} = \phi\left(\frac{1}{(\tau F_s {S_b}^2)}\right)^{0.5}, \tag{1}$$

and

$$\frac{k}{\phi^3} = \frac{1}{\tau F_s {S_b}^2}, \tag{2}$$

where k is permeability and ϕ is porosity. The term $(k/\phi)^{0.5}$ is a pore geometry term, frequently called the "mean hydraulic radius", and (k/ϕ^3) is simply called the "pore structure term" that accounts for all features of the internal structure [see *Equation (2)*]. The other parameters τ, F_S, and S_b are tortuosity, pore shape factor, and specific internal surface area, respectively.

Replacing the variable $1/\tau F_s {S_b}^2$ in *Equation (1)* with (k/ϕ^3), it can be written as follows:

$$\left(\frac{k}{\phi}\right)^{0.5} = \phi'\left(\frac{k}{\phi^3}\right)^{0.5} \tag{3}$$

or

$$\left(\frac{k}{\phi}\right)^{0.5} = \left(\frac{v_p}{v_b}\right)\left(\frac{k}{\phi^3}\right)^{0.5} \tag{4}$$

Wibowo and Permadi (2013) demonstrated that these two equations say that plotting $(k/\phi)^{0.5}$ against (k/ϕ^3) on log-log plot graph yields a straight line with a slope 0.5 when the straight line produces $v_p/v_b = \phi = 1$, where v_p and v_b are volume pore and bulk volume, respectively. The equations above are valid only for a single capillary tube

with infinitely small wall thickness. This implies that fluid flows at constant rate for the entire flow path, i.e. volumetric flow efficiency *(E_P)* is 100%. However, in porous rocks that have many tiny crevices, non-uniform pore sizes, rough pore walls, and probably dead ends or blind pores as well, the flow would be dominated by connected large pores (Wyllie and Gardner 1958) and influenced by the Knudsen effect (Kraus et al. 1953) in smaller pores, and probably even stagnant in the dead ends, resulting in $E_P < 100\%$. Therefore, *Equation 3* can be written in the form of a power law equation as follows:

$$\left(\frac{k}{\phi}\right)^{0.5} = \left(\frac{v_p}{v_b}\right)\left(\frac{k}{\phi^3}\right)^{0.5} \tag{5}$$

where a, which was ϕ' in Equation (3) above, is a constant that is interpreted as a correction factor for volumetric fluid flow efficiency for irregular pore systems (Permadi and Wibowo 2013) and b is the power law exponent, an indicator of the complexity of pore structure. The maximum value of b is 0.5 for smooth capillaric systems as described above. For natural porous rocks having similar microscopic geological features, it was shown that the value of b is less than 0.5. The lower the b value, the more complex the pore structure.

In this paper, first this rock typing method is applied to the core analysis data and then the grouping result of each relation can be extended to seismic parameters to create a strong correlation between velocity and permeability, velocity and pore geometry, and also velocity and pore structure. Finally, the rock type units are used to model velocity equations and generate the matrix velocity estimation.

DATA USED

The laboratory data for sandstone were compiled by Prasad (2003) and are given in the Appendix. There are 67 core samples and the data provide the measurements of velocity and attenuation at similar pressure around 40 MPa and saturated by distilled water, along with values for porosity and permeability. All velocity and quality factor values used here were measured in the ultrasonic frequency range (between 0.5 to 1 MHz) on fully saturated rocks under varying pressures using the pulse transmission technique (Prasad 1998). A summary of the used data in this study is presented in *Table 1*. In general, the wide ranges of porosity and permeability are beneficial for investigating the effects of rock quality and compressional velocity behaviors.

Table 1

Summary of laboratory measurement of core samples

PARAMETERS	**Min.**	**Max.**	**Avg.**
Porosity, ϕ – (%)	3.41	36.04	19.48
Permeability, k – (mD)	0.005	2040	9.284
Volume of clay, V_{cl} – (%)	0.00	30.00	11.30
P-wave velocity, Vp – (m/s)	2,909.0	5,171.0	3,997.4

RESULTS AND DISCUSSION

The relationship among porosity, permeability, and P-wave velocity

All of the core data analysis parameters such as porosity, permeability, and P-wave velocity are cross-plotted in *Figure 1*. In general, the correlation between permeability and porosity is not really good. Moreover, the relationship between velocity and permeability is also very scattered. Only P-wave velocity and porosity have a good linear correlation in this case.

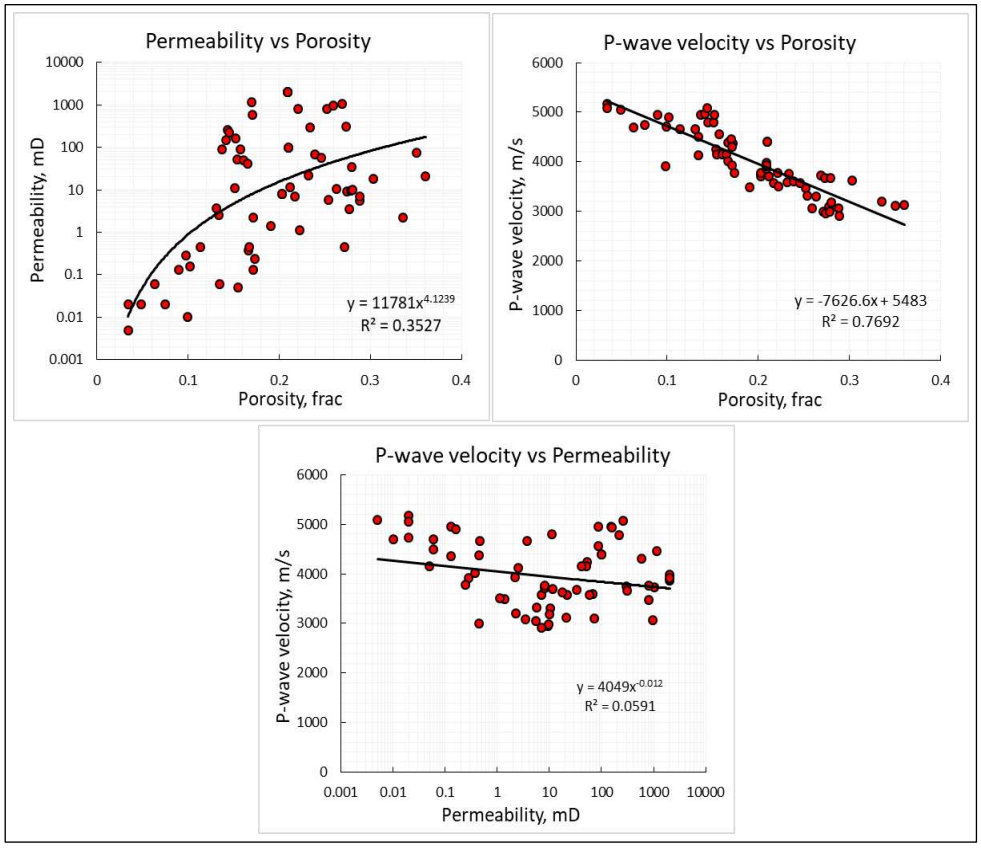

Figure 1. *Relationship among Permeability and Porosity, P-wave velocity and porosity, and P-wave velocity and Permeability*

This result is important when investigating how the heterogeneity of the sandstone samples affects the relationship between velocity and permeability and being a background to understand the effects of pore architecture details to compressional sonic velocity.

Rock Grouping Based on PGS Rock Type Curve

The relationship between P-wave velocity with both pore geometry and pore structure was obtained by grouping the rocks according to the PGS rock type curve (Wibowo and Permadi 2013). *Figure 2* shows the result of the grouping of the data, where the data falling on the same line were interpreted as having the same rock type number. This same rock type means that the samples show similarity in their pore architecture, including the rock texture, such as grain size, grain sorting, grain angularity and roundness, type of cements distribution, and other quality of the porous rock properties. As can be seen in this figure, all the data points cover nine rock type lines (RT4 to RT13). In general, it should be noted that the larger the rock type number, the lower the slope of the line and the more complex the pore structure, resulting in poorer reservoir quality (low porosity, low permeability) of the rock type.

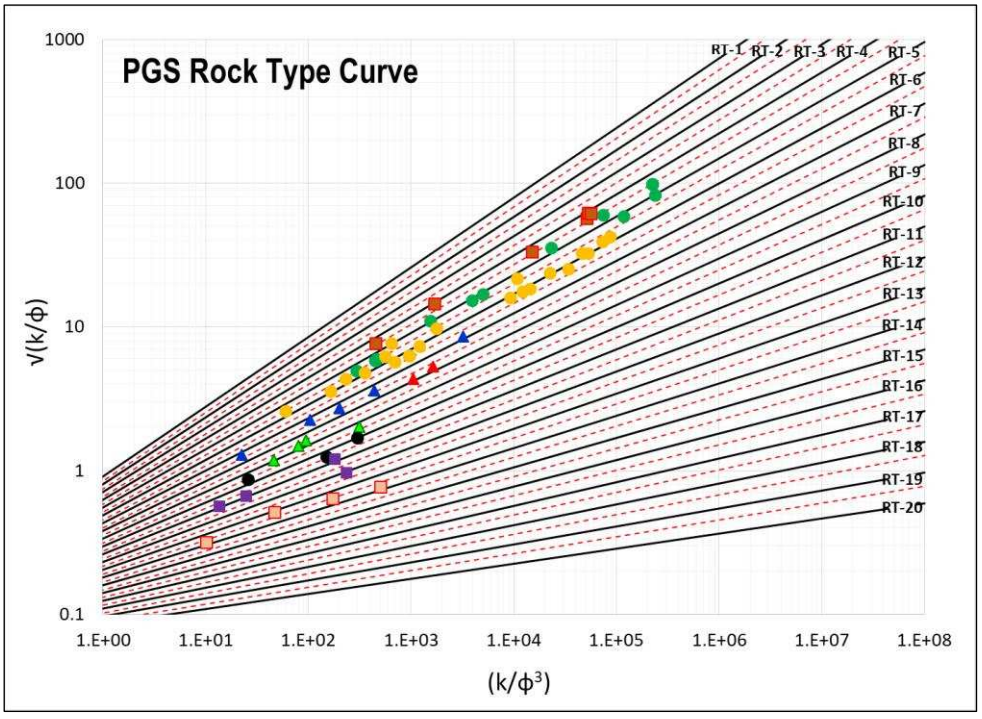

Figure 2. *Identification of the rock type based on pore geometry and pore structure*

After grouping all the rock samples, each rock type was propagated to the new relationship between P-wave velocity and permeability. For instance, *Figure 3* represents strong correlation (as opposed to the scattered nature shown in *Figure 1*). All the rock type lines are collected in the same point at which both pore geometry and pore structure meet, hereafter called the rock type convergence point. The physical meaning of this point was demonstrated by Wibowo (2014) as the

indistinguishable point where we cannot distinguish the rock type number. He determined the convergence point at $(k/\phi)^{0.5} = 0.045$ and $k/\phi^3 = 0.002$. This means that porous rocks at this point of convergence have the same property, possibly including the P-wave velocity, V_p. Since no distinction in both pore geometry and structure could be made among all rock types at the convergence point, it is assumed for practical purposes that this situation holds for infinitely small capillary tubes at the porosity value of 1.0, yielding V_p of the fluid filling the pores. Thus, the theoretical P-wave velocity at this point is the velocity of the saturated fluid (i.e. distilled water), which is assumed to be 1500 m/s. Consequently, the correlations of V_p against either $(k/\phi)^{0.5}$ or k/ϕ^3 developed in the present study have a convergence point at a point $(V_p, (k/\phi)^{0.5}) = (1500, 0.045)$ or $(V_p, k/\phi^3) = (1500, 0.002)$.

From *Figure 3* it can be seen that P-wave velocity and Permeability display a special correlation when grouped based on the PGS method. This phenomenon becomes the basis of further analysis and is discussed in more detail in the section on the effects of pore geometry and pore structure on P-wave velocity.

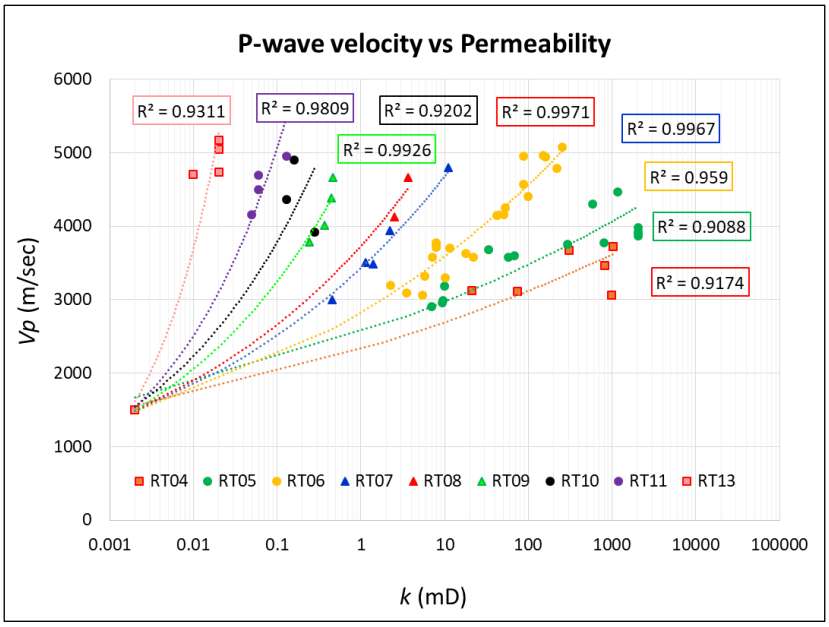

Figure 3. *Plot P-wave velocity versus permeability for each rock type*

The Effect of Pore Geometry on P-Wave Velocity (V_p)

In general, *Figure 4* follows the trend characterized in *Figure 3*. The plot V_p versus pore geometry shows all the data points were separated to form clusters, each specifically representing a certain rock type. Without grouping the rock samples into rock types, the spread of the data points is quite large, although there is a trend of

increasing V_p as the pore geometry term decreases. This is mainly due to combined effects of porosity, grain sizes and shapes, and rock hardness.

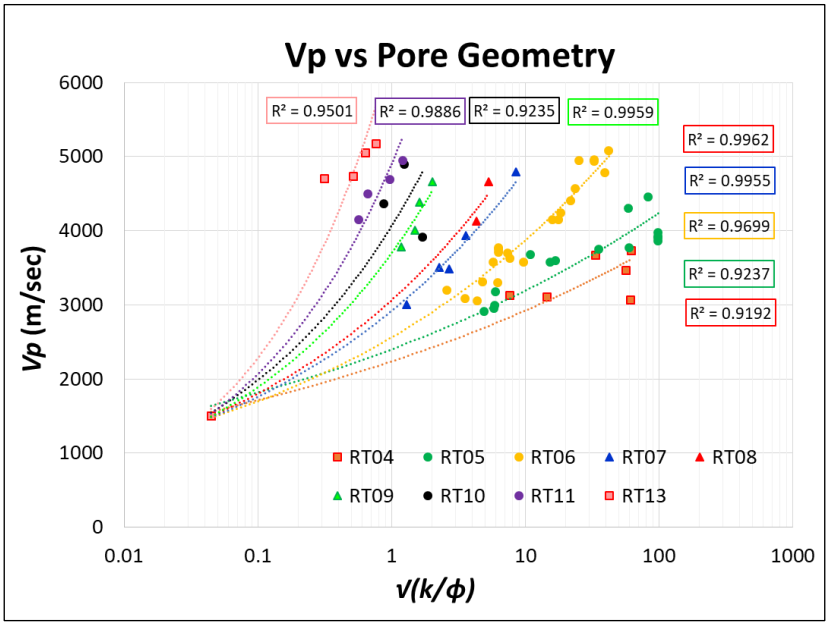

Figure 4. *The relationship among P-wave velocity and Pore Geometry*

It is more interesting to analyze the relationship between V_p and pore geometry on the rock type basis. *Figure 4* demonstrates that all rock types have the same behavior, that is V_p tends to become higher as pore geometry variable increases. As pore geometry here is equivalent to the mean hydraulic radius, V_p increases with this radius. Starting with the poorest rock quality, the data points furthest to the left of several rock types seemly have the same trend line *(*see *Figure 4)*. This behavior is not only due to both very low porosity and very low permeability but also the fact that both rock textures and the level of rock hardness are about the same. This level is determined by type and content or volume of the clay material (as a cement). The higher the density of the material and the larger the clay content, the harder the rock is. Therefore, the difference that makes higher velocity V_p for the higher rock types is most likely a higher percentage of the clay content.

For rock types of better quality, those with smaller rock type numbers, the data points of neighboring rock types are clearly separated. The cementing materials in these rock types are relatively low in quantity. The better the rock type quality, the less the amount of clay content and the stronger the role of pore geometry. As has been discussed above, pore geometry in each rock type is strongly controlled by the value of S_b. According to Equation 1, the pore geometry variable is inversely proportional to S_b squared. Porous rocks made up of smaller grains size tend to have higher S_b, while larger grain size produces lower S_b.

Table 2
The equations of each rock type for the plot of P-wave velocity versus pore geometry

Vp vs. Pore Geometry [$(k/\phi)^{0.5}$]				
RT	Equation	*c*	*p*	R^2
4	$Vp = 2236.4\ \sqrt{(k/\phi)}^{0.1161}$	2236.4	0.1161	0.9192
5	$Vp = 2399.6\ \sqrt{(k/\phi)}^{0.1236}$	2399.6	0.1236	0.9237
6	$Vp = 2562.3\ \sqrt{(k/\phi)}^{0.1792}$	2562.3	0.1792	0.9699
7	$Vp = 2916.8\ \sqrt{(k/\phi)}^{0.2185}$	2916.8	0.2185	0.9955
8	$Vp = 3062.4\ \sqrt{(k/\phi)}^{0.2302}$	3062.4	0.2302	0.9962
9	$Vp = 3698.6\ \sqrt{(k/\phi)}^{0.292}$	3698.6	0.292	0.9959
10	$Vp = 4063.6\ \sqrt{(k/\phi)}^{0.3109}$	4063.6	0.3109	0.9235
11	$Vp = 4899.1\ \sqrt{(k/\phi)}^{0.3744}$	4899.1	0.3744	0.9886
13	$Vp = 6421.8\ \sqrt{(k/\phi)}^{0.4487}$	6421.8	0.4487	0.9501

It has been described above that any given rock type has its own similarity in both tortuosity and pore shape factor (i.e. the Kozeny constant). Thus, the only difference among the members of a rock type is S_b. According to *Equation 1*, a lower S_b will result in a higher $(k/\phi)^{0.5}$. A lower S_b can result from a smaller number of pores or a decrease in porosity but relatively bigger pore size. Thus, porosity reduction that results in an increase in $(k/\phi)^{0.5}$ is an indication of a larger mean hydraulic pore size or a bigger average pore throat size. It may be concluded that, for a given rock type, the increase in V_p with pore geometry is due to a decrease in porosity followed by an increase in the average pore throat size. However, for general trend for all rock types members without grouping *(*see *Figure 7)*, Vp decreases as $(k/\phi)^{0.5}$ increases, the influence of porosity may be much stronger than that of the mean hydraulic pore size or pore throat size. *Table 2* shows a result of the grouped P-wave velocity versus pore geometry.

The Effect of Pore Structure on P-Wave Velocity

According to *Equations 1* and *2*, parameters that affect either pore geometry or pore structure variable are principally the same. *Equation (2)* states that porous rocks with lesser tortuosity, simpler pore shapes or a lower shape factor, and a lower specific internal surface area would have a higher value of the pore structure term. These characteristics are normally possessed by good to excellent quality rock types. Conversely, lower quality rock types are those with higher tortuosity and more complex pore shapes or a higher shape factor, resulting in a lower value of the pore structure term and more complex pore structure. The pore structure variable is much higher in value than that of pore geometry, as the pore structure variable is inversely

proportional to porosity to the power of three. A very low porosity combined with a relatively high permeability would yield a high value for the pore structure variable. *Figure 5* demonstrates the relation of pore structure variable to V_p for sandstones. It looks much the same as the relationship between pore geometry variable and V_p *(*see *Figure 4)*. However, as depicted in *Figure 5*, the separation of the data points of several lower quality rock types is less clear due to overlapping when compared with that seen in *Figure 4* for the effect of pore geometry on V_p. This is because the numerical values of pore structure variable among the very low-quality rock types are nearly the same (Prakoso et al. 2016).

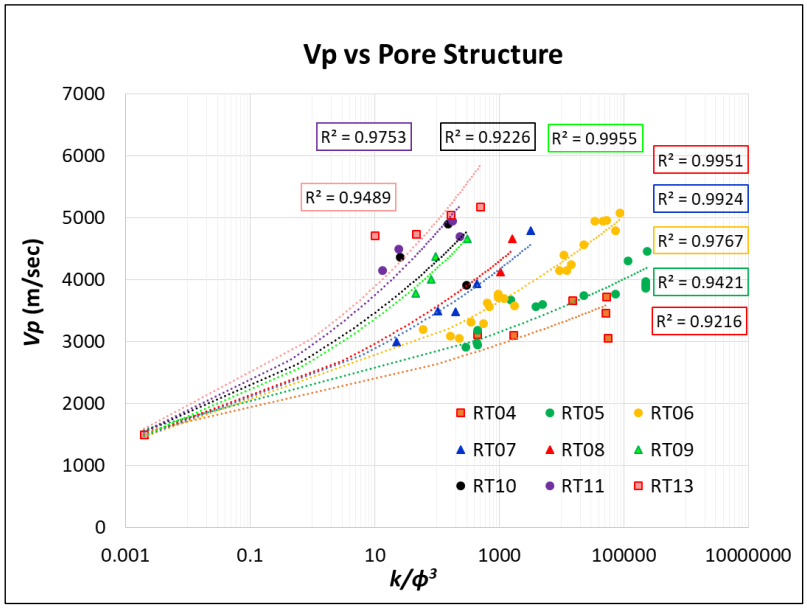

Figure 5. *The relationship among P-wave velocity and pore structure*

As can be seen in *Figure 5*, some data points of several rock types behave differently in that V_p decreases or is relatively constant as (k/ϕ^3) increases. It would be expected that V_p increases with permeability as shown by Klimentos (1991). This is true in the cases here for any given rock type as long as the increase in permeability is followed by relatively more porosity reduction. The concept of rock typing as given by *Equation (5)* assumes the same tortuosity and pore shape for all the members of a rock type. Consequently, to the group, k/ϕ^3 is strongly influenced by specific internal surface area S_b. By ignoring the effect of materials composing the samples, the effect of the permeability increase on the velocity was probably suppressed by the influence of both the higher porosity and S_b because the increase in these two parameters reduces the velocity. The equations established through the relationship between V_p and pore structure are presented in *Table 3*.

Table 3
The equations of each rock type for the plot of P-wave velocity versus pore structure

Vp vs Pore Structure (k/ϕ^3)				
RT	**Equation**	***d***	***q***	***R²***
4	$Vp = 2109.8\ (k/\phi^3)^{0.0489}$	2109.8	0.0489	0.9216
5	$Vp = 2197.0\ (k/\phi^3)^{0.0523}$	2197.0	0.0523	0.9421
6	$Vp = 2257.6\ (k/\phi^3)^{0.0695}$	2257.6	0.0695	0.9767
7	$Vp = 2411.3\ (k/\phi^3)^{0.0792}$	2411.3	0.0792	0.9924
8	$Vp = 2467.7\ (k/\phi^3)^{0.0803}$	2467.7	0.0803	0.9951
9	$Vp = 2703.5\ (k/\phi^3)^{0.0951}$	2703.5	0.0951	0.9955
10	$Vp = 2788.9\ (k/\phi^3)^{0.0943}$	2788.9	0.0943	0.9226
11	$Vp = 2954.5\ (k/\phi^3)^{0.1036}$	2954.5	0.1036	0.9753
13	$Vp = 3058.0\ (k/\phi^3)^{0.1045}$	3058.0	0.1045	0.9489

Based on *Tables 2* and *3*, these results enable generalization of the relationship for V_p versus $(k/\phi)^{0.5}$ and V_p versus k/ϕ^3, respectively, in the forms of *Equation (6)* and *(7)* below.

$$V_p = c \times [(k/\phi)^{0.5}]^p \tag{6}$$

$$V_p = d \times [(k/\phi^3)]^q, \tag{7}$$

where c and d are constants and p and q are exponents, which are all rock type dependent.

P-Wave Velocity Prediction

The application of the regression formula of each rock type as shown in *Tables 2* and *3* for predicting V_p was performed. By using permeability and porosity values of the samples of the corresponding rock type, the predicted V_p was then compared with the values of V_p measured. The comparisons are exhibited in the Figure 6 for both V_p against $(k/\phi)^{0.5}$ and V_p against (k/ϕ^3), giving the average relative errors $ARE = 5.23\%$ and 8.64%, respectively.

The relationships of V_p against $(k/\phi)^{0.5}$ and V_p against (k/ϕ^3) are demonstrated in *Figure 7* without the use of rock grouping. The figure also depicts both the equations and the correlation coefficients R^2 of the trend lines. If we apply these results for predicting the *Vp,* the average relative errors will be considerably higher than those resulting from rock grouping in *Figure 6*.

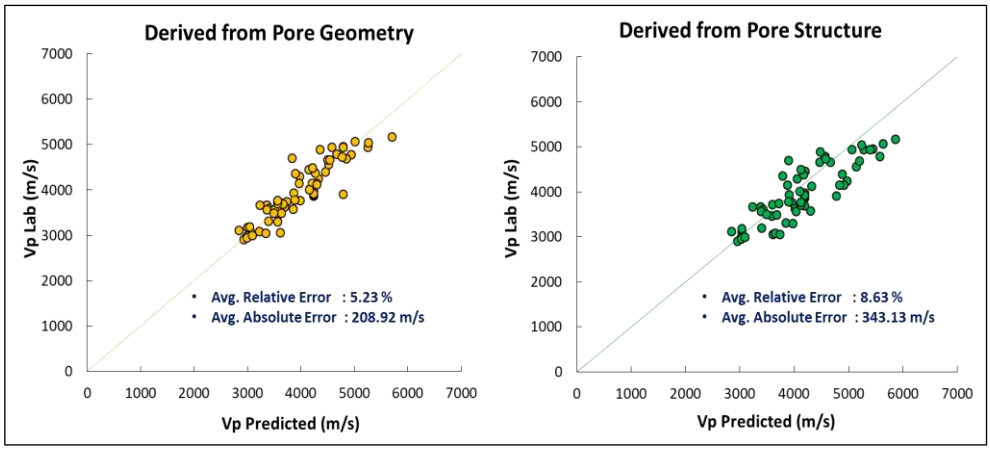

Figure 6. *Predicted versus measured V_p based on $(k/\phi)^{0.5}$ and (k/ϕ^3) for rock typed samples*

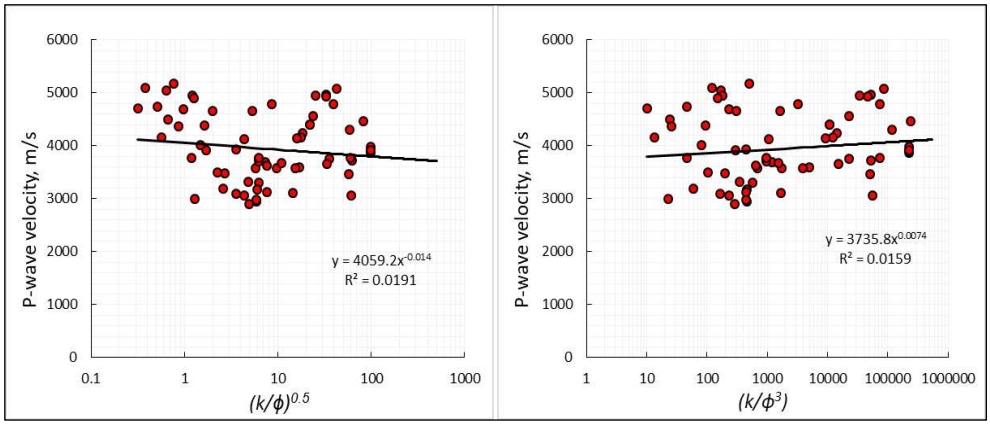

Figure 7. *Trend lines on ungrouped rocks for V_p against $(k/\phi)^{0.5}$ and V_p against (k/ϕ^3)*

Matrix Velocity Estimation

The application of relationship between V_p and pore geometry $(k/\phi)^{0.5}$ was derived to determine matrix velocity value. This matrix P-wave velocity is mainly used for estimating the primary porosity from the sonic log. For instance, the well-known Wyllie equation was used to apply this method to estimate porosity:

$$\phi_S = \frac{\Delta t - \Delta t_{ma}}{\Delta t_f - \Delta t_{ma}} \tag{8}$$

where Δt is a transit travel time of measured sonic log data, while Δt_{ma} and Δt_f are transit travel times of matrix and saturated fluid, respectively, in the formation logged with the sonic tool.

In many cases, the investigators used the Δt_{ma} mainly from the literature as shown in *Table 4*. However, the matrix velocity is strongly influenced by its rock compositions and it will be difficult to determine if no rock composition data are available. This is worth investigating because if the matrix velocity does not represent the correct condition of the reservoir, the porosity estimation will be either overestimated or underestimated.

Table 4

Velocity matrix and transit travel time of sonic log

Rocks/Materials	V_{ma} (m/sec)	Δt_{ma} (µs/m)	Δt_{ma} (µs/m) (commonly used)
Sandstones	5486.4 - 5943.6	182.3 - 168.2	182.3 - 168.2
Limestones	6400.8 - 7010.4	156.2 - 142.6	155.8
Dolomites	7010.4	142.6	142.6
Anhydrate	6096	164.0	164.0
Salt	4572	218.7	219.8
Casing (Iron)	5334	187.5	187.5
Rocks/Materials	**V_{ma} (ft/sec)**	**Δt_{ma} (µs/ft)**	**Δt_{ma} (µs/ft) (commonly used)**
Sandstones	18000 -19500	55.5 - 51.0	55.5 - 51.0
Limestones	21000 - 23000	47.6 - 43.5	47.5
Dolomites	23000	43.5	43.5
Anhydrate	20000	50.0	50.0
Salt	15000	66.7	67.0
Casing (Iron)	17500	57.0	57.0

*Schlumberger, 1989, *Log Interpretation Principles/ Applications*

In order to solve this problem, by utilizing the equations in *Table 2*, constants *c* and exponents *p* from all rock types were plotted against each other. Then, linear regression was made from these points and the regression line was extended forward until the exponent $p = 1$. At this point, the condition of the rock is assumed to be very tight or without pores remaining. Therefore, this condition is expected as the grain matrix and then the constant *c* is pointed to the value 9289.8 m/s *(*see *Figure 8)*. This value should be normalized because the data used in this study were measured in laboratory at 40 MPa. This is important because velocities almost always increase with effective pressure.

The velocity change between any two effective pressures P1 and P2 can be conveniently written as:

$$\frac{Vp\ @\ P2}{Vp\ @\ P1} = \frac{1.0-0.38\exp(-P2/12)}{1.0-0.38\,exp(-P1/12)} \tag{9}$$

where P2 is the pressure in the ambient condition and P1 is the effective pressure used during the core measurement.

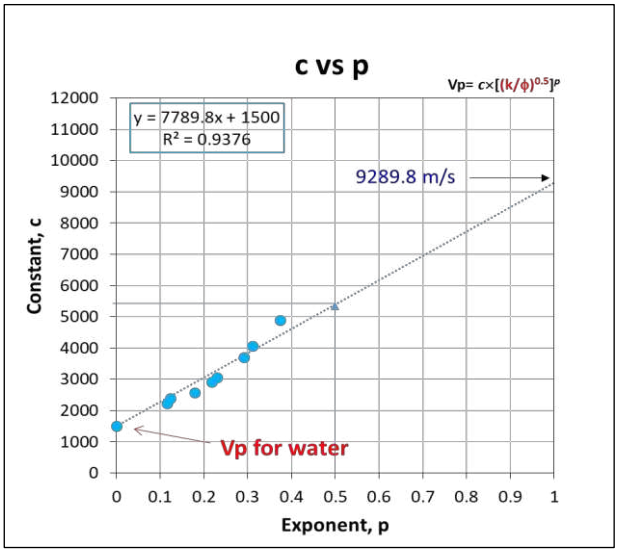

Figure 8. *Crossplot Constant (c) versus exponent (p) for prediction matrix velocity*

According to *Equation (9)*, estimated matrix velocity obtained through this method is 5,868.93 m/s (19,255.02 ft/s), which leads us to sonic travel time around 51.93 µs/ft. That value was applied into the Wyllie porosity equation and compared to the commonly used Δt_{ma} which is 55.5 and 51 µs/ft. The comparisons for predicted versus measured porosity are exhibited in *Figure 9*.

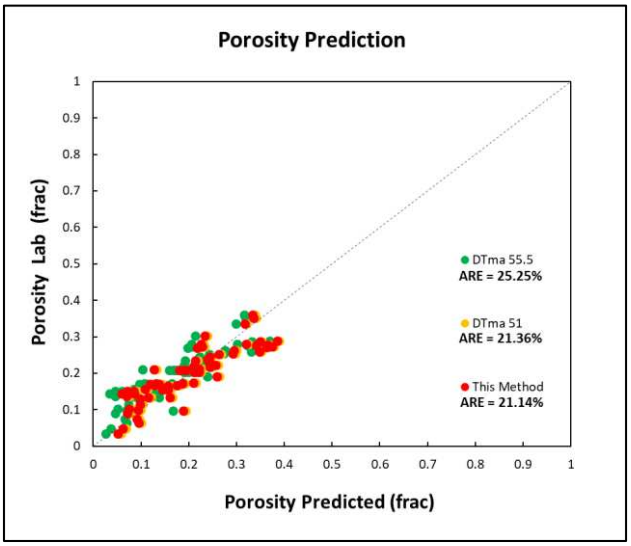

Figure 9. *The result of predicted versus measured porosity from different* DT_{ma} values

CONCLUSION

The effect of pore attributes, pore geometry and pore structure on P-wave velocity at pressurized and saturated conditions has been investigated for sandstones. These samples represent ideal systems where *P*-wave velocity values are systematically controlled by similarity of internal pore structure, which is similarity in both tortuosity and the pore shape factor. In the given rock type, either pore geometry or pore structure increases owing to a decrease in specific internal surface area and porosity with increasing mean hydraulic radius, which all give rise to an increase in saturated P-wave velocity.

The best obtained prediction of P-wave velocity was made by the relationship between V_p and pore geometry $(k/\phi)^{0.5}$, giving a relative error of 5.23%. Then, estimation of sonic logs can be generated once the well log analysis provides the corresponding permeability and porosity values. Furthermore, matrix velocity can be also derived from the relation between constant c and exponent p of $V_p = c \times [(k/\phi)^{0.5}]^p$ obtained from each of the established rock types. The results of estimated porosity by using matrix velocity in this method show better prediction compared to the assumed matrix velocities from literature. In addition, if we do not have rock/mineral composition information, we can use an apparent matrix value obtained with the procedure presented here.

ACKNOWLEDGMENT

The describe darticle was carried out as part of the EFOP-3.6.1-16- 2016-00011 *Younger and Renewing University – Innovative Knowledge City – institutional development of the University of Miskolc aimingat intelligent specialization* project implementedin the frame work of the Szechenyi 2020 program. The realization of this project is supported by the European Union, co-financed by the European Social Fund.

It is also supported by the Demonstratorship program at the Geophysical Department, University of Miskolc under dr. Norbert Péter Szabó supervision. Muhammad also would like to thank professor Pudji Permadi (Bandung Institute of Technology) for advice and discussions.

REFERENCES

[1] El-Khatib N. (1995). Development of a modifed capillary pressure-J function. Society of Petroleum Engineers. *Presented at the SPE Middle East Oil Show held in Bahrain*: March 11–14. doi:10.2118/29890-MS.

[2] Fabricius, I. L., Baechle, G., Eberli, G. P. & Weger, R. (2007). Estimating Permeability of Carbonate Rocks from Porosity and Vp/Vs. *Geophysics*, 72, 5. http://dx.doi.org/10.1190/1.2756081.

[3] Fabricius, I. L., Baechle, G., Eberli, G. P. & Weger, R. (2010). Elastic Moduli of Dry and Water-Saturated Carbonates – Effect of Depositional Texture, Porosity, and Permeability. *Geophysics*, 75, 3. http://dx.doi.org/10.1190/1.3374690

[4] Han, D. H., Nur, A. & Morgan, D. (1986). Effects of Porosity and Clay Content on Wave Velocities in Sandstones. *Geophysics*, 51, pp. 2093–2107. http://dx.doi.org/ 10.1190/1.1442062

[5] Harmsen, G. J. (1955). The Concept "Hydraulic Radius" in Porous Media. Petroleum Transactions. *AIME,* 204, pp. 274–277.

[6] Klimentos, T. (1991). The effects of porosity-permeability-clay content on the velocity of compressional waves. *Geophysics*, 56 (12), pp. 1930–1939. https://doi.org/10.1190/ 1.1443004

[7] Kozeny, J. (1927). Uber kapillare Leitung des Wassers im Boden (Aufstieg Versikerung und Anwendung auf die Bemasserung), *Sitzungsber Akad, Wiss, Wein, Math.-Naturwiss*, KL 136(Ila), pp. 271–306.

[8] Mavko, G., Mukerji, T., Dvorkin, J. (2009). *The Rock Physics handbook*. 2nd edn. Cambridge: Cambridge University.

[9] Milad, B., Ghosh, S. & Slatt, R. M. (2018). Comparison of rock and natural fracture attributes in karsted and non-karsted Hunton Group Limestone: Ada and Fittstown area, Oklahoma. *Shale Shaker*, 69, No. 2, pp. 70–86.

[10] Milad, B. & Slatt, R. (2018). Impact of Lithofacies Variations and Structural Changes on Natural Fracture Distributions. *AAPG and SEG Interpretation: a journal of subsurface characterization*, Vol. 6 (4), p.1, doi: 10.1190/int-2017-0138.1.

[11] Mokhtar, E. A., Vega, S., Hassan, A. A., & Baloushi, M. N. M. A. (2010). Rock Physics Characterization Using Acoustic Velocity Measurements on Late Cretaceous Carbonate Rocks from the Middle East. *Society of Petroleum Engineers*, 138649.

[12] Prakoso, S., Permadi, P., Winardhie, S. (2016). Effects of pore geometry and pore structure on dry P-wave velocity. *Modern Appl Sci*., 10 (8), pp. 117–133. https://doi.org/10.5539/mas.v10n8p117.

[13] Prasad, M. (1998). Empirical trends in velocity and quality factor properties of reservoir rocks: 68th Ann. Internat. Mtg., Soc. Expl. Geophys. *Expanded Abstracts*, pp. 992–995.

[14] Prasad, M. (2003). Velocity-permeability relations within hydraulic units. *Geophysics*, 68, pp. 108–117, https://doi.org/10.1190/1.1543198

[15] Verwer, K., Eberli, G., Baechle, G. & Weger, R. (2010). Effect of Carbonate Pore Structure on Dynamic Shear Moduli. *Geophysics,* 75, 1. http://dx.doi.org/10.1190/1.3280225.

[16] Rojas, E., Davis, T. L., Batzle, M., Prasad, M. & Michelena, R. J. (2005). Vp-Vs Ratio Sensitivity to Pressure, Fluid, And Lithology Changes in Tight Gas Sandstones. *SEG Technical Program Expanded Abstracts*, 24 (1), doi: 10.1190/1.2147950.

[17] Raymer, L. L., Hunt, E. R., Gardner, J. S. (1980). An improved sonic transit time-to-porosity. *SPWLA 21st Annual Logging Symposium*, 8–11 July, Lafayette, Louisiana.

[18] Weger, R. J., Eberli, G. P. (2009). Quantification of pore structure and its effect on sonic velocity and permeability on carbonate. *AAPG Bull*, 93 (10), pp. 1297–1317, https://doi.org/10.1306/05270909001

[19] Wibowo, A. S. (2014). *Karakterisasi Batuan Karbonat Berdasarkan Geometri dan Struktur Pori-Pori.* Doctoral dissertation, Institut Teknologi Bandung, Indonesia.

[20] Wibowo, A. S., Permadi, P. (2013). A type curve for carbonates rock typing. Presented at the IPTC Beijing, China, 26–28 March. IPTC-16663. https://doi.org/10.2523/IPTC-16663-MS.

[21] Wyllie, M. R. J., Gregory, A. R., Gardner, I. W. (1956). Elastic wave velocities in heterogeneous and porous media. *Geophysics*, 12 (1), pp. 41–70.

[22] Xu, S. & Payne, M. A. (2009). Modeling Elastic Properties in Carbonate Rocks. *The Leading Edge*, 28, 1, pp. 66–74.

APPENDIX

Data used for this study were reported in Prasad (2003) and are listed in *Table A-1*. The source numbers in *Table A-1* correspond to the following authors: 1 = Assefa and Sothcott (1997), 2 = Prasad et al. (1999), 3 = Klimentos and McCann (1990), 4 = Lucet (1989), 5 = Prasad and Manghnani (1997), 6 = Tao et al. (1995). All values in the table are given for effective pressures around 40 MPa.

Table A-1

The data set used for this study

Source number	Porosity (%)	Porosity (v/v)	Clay (%)	Vp (m/s)	Qp	Permeability (mD)
1	3.41	0.0341	6.76	5,171	97	0.02
1	3.46	0.0346	0	5,091	62	0.005
1	4.89	0.0489	0	5,048	42	0.02
1	6.36	0.0636	26.2	4,695	17	0.06
1	7.52	0.0752	0	4,735	37	0.02
1	9.79	0.0979	9.75	3,917	22	0.28
1	13.4	0.134	0	4,126	33	2.51
1	17.35	0.1735	2.71	3,780	31	0.24
2	19.1	0.191	10	3,488	8	1.4
2	23.2	0.232	10	3,580	34	22
2	23.4	0.234	5	3,751	19	295
2	23.9	0.239	9	3,601	17	68
2	25.2	0.252	9	3,466	13	818
2	26.9	0.269	4	3,726	21	1,030
3	8.96	0.0896	6	4,947	22	0.13
3	9.96	0.0996	7	4,705	32	0.01
3	10.22	0.1022	9	4,895	12	0.16
3	11.39	0.1139	6	4,666	37	0.46
3	13.11	0.1311	7	4,666	28	3.67
3	13.47	0.1347	14	4,498	12	0.06
3	13.72	0.1372	0.5	4,950	613	87.65
3	14.15	0.1415	1	4,960	79	150.7
3	14.37	0.1437	1	5,078	185	255.9
3	14.47	0.1447	0.2	4,788	712	220.9
3	15.13	0.1513	4	4,794	34	11.06
3	15.18	0.1518	0.7	4,942	394	160.4

Source number	Porosity (%)	Porosity (v/v)	Clay (%)	Vp (m/s)	Qp	Permeability (mD)
3	15.41	0.1541	15	4,246	19	52.42
3	15.46	0.1546	15	4,152	21	0.05
3	15.72	0.1572	5	4,564	127	87.55
3	16.11	0.1611	15	4,152	20	50.51
3	16.5	0.165	15	4,149	18	41.74
3	16.65	0.1665	12	4,010	29	0.37
3	16.71	0.1671	8	4,381	40	0.44
3	17.13	0.1713	12	3,933	26	2.21
3	17.18	0.1718	15	4,362	9	0.13
3	21.19	0.2119	15	3,700	31	11.42
3	21.73	0.2173	22	3,572	22	7.1
3	22.2	0.222	25	3,500	10	1.13
3	25.41	0.2541	20	3,314	20	5.78
3	26.32	0.2632	20	3,299	25	10.27
3	27.12	0.2712	25	3,000	11	0.45
3	27.33	0.2733	5	3,666	27	305.8
3	27.39	0.2739	23	2,952	10	9.3
3	27.73	0.2773	17	3,090	19	3.5
3	27.87	0.2787	17	2,990	18	9.59
3	27.96	0.2796	15	3,675	18	33.67
3	28.04	0.2804	20	3,181	18	10.05
3	28.79	0.2879	18	3,056	20	5.47
3	28.87	0.2887	23	2,909	19	7.03
3	30.31	0.3031	12	3,627	17	17.77
3	33.59	0.3359	15	3,195	16	2.25
3	35.09	0.3509	30	3,108	10	73.26
3	36.04	0.3604	16	3,121	19	21.16
4	20.3	0.203		3,754	33	8
4	20.3	0.203		3,707	31	8
4	20.3	0.203		3,771	41	8
4	20.9	0.209		3,867		2,040
4	20.9	0.209		3,976	48	2,040
4	20.9	0.209		3,903		2,040
4	20.9	0.209		3,921		2,040

Source number	Porosity (%)	Porosity (v/v)	Clay (%)	Vp (m/s)	Qp	Permeability (mD)
4	24.6	0.246		3,572	38	58
5	21	0.21	4	4,400	100	100
5	21	0.21	4	4,400	100	100
6	17	0.17	<1	4,460	65	1,170.7
6	17.1	0.171	1	4,300	35	587.8
6	22.1	0.221	1	3,770	59	794.2
6	25.9	0.259	3	3,060	26	977.1

Geosciences and Engineering, Vol. 6, No. 9 (2018), pp. 118–126.

EXAMINATION OF DEBRECEN'S 110-YEAR RAINFALL DATA

CSABA ILYÉS[1]–ENDRE TURAI[2]–PÉTER SZŰCS[3]–TAMÁS ILYÉS[4]

[1] Assistant Research Fellow, Institute of Environmental Management,
Faculty of Earth Science and Engineering, University of Miskolc,
MTA-ME Geoengineering Research Group
e-mail: hgilyes@uni-miskolc.hu
[2] Associate Professor, Institute of Geophysics and Geoinformatics,
Faculty of Earth Science and Engineering, University of Miskolc
[3] Professor, Institute of Environmental Management
Faculty of Earth Science and Engineering, University of Miskolc
MTA-ME Geoengineering Research Group
[4] PhD student, Faculty of Sciences University of Pécs

Abstract: In this examination the cyclic properties of rainfall data were prepared. To complement other climate change research, we defined the deterministic cycles of a 110-year-long precipitation dataset, both annual and monthly.

The sample area of Debrecen was chosen to for these calculations, and we defined 18 locally important cycles from annual rainfall and several other important cycles from monthly sampled datasets with spectral analysis based on the Discrete Fourier Transform. With the defined cycles and amplitudes, we calculated forecasts up to 2030 as well as analyzing the time-dependency of the cycles.

Keywords: *Debrecen, hydrology, precipitation, time series, wavelet*

INTRODUCTION

In climate research, the investigation of long-term datasets is becoming ever more important. At present it is possible to investigate 110-year-long equidistantly sampled datasets. It is also clear that climate change or extreme weather conditions can influence the water cycle on a global as well as on a local scale, and several scientists argue that the cycle's speed is increasing [1]. Water management practice should be able to handle these changes to fulfill increasing water demands. More and more water-related hazards are being observed all over the world. To solve water-related problems successfully, the cyclic behavior of water cycle components needs to be understood.

MATERIALS AND METHODS

Mathematical basis of spectral analysis

There are several ways to examine long-term time-series data, one of which is spectral analysis based on the Discrete Fourier Transform [2, 3].

With the Discrete Fourier Transform (DFT), the spectrum can be calculated with the following equation:

$$Y(T) = \int_{t=-\infty}^{\infty} y(t) e^{-j\frac{2\pi}{T}t} dt \tag{1}$$

where t is time, the independent variable of the registration, $y(t)$ is the recording, registered signal, j is an imaginary unit, T indicates the period, the length of a cycle, and $Y(T)$ is the spectrum of the registered signal.

$$Y(T) = \mathrm{Re}[Y(T)] + j\,\mathrm{Im}[Y(T)] \tag{2}$$

$$Y(T) = A(T) e^{j\Phi(T)}, \tag{3}$$

where $Re[Y(T)]$ denotes real spectra, the first part of the complex spectra; $Im[Y(T)]$ denotes imaginary spectra, the second part of the complex spectra, $A(T)$ is the amplitude of the complex spectra, and $\Phi(T)$ is the phase angle of the complex spectra.

The amplitude and phase angle can be calculated from the real and imaginary spectra [4]:

$$A(T) = \sqrt{\mathrm{Re}[Y(T)]^2 + \mathrm{Im}[Y(T)]^2}, \tag{4}$$

$$\Phi(T) = arctg \frac{\mathrm{Im}[Y(T)]}{\mathrm{Re}[Y(T)]}. \tag{5}$$

With the previously discussed amplitude spectrum and phase spectrum, the original dataset can be recalculated, but when only using the major and additional cycles, a deterministic time series can be defined:

$$y(t)^{det} = \bar{Y} + \frac{2}{t_{reg}} \sum_{i=1}^{I} A_i \cos\left[\frac{2\pi}{T_i}(t - 1901) + \Phi(T_i)\right] \tag{6}$$

where $y(t)^{det}$ indicates data calculated from the deterministic components, $\bar{Y}$ is expected value, declared static through the examined period, t_{reg} is length of the dataset, T_i is the period of cycle I, I is the number of the deterministic cycles, $\phi(T_i)$ is the phase angle of cycle i, and A_i is the amplitude of cycle i.

The linear relation between the original measured y(t) data and the deterministic $y(t)^{det}$ data, or the error term of the calculated data, which can be calculated with

the Pearson-correlation coefficient, can be interpreted as the stochasticity in the time series.

If the t value exceeds the year 2010, predictions can be calculated for the future. In this paper the periodic components of the Debrecen dataset were used and a forecast was delivered up to the year 2030.

Wavelet-analysis

Wavelet time series analysis is a well-known method to investigate the time-dependence of a cycle within a time series. The shape of the cycles searched for in the registered signals can be described with harmonic functions; in the examination sine wave packet was used [5].

To carry out the wavelet analysis, a cross-correlation function is used [Rxy(τ)]:

$$R_{xy}(\tau) = \frac{1}{t_{reg}} \int_{\tau=t_{\min}}^{t_{\max}} x(\tau)\, y(t+\tau) dt \,. \tag{7}$$

A normalized cross-correlation function is:

$$R_{xy}^{(N)}(t) = \frac{R_{xy}(t)}{Max\{R_{xy}(t)\}} \,. \tag{8}$$

Materials

The data was acquired from the Hungarian Meteorological Service's Online Database [6], which contains several types of meteorological data from five different stations. Monthly and annual precipitation data from Debrecen covering a period of 110 years (1901–2010) were analyzed. The calculation was calculated with self-made software for spectral analysis.

For interpreting the results, the term "relative amplitude spectra" was defined, which means the values of the amplitude spectrum compared to the absolute maximum of the amplitude spectrum.

RESULTS AND DISCUSSION

Spectral analysis

First, we examined the annual rainfall data from Debrecen, where the registration period is 1901–2010. Thus the length of the registration period is t_{reg} = 110 years, meaning the number of samples are for each city is 110. With this method, the minimal length of the period – called the Nyquist period – can be calculated; it is 2 years in this case. The results of the spectral analysis, the cycles and their relative amplitude are shown in *Figure 1*.

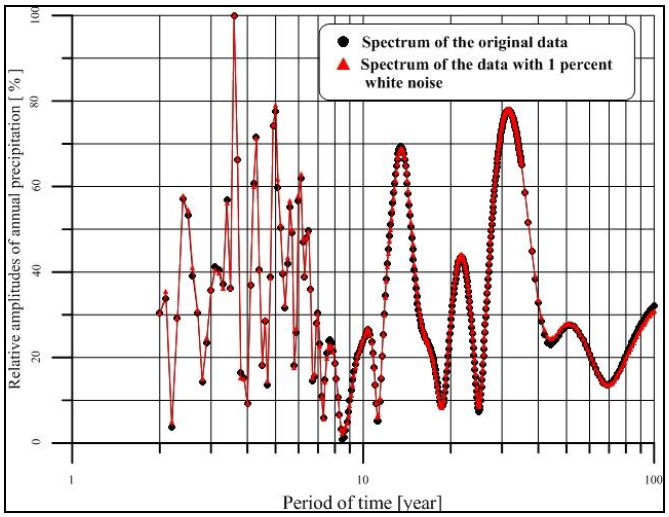

Figure 1. *Relative amplitude spectra from annual rainfall data of Debrecen, with 1% white noise*

From annual rainfall data 18 cycles were determined, 10 of which are major cycles. The most dominant cycle was 3.6 years long, with 100% amplitude, and most of the other main cycles were between 27 and 77%. The following dominant cycles are 5-year-long cycles and the 31-year-long cycles. The calculation with white noise showed a similar result; based on this the spectra from Debrecen were accepted to be correct.

The monthly precipitation datasets contain monthly rainfall data from January 1901 to December 2010, so the length of the registration period $t_{reg} = 1320$ months.

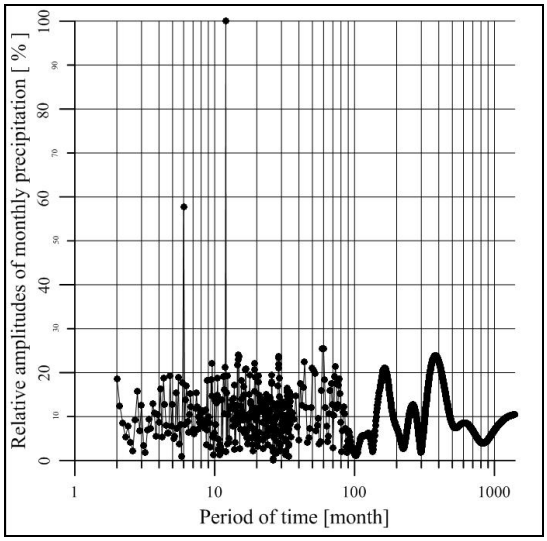

Figure 2. *Relative amplitude spectra from monthly rainfall data of Debrecen*

In the analysis of the Debrecen data, 43 cycles were detected *(Figure 2)*. In this case, the 1-year-long cycle had the 100% relative amplitude spectrum, and the six month long had the relative amplitude spectrum of 57.64%. The other cycles were additional cycles. The additional dominant cycles were the 59-month, 14.7-month, and 378-month cycles; most of the minor cycles have a relative amplitude range under the 20% value but were considered important in the precipitation dataset.

Forecasting

For this investigation the cyclic components of the annual and monthly precipitation data were used. We developed several scenarios to test the forecasting method.

First, 10 major cycles were used to calculate a deterministic rainfall dataset, and we made predictions up to the year of 2030. Teaching took place with the data between 1901 and 2010, and the validation phase was between 2010 and 2016 [7]

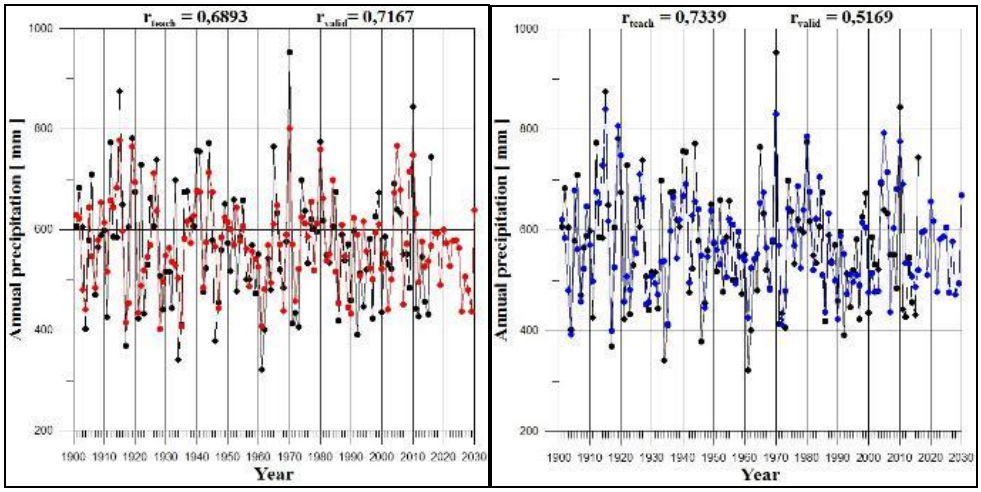

Figure 3. *Calculated rainfall data in the Debrecen area from 10 cycles (left) and from 18 cycles (right)*

Calculating with 10 dominant cycles, the correlation coefficient with the original measured data is 0.6893 in the teaching phase, and becomes higher in the validation phase. In the forecast the calculated annual rainfall data is between 400 and 600 mm, with a maximum value in 2030. The expected value between 1901 and 2010 is 574.8 mm/year, with a standard deviation of 89.7 mm/year, and for the predicted period, the average is 546.7 mm/year, with a standard deviation of 56.5 mm/year. The decrease from the teaching period is 5%.

When we used 18 cycles for the calculation, the correlation coefficient became higher, 0.7339. The values of the forecasting interval are 450 to 650 mm, without any extreme data. The expected value for the teaching phase is 574.4 mm/year, with 98.7 mm/year standard deviation, and for the forecasting phase 559.4 mm/year, with a standard deviation of 66.1 mm/year.

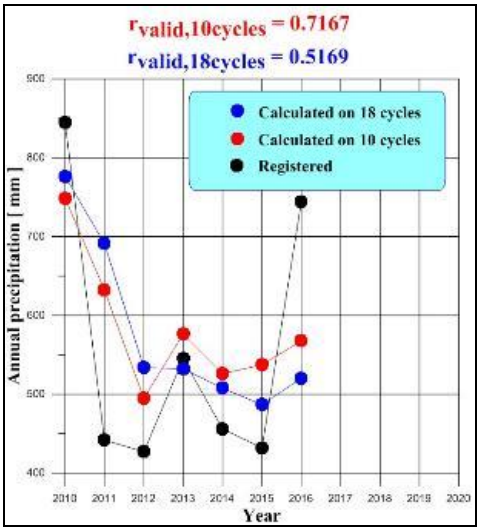

Figure 4. *Correlation in the validation phase*

As seen in *Figure 4*, the original measured and the calculated values show a strong connection for this short interval: the correlation coefficients are 0.7167, and 0.5169 with 10 and 18 cycles respectively. The only major difference between the measured and the calculated data is for the year of 2016.

The calculation was delivered also using the monthly dataset, but even with 164 cycles the correlation coefficient was only 0.62, which can be considered as moderate. The results also show that with fewer cycles a more adequate forecast can be calculated, so the number of necessary cycles for the calculations can be a direction of future studies [8].

Wavelet-analysis

For this analysis we used the cycles defined from the Debrecen dataset, with a sine wave packet with unit amplitude, and with the periods of time detected previously.

In *Figure 5* the correlation coefficient shows years when the cycle was more or less dominant.

For the examination all of the calculated periodic components were used, in this paper we present the more interesting ones, as the cycles with smaller periods of time showed many similarities.

The wavelet of the smaller cycles shows local maximum values in the 1910s, 1940s and 1970s, as seen in the graph of the 4.3 and the 5-year-long cycles. Much less dominance can be noticed after the year of 2000.

As for cycles with a longer period of time, a more consistent graph can be seen *(Figure 5)*. The time distribution of these cycles shows that the longer periods are not showing any changes in the examined time interval as opposed to the shorter cycles.

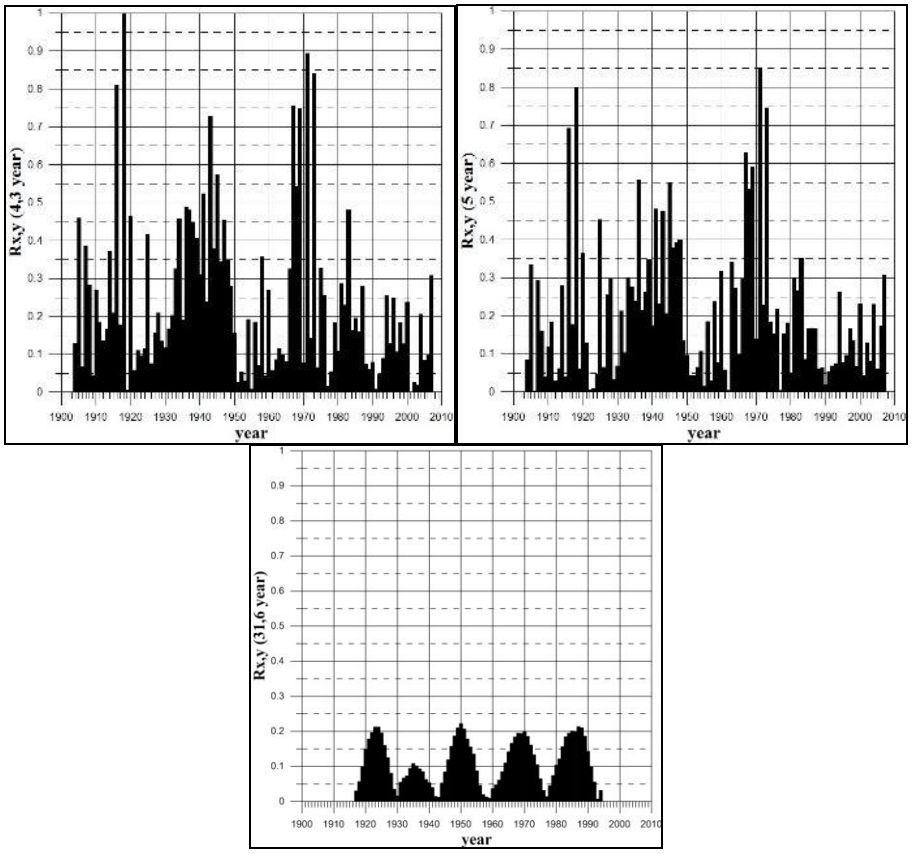

Figure 5. *Wavelets of the dominant cycles*

With this method a certain year can be examined as well, as seen in *Figure 6*.

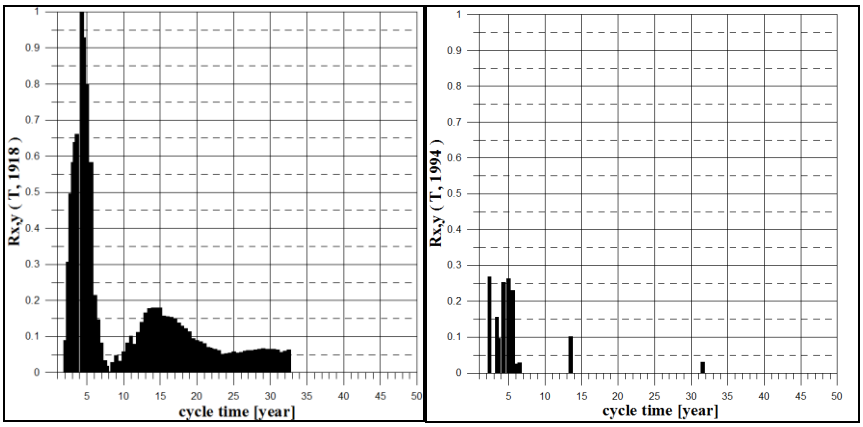

Figure 6. *Dominance of the different cycles in the year of 1918 (left) and 1994 (right) in Debrecen*

As seen in the graph the correlation coefficient of the cycles is much smaller in 1994 than in 1914, which can mean that the dominance of the shorter cycles is less relevant at the end of the 20th century.

CONCLUSION

Based on our research, we analyzed 110-year-long rainfall records and defined several cycles that can describe the climate of the city of Debrecen. Also we developed a forecasting method that was tested in that area and we analyzed the time distribution of the cycles.

In this changing climate, finding deterministic values in a hydrological or meteorological parameter can be helpful to better understand the climate, and several uncertainties of rainfall events can be reduced by using this method.

Directions of future studies could be to understand the reasons for the cycles as well as finding a connection with the cycles of hydrogeological parameters, shallow and deeper groundwater levels.

ACKNOWLEDGEMENT

The research was carried out within the GINOP-2.3.2-15-2016- 00031 *Innovative solutions for sustainable groundwater resource management* project of the Faculty of Earth Science and Engineering of the University of Miskolc in the framework of the Széchenyi 2020 Plan, funded by the European Union, co-financed by the European Structural and Investment Funds.

REFERENCES

[1] Szöllősi-Nagy, A. (2018). A klímaváltozás a vízről szól? (Is climate change all about the water?). *Innotéka*, Vol. 8, No. 5, pp. 29–33.

[2] Bath, M. (1974). *Spectral Analysis in Geophysics*. Amsterdam–Oxford–New York: Elsevier Scientific Publishing Company.

[3] Bracewell, R. N. (1978). *The Fourier Transform and its Applications*. Oxford: McGraw-Hill Book Co.

[4] Candy, V. J. (1985). *Signal Processing – The Model-based Approach*. Oxford: McGraw-Hill Book Company.

[5] Nason, G. P. & von Sachs, R. (1999). Wavelets in time series analysis. *Philosophical Transactions of the Royal Society A-mathematical Physical and Engineering Sciences*, Issue 357, pp. 2511–2526.

[6] HMS 2015. *Hungarian Meteorological Service Online Database*. [Online] Available at: http://www.met.hu/eghajlat/magyarorszag_eghajlata/eghajlati_adatsorok/ [Accessed 1 July 2015].

[7] HCSO 2016. *Hungarian Central Statistical Office StaDat Database – 5.10.4*. A meteorológiai megfigyelőállomások főbb adatai (1985–). [Online] Available at: https://www.ksh.hu/docs/hun/xstadat/xstadat_eves/i_met002c.html [Accessed 31 Aug 2016].

[8] Ilyés, Cs., Turai E., Szűcs P. (2018). Examination of rainfall data for 110 years using spectral and wavelet analysis. *Central European Geology*, Vol. 61, Issue 1, pp. 1–15.

Geosciences and Engineering, Vol. 6, No. 9 (2018), pp. 127–141.

EFFECTS OF EARTHQUAKE DATA CLUSTERING ON THE RESULTS OF STRESS INVERSIONS

LILI CZIROK[1*]–LUKÁCS KUSLITS[2]

[1]*University of Sopron, Roth Gyula Doctoral School, Sopron*
[2]*MTA CSFK Geodetic and Geophysical Institute, Sopron*
[*]*cziroklili@ggki.hu*

Abstract: An important criterion of stress inversions is the homogeneous stress field of the studied area. Therefore, it is necessary to take into account the variability of used focal mechanism solutions (FMS) and create some subareas for estimations. If there are a large number of earthquakes, it is worth generating the clusters automatically.

This research has two aims:

Firstly, effects of the existing clusterization methods are analysed by the authors. Clusters of earthquake data are created based on three methods: (a) manual grouping based on the FMS map, (b) k-means algorithm and (c) an automatized, nearest neighbour-based method. The input data for clustering were in each case the epicentral coordinates of the investigated earthquakes.

Secondly, the authors have begun developing a new, automatized clustering method that does not require a minimal number of cluster members or any other manually given parameter but whose reliability is similar to that of the manual method.

The applied stress inversion is a linear, iterative method that uses the Mohr-Coulomb law to analyse the fault instability of input data (using the code STRESSINVERSE). Focal mechanisms used for calculation are situated in the Vrancea Zone (SE Carpathians).

Keywords: *focal mechanism solutions, stress inversions, clustering algorithms, SE-Carpathians*

INTRODUCTION

Tectonics

The South-eastern Carpathians are an interesting part in the Eurasian plate because of their geodynamic activity characterized by an ongoing subduction processes. This has two main indications in the Carpathian Bends: the Ciomadul Volcano and the Vrancea Zone.

In the Inner Carpathians, there are post volcanic activities produced by the Ciomadul Volcano. From the Late Jurassic to the Early Cretaceous, a volcanic mountain range evolved due to the subduction of the Neo-Tethys. The Ciomadul Volcano is the youngest and the southernmost member of this chain. It erupted about 30,000 years ago, that being the last volcanic eruption in the Carpathian Basin [1].

The Vrancea Region is a complex seismic region which has been active since the closure of Ceahlau-Severin Ocean between the late Early and Late Cretaceous [2]. Nowadays, this subduction event is still in progress. Moreover, three tectonic units converge here: the East European Plate and the Intra-Alpine and Moesian subplates, evoking major seismic and geodynamic activity. As for intermediate-depth earthquakes' focal mechanism solutions, reverse faults are the dominant tectonic regime but stress orientations are variable. Normal faults and strike-slips also occur in the Vrancea Zone due to the complicated tectonic situation. *Figure 1* presents the tectonic situation in Romania [2].

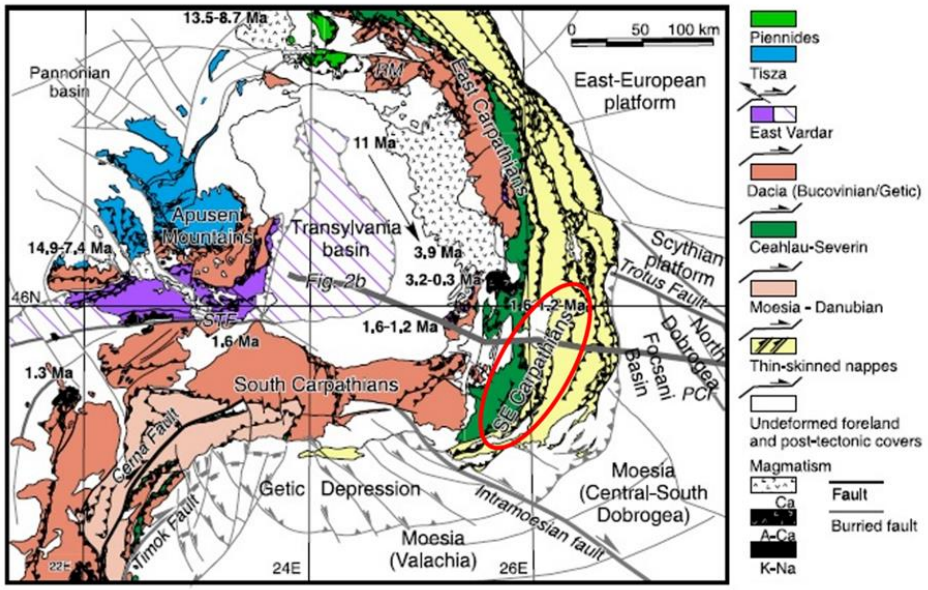

Figure 1. *The tectonic units in Romania.*
The red circle outlines the studied area (SE Carpathians) [2]

Previous studies

Martínez-Garzón et al. [3] carried out stress inversions for the region of San Jacinto Fault Zone. On the 4th April 2010, a M_w 7.2 earthquake occurred in the area followed by two larger seismic events (having local magnitudes M_L 4.3 and 5.2). In the relocated seismicity catalogue, there were roughly 5,400 events until the end of 2010, about 3,400 of which have focal mechanism solutions. In this publication [3], the authors developed a refined methodology for stress inversion. They classified seismic events using a k-means algorithm and then applied the mixture of two stress inversion methods: Michael's [4] and Vavrycuk's method [5].

Hardebeck and Michael [4] presented a damped, linear inversion method that creates groups before the carrying stress inversion. The code MSATSI (Martinez-Garcon et al. 2014) [6], has an option for setting the number of minimum events falling into a grid point. After the clustering of input data, stress inversion routines assign each

clustered set of earthquakes to one geographic point for the computations, called a grid point or node. Based on this setting, the program creates the groups for the formal stress inversion and executes the estimations. Nevertheless, the reliability of the stress tensor is lower than that computed by STRESSINVERSE, as this algorithm cannot distinguish between the correct and auxiliary fault planes. For the code STRESS-INVERSE, FMS data need to be classified before using them as input data [5].

DATA

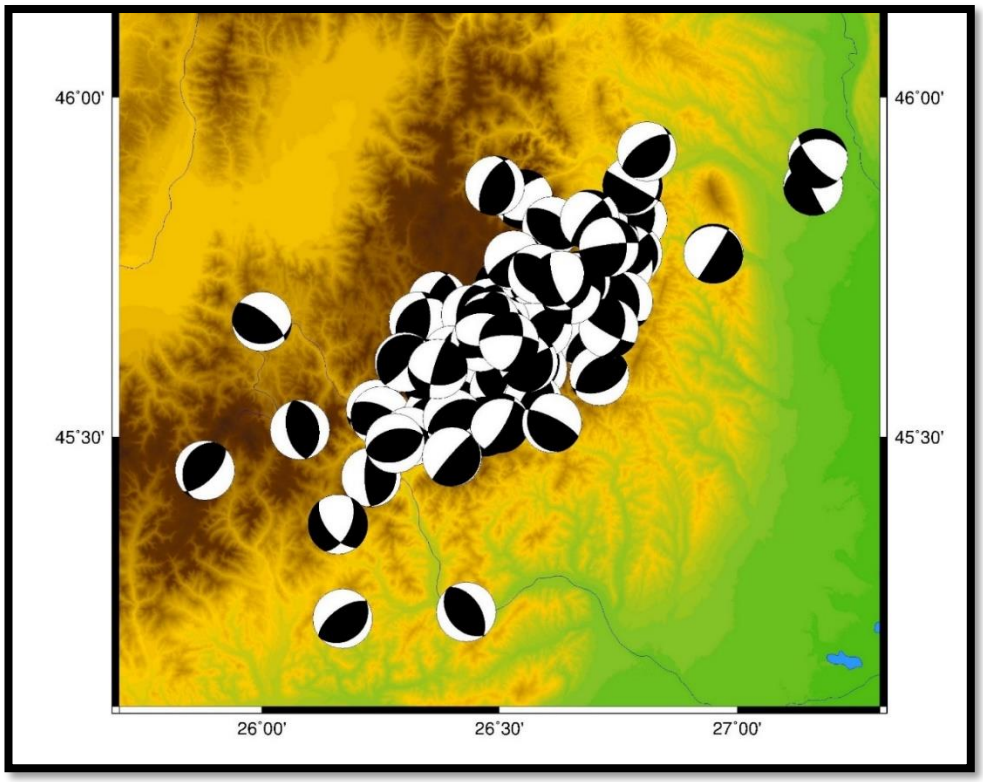

Figure 2. *Selected focal mechanism solutions in the Vrancea-zone used for the clusterization. The map is created using Generic Mapping Tools*

For these estimations, there were altogether 84 focal mechanism solutions, available from 1978 to the very recent days (the last solution was determined on March 14, 2018). The most important data source is the Romanian National Institute for Earth Physics (Institutul National de Cercetare-Dezvoltare pentru Fizica Pamantului). Seismic moment tensors were determined using two codes: FMNEAR [7] and ISOLA-GUI [8]. FMNEAR applies a fully-automated waveform inversion on seismic records of near-earthquake stations. Moment tensors are computed in near real-time. The ISOLA-GUI is also a waveform-inversion method but it is not automatic.

Earlier focal mechanism solutions (until the 1990s) originate from the websites of the National Institute of Geophysics and Volcanology [9] and Incorporated Research Institutions for Seismology [10].

Figure 2 is a map of used focal mechanism solutions in the Vrancea Region. The map was created using Generic Mapping Tools.

CLUSTERING METHODS

It is visible in *Figure 2* that most of the earthquakes are concentrated in a relatively small region (having an area of about 220 × 150 km^2). Because of that, other clustering methods (a k-means algorithm and an automatic, nearest neighbour-based algorithm) were applied to compare final results obtained using them with results using manual classification of the FMS map.

Manual clustering

Subareas for the stress inversion were generated based on the' latitude and longitude coordinates of epicentres. Moreover, the homogeneity of the stress field was also an important criterion. The FMS map *(Figure 2)* was used for classification. A total number of 8 clusters (shown in *Figure 3*) were finally created as inputs for each individual estimation. In *Figure 3*, two other thematic maps are also represented: a tectonic map of the study area [11] and a digital elevation model produced by the Shuttle Radar Topography Mission [12].

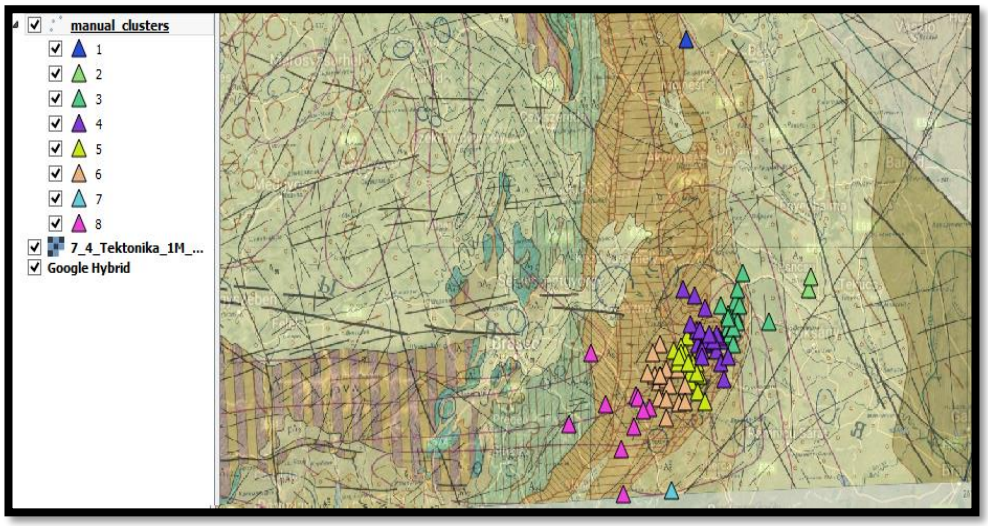

Figure 3. *Classes created manually (in a rather subjective way) based on the map of focal mechanisms (shown in* Figure 2*)*

k-means clustering

Here, k-means clusters for the inversion were created using the STATISTICA programme [13] [14] [15]. In this case, altogether 8 clusters were generated based on the seismic events' coordinates. The result of this algorithm is visible in *Figure 4*.

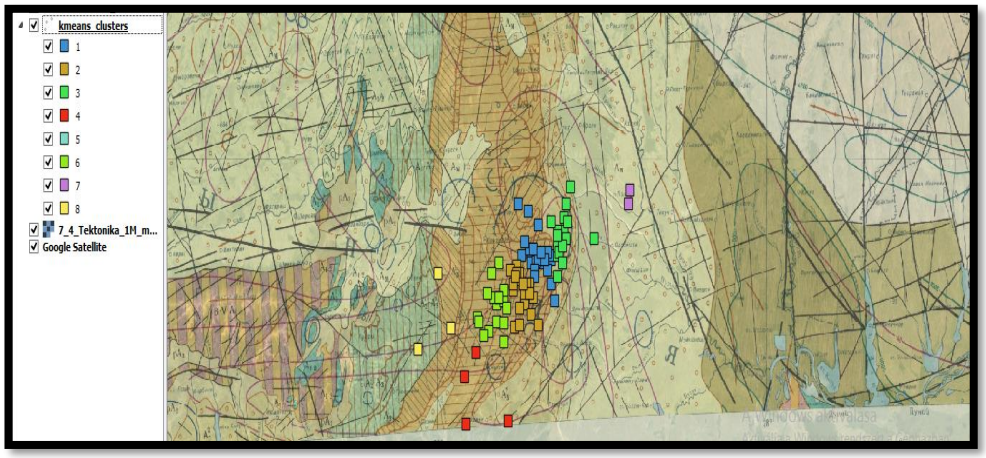

Figure 4. *Classes created using k-means clustering*

Automatized method

The automatic algorithm presented here is based on the principle of nearest neighbours, essentially resulting in a simpler version of an agglomerative hierarchical clustering method [14]. Euclidean distances were the applied metric for linkage, which only prepares the first row of the dendrogram, and only searches for the closest two points of the whole remaining dataset when creating a new cluster. It operates using the following iterative computational steps:

1) For the clustering, the distance matrix of the investigated points is determined *(Figure 5)*.
2) Non-identical points positioned closest to each other, then form the initial cluster points *(Figure 6)*.
3) Each cluster is then linked with unclassified points positioned closest to points already part of a cluster *(Figure 6)*. This step is repeated as long as there is still a new point to be identified.
4) If clusters cannot be further enlarged, the iteration returns to step 2 using the remainder of the dataset until all points are classified *(Figure 7a)*.
5) It is possible to set a threshold distance value to isolate "lonely" points that are too far away from their nearest neighbours in the dataset *(Figure 7b)*. This is an important feature, because such points can probably behave as noise for the calculations and potentially bias the stress-field estimation [16].

The steps of this clustering method are presented in *Figures 5–7*.

	1	2	3	4	5	6	7	8	9	10
1	0	5.0990	8.2462	4.4721	7.8102	1	2	10	12.0416	4.4721
2	5.0990	0	7.6158	1.4142	4.1231	6.0828	7.0711	7.0711	8.5440	4.2426
3	8.2462	7.6158	0	6.3246	5	8.5440	8.9443	4	6.0828	4
4	4.4721	1.4142	6.3246	0	3.6056	5.3852	6.3246	6.3246	8.0623	2.8284
5	7.8102	4.1231	5	3.6056	0	8.6023	9.4340	3	4.4721	4.1231
6	1	6.0828	8.5440	5.3852	8.6023	0	1	10.6301	12.7279	5
7	2	7.0711	8.9443	6.3246	9.4340	1	0	11.3137	13.4536	5.6569
8	10	7.0711	4	6.3246	3	10.6301	11.3137	0	2.2361	5.6569
9	12.0416	8.5440	6.0828	8.0623	4.4721	12.7279	13.4536	2.2361	0	7.8102
10	4.4721	4.2426	4	2.8284	4.1231	5	5.6569	5.6569	7.8102	0
11	6.7082	5.3852	2.2361	4.1231	3.1623	7.2111	7.8102	3.6056	5.8310	2.2361
12	1.4142	6	7.6158	5.0990	8.0623	1	1.4142	9.8995	12.0416	4.2426
13	8.2462	9.8995	4	8.4853	8.5440	8.0623	8	8	10.0499	5.6569
14	6	1.4142	8.9443	2.8284	5	7	8	8	9.2195	5.6569
15	11.4018	8.2462	5.0990	7.6158	4.1231	12.0416	12.7279	1.4142	1	7.0711
16	9.4340	7	3	6.0828	3.1623	10	10.6301	1	3.1623	5
17	3.1623	4.4721	5.0990	3.1623	5.3852	3.6056	4.2426	7.0711	9.2195	1.4142
18	25.4951	21.6333	18.6011	21.4009	17.8045	26.1725	26.8701	15.5563	13.4536	21.2132
19	12.7279	8.9443	7.0711	8.6023	5	13.4536	14.2127	3.1623	1	8.6023
20	12.3693	7.2801	11.1803	8.0623	6.3246	13.3417	14.3178	7.8102	7.2111	10.0499
21	24	23.5372	16.1245	22.3607	19.9249	24.0208	24.0832	17.0880	17	20.0998
22	29.0172	28.2843	21.0238	27.1662	24.5153	29.0689	29.1548	21.5870	21.1896	25.0200
23	12.5300	7.8102	9.2195	8.0623	5.0990	13.4164	14.3178	5.3852	4.2426	9.2195

Figure 5. *Distance matrix of the points of the test dataset; red cells indicate points forming the first cluster*

Figure 6. *Schematics of the algorithms operation. Application of iterative steps 2 and 3 using the principle of nearest neighbours for creating the cluster of points highlighted with orange*

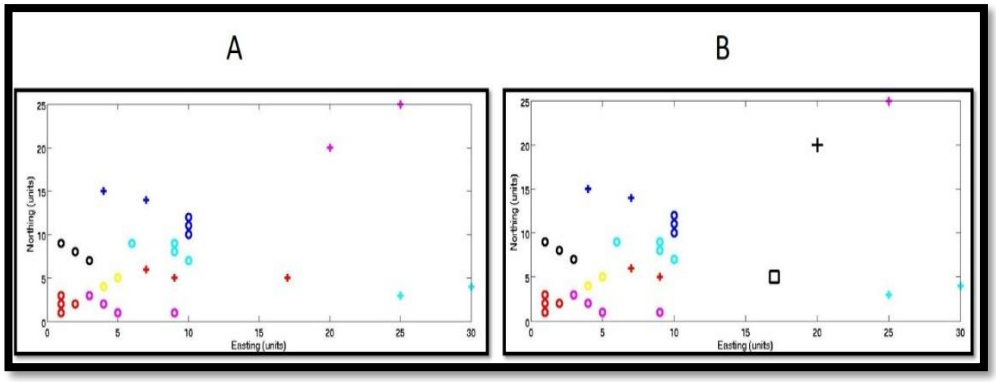

Figure 7. *Two clustering results using the same example dataset, on the left without (A) and on the right with a threshold value of 6 units for distance (B). Here this threshold value was introduced in order to separate the highlighted points (thick black cross and square, pink cross), which can be considered outliers from all the other groups*

In case of the Vrancea Region, no critical distance was applied. The input data and results can be seen in *Figure 8*. This algorithm produced a relatively large number of 28 classes for the analysis of stress relations.

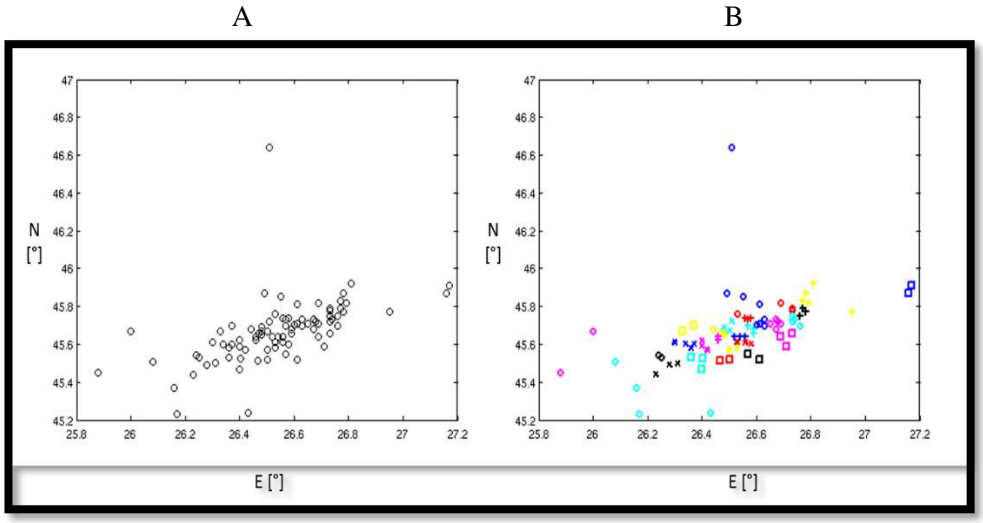

Figure 8. *The epicenters of seismic events (A) and the clusters (B) generated without critical distance in a MATLAB environment*

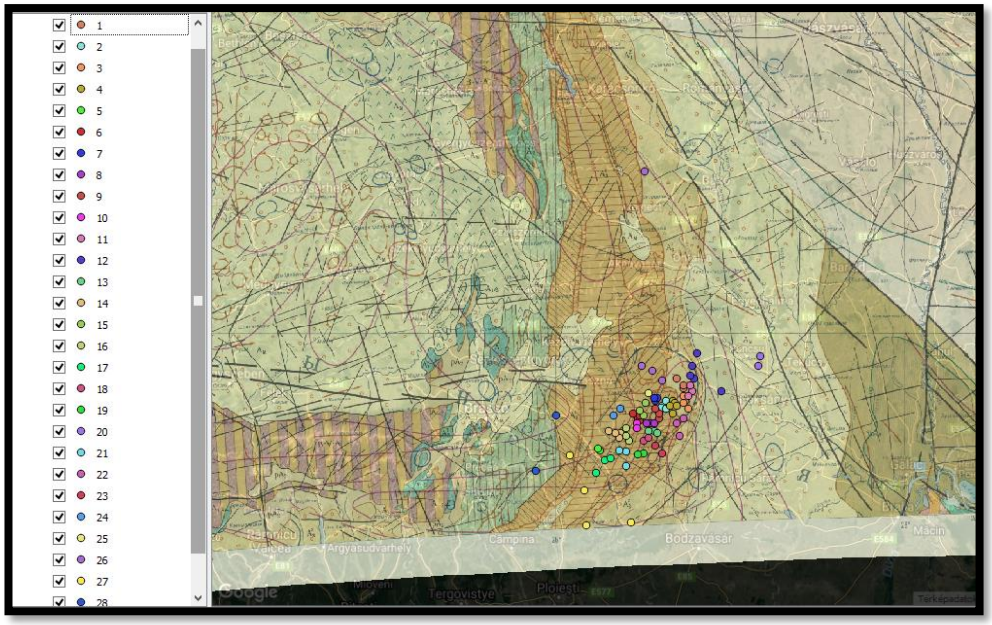

Figure 9. *Classes created using the automatized method plotted in Quantum GIS*

RESULTS OF STRESS INVERSIONS IN THE VRANCEA REGION

In the current publication, the authors applied the code STRESSINVERSE in MATLAB environment for computing the estimations.

Results using manual clustering

The azimuths of maximum horizontal stress directions (S_H) and the vertical principal (σ_V) stress axes were determined as in [17] and [18]. The best R values were calculated by the error analysis of this stress inversion method. The distributions of all R values were illustrated using histograms (shown in *Figures 10–12*). The maximum of the histograms presents the best values of shape ratios (R_{best}).

Table 1

Estimated orientations of the principal stress axes and the best R values

Number of cluster	Amount of events	Largest plunge (°) and σ_V		Azimuth (°) and S_H		R_{best}
1.	1	48.86	σ_1	150.33	$\sigma_3 + 90°$	0.5752
2.	2	55.71	σ_1	213.51	σ_2	0.6288
3.	15	76.73	σ_3	323.63	σ_1	0.5802
4.	22	78.49	σ_3	13.33	σ_1	0.1858
5.	17	83.08	σ_3	232.84	σ_1	0.2317
6.	16	83.43	σ_3	289.67	σ_1	0.5219
7.	1	80.02	σ_3	51.77	σ_1	0.7483
8.	10	81.28	σ_3	168.49	σ_1	0.4381

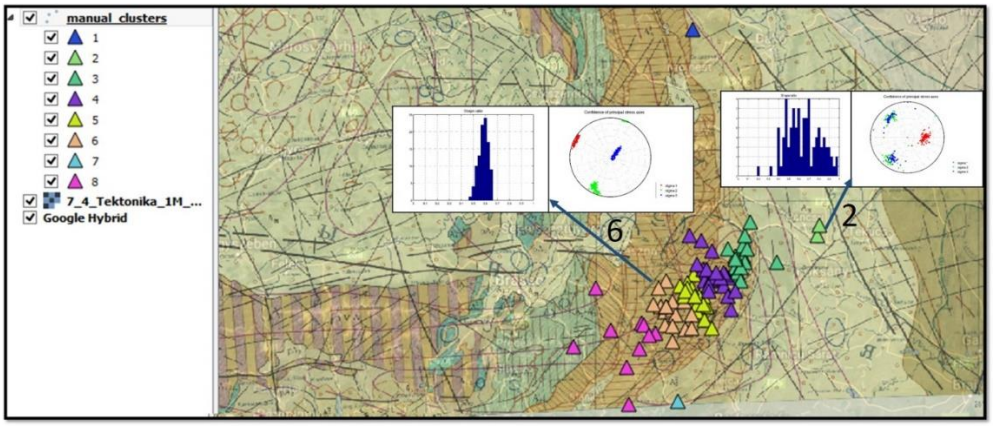

Figure 10. *R-histograms and stereograms of the 6th group and 2nd group*

In *Figure 10*, the 6th and 2nd clusters' R histograms and stereograms are shown. The 2nd cluster has the least reliable stress tensor – the spread of R values is large and the σ_2- and σ_3-axes cannot be distinguished on the stereogram. Thus, the exact stress relations cannot be evaluated by the estimated orientations. In the case of the 6th cluster, principal axes directions could be identified very clearly

Results using the k-means method

Table 2

Estimated orientations of the principal stress axes and the best R values

Number of cluster	Amount of events	Largest plunge (°) and σ_V		Azimuth (°) and S_H		R_{best}
1.	22	76.15	σ_3	358.56	σ_1	0.1744
2.	20	79.2	σ_3	256.86	σ_1	0.4983
3.	16	74.75	σ_3	313.3	σ_1	0.4572
4.	4	52.02	σ_3	18.82	σ_1	0.3253
5.	1	48.86	σ_1	150.33	$\sigma_3 + 90°$	0.5752
6.	16	86.84	σ_3	139.25	σ_1	0.5711
7.	2	48.16	σ_1	302.46	$\sigma_3 + 90°$	0.6547
8.	3	78.55	σ_3	172.29	σ_1	0.1652

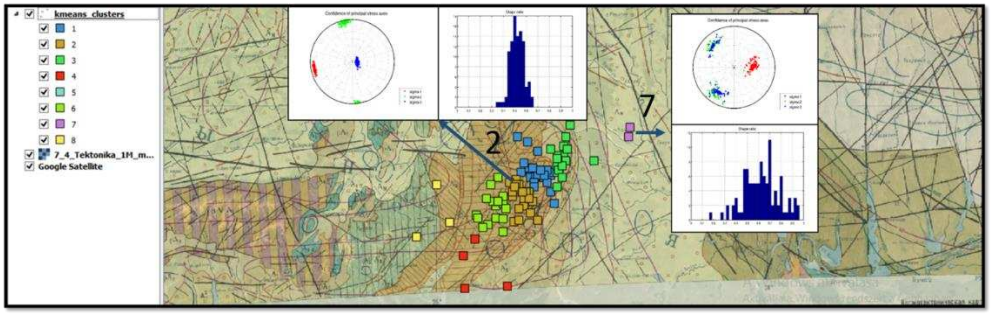

Figure 11. *R histograms and stereograms of the 7th group and 2nd group*

In the case of k-means clustering, results of the 7th group are the least reliable. This group is identical to the 2nd cluster of manual grouping (shown in *Figure 10*). As it is visible, the orientations of principal stress axes cannot be identified accurately based on their stereogram. Here, the 2nd group has the most reliable stress tensor, which also significantly overlaps the 6th group of the manual classification. In this case, the orientations of principal stress axes are similar. All the principal axes can be identified well and the best R values can be determined unambiguously.

Results using the automatized method

Table 3

Estimated orientations of the principal stress axes and the best R values

Number of cluster	Amount of events	Largest plunge (°) and σ_V		Azimuth (°) and S_H		R_{best}
1.	3	65.5	σ_3	305.79	σ_1	0.3579
2.	4	58.96	σ_3	105.53	σ_1	0.655
3.	4	66.38	σ_3	227.63	σ_1	0.1624
4.	5	72.47	σ_3	328.33	σ_1	0.195
5.	2	65.46	σ_2	341.45	$\sigma_3 + 90$	0.3977
6.	4	65.87	σ_2	88.77	σ_1	0.6479
7.	3	66.41	σ_3	83.76	σ_1	0.5996
8.	3	46.14	σ_1	167.94	σ_2	0.816
9.	3	51.4	σ_3	186.36	σ_1	0.9242
10.	2	63.14	σ_3	155.43	σ_1	0.433
11.	3	61.35	σ_2	318.16	σ_1	0.7477
12.	5	58.33	σ_3	50.19	σ_1	0.6845
13.	3	45.54	σ_2	70,36	σ_1	0.6607
14.	4	72.21	σ_2	319,54	$\sigma_3 + 90$	0.7988
15.	3	78.59	σ_3	350,12	σ_1	0.728
16.	3	73.87	σ_3	4,98	σ_1	0.5269
17.	3	83.54	σ_3	240,5	σ_1	0.3313
18.	2	64.18	σ_3	93,87	σ_1	0.6572
19.	2	43.92	σ_1	228,43	$\sigma_3 + 90$	0.3325
20.	2	48.16	σ_1	302,46	$\sigma_3 + 90$	0.6547
21.	3	73.89	σ_3	47,42	σ_1	0.1968
22.	3	50.17	σ_3	219,21	σ_1	0.335
23.	2	63.41	σ_3	70,22	σ_1	0.3363
24.	2	76.02	σ_3	281,33	σ_1	0.6185
25.	1	56.04	σ_3	325,36	σ_1	0.6008
26.	3	40.38	σ_1	206,96	$\sigma_3 + 90$	0.8026
27.	4	44.94	σ_3	16,44	σ_1	0.3358
28.	2	60.01	σ_3	169,63	σ_1	0.4579

In *Figure 12*, the results of three groups are presented: the 5th, 7th and 19th, respectively. The 7th group has similar results to the previous studies (the stereogram indicates thrust faults). The 19th group has rather special results. It seems reliable and accurate but it disagrees with the known studies. Here, the σ_1-axes has the largest plunge and the maximum horizontal direction was determined by the σ_3 axes (shown in *Table 3*). In the case of the 5th group, the calculations yielded a very poor outcome.

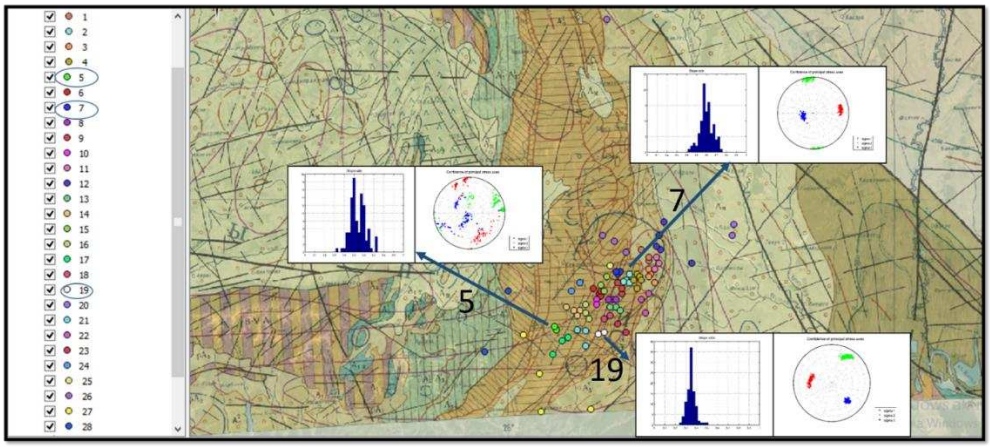

Figure 12. *R histograms and stereograms of the 5th, 7th and 19th groups*

DISCUSSION

After carrying out stress inversions, the stress relations were characterised by stress tensors. The authors used [17] and [18] for the determination of maximum horizontal stress orientations (S_H) and dominant tectonic regimes.

Figures 13–15 (the manual method, the k-means algorithm and the automatic clustering, respectively) illustrate the determined stress orientations and tectonic regimes based on the results. The maps were generated using Quantum GIS.

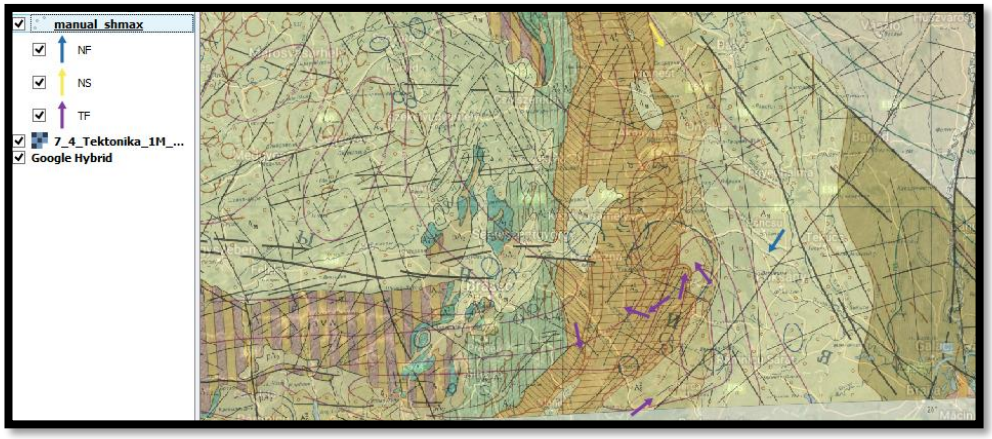

Figure 13. *The interpreted maximum horizontal stress orientations based on the azimuth of S_H and dominant tectonic regimes in the case of manual clustering. The different regimes are indicated by different colours (blue – normal faults, yellow – transtensions, purple – thrust faults)*

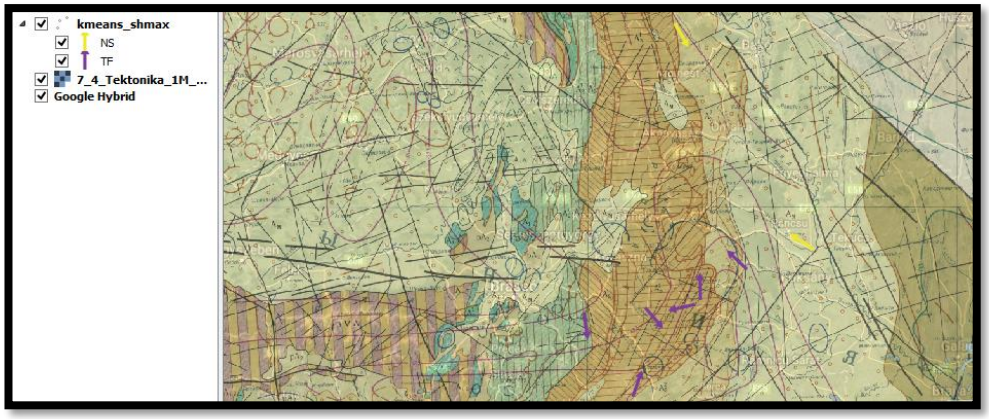

Figure 14. *The interpreted maximum horizontal stress orientations based on the azimuth of S_H and dominant tectonic regimes in the case of groups created by k-means algorithm. The different regimes are indicated by different colours (yellow – transtensions, purple – thrust faults)*

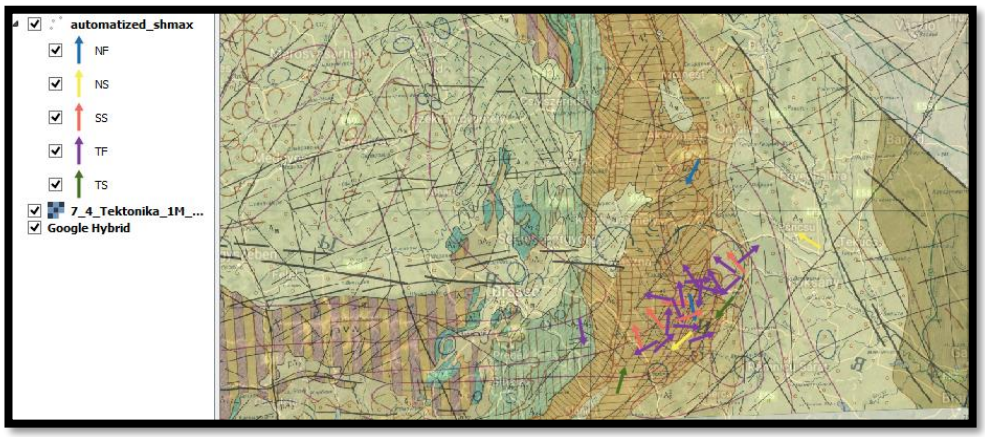

Figure 15. *The interpreted maximum horizontal stress orientations based on the azimuth of S_H and dominant tectonic regimes in the case of clusters created by the automated closest neighbour-based approach. The different regimes are indicated different colours (blue – normal faults, yellow – transtension, purple – thrust faults)*

It is visible in the comprehensive maps that the main tectonic structures are thrust faults and that stress orientations are variable. These pieces of information are similar to those obtained in previous studies and verify the complexity of the Vrancea Zone's tectonics.

However, it is necessary to take into account the difference among the clustering methods in the interpretation. While 8 subareas were created when using manual and

k-means clustering, the automated, nearest neighbour-based method generated 28 clusters. These clusters have a maximum of only 5-6 events, while the k-means and manual methods produced 15 events per cluster on average. Nevertheless, all grouping methods were able to create very small clusters (e.g. *Figure 9*, the 1st class of manual method or *Figure 10*, the 7th of k-means algorithm). Where there is a low amount of available data, results were generally less reliable than in larger subareas.

CONCLUSIONS

Based on this study, it seems to be apparent that the sets of epicentres generated by the manual and k-means method provided more reliable results for the evaluation of stress relations in the exterior SE Carpathians. The authors have begun developing an automatic method that is based on the principle of nearest neighbours. This initial version probably created too many sets for stress inversion. Thus, the next step will be to create an automatic clustering method more similar to the classical hierarchical method [19] but more suitable for taking into account the various types of different parameters (such as stress-field homogeneity) potentially relevant to stress-field estimations.

List of symbols

Symbol	Description	Unit
R	the shape ratio	–
R′	derived from shape ratio	–
σ_{11}, σ_1	the greatest principal stress axis (PSA)	°
σ_{22}, σ_2	the second greatest PSA	°
σ_{33}, σ_3	the smallest PSA	°
σ_V	the vertical principal stress	°
S_{Hmax}	maximum horizontal directions	–
M_w	momentum magnitude	–
$M__$	local magnitude	–

ACKNOWLEDGMENTS

This publication was created within the framework of ÚNKP-18-3 New National Excellence Program of the Ministry of Human Capacities, Hungary. Moreover, the authors would like to thank dr. Gribovszki Katalin (MTA CSFK Geodetic and Geophysical Institute) and dr. Norbert Péter Szabó for their help and support for this work.

REFERENCES

[1] Harangi, S., Novák, A., Kiss, B., Seghedi, I., Lukács, R., Szarka, L., Wesztergom, V., Metwaly, M., Gribovszki, K. (2015). Combined magnetotelluric and petrologic constrains for the nature of the magma storage system beneath the Late Pleistocene Ciomadul volcano (SE Carpathians). *Journal of Volcanology and Geothermal Research*, 290, pp. 82–96.

[2] Ismail-Zadeh, A., Matenco, L., Radulian, M., Cloetingh, S., Panza, G. (2012). Geodynamics and intermediate-depth seismicity in Vrancea (the south-eastern Carpathians): Current state-of-the art. *Tectonophysics*, 530, pp. 50–79.

[3] Martínez-Garzón, P., Ben-Zion, Y., Abolfathian, N., Kwiatek, G. & Bohnhoff, M. (2016). A refined methodology for stress inversions of earthquake focal mechanisms. *J. Geophys. Res. Solid Earth*, 121, pp. 8666–8687, doi:10.1002/2016JB013493.

[4] Hardebeck, J. L., Michael, A. J. (2006). Damped regional-scale stress inversions: Methodology and examples for southern California and the Coalinga aftershock sequence. *Journal of Geophysical Research*, Vol. 111, B11310, doi: 10.1029/2005JB004144

[5] Vavrycuk, V. (2014). Iterative joint inversion for stress and fault orientations from focal mechanisms. *Geophys. J. Int.*, 199, 69–77.

[6] Martínez-Garzón, P., Kwiatek, G., Ickrath M. & Bohnhoff, M. (2014). MSATSI: A MATLAB Package for Stress Inversion Combining Solid Classic Methodology, a New Simplified User-Handling, and a Visualization Tool. *Seismological Research Letters*, 85 (4), pp. 896–904.

[7] Moment Tensors by FMNEAR: http://fmnear.infp.ro/

[8] Moment Tensors by ISOLA-GUI: http://mt.infp.ro/

[9] National Institute of Geophysics and Volcanology (INGV): http://rcmt2.bo.ingv.it/

[10] Incorporated Research Institutions for Seismology (IRIS): https://ds.iris.edu/spud/momenttensor

[11] Meželovskij, N. V., Conseil d'assistance économique mutuelle (1987). *Space tectonic of map european countries – the CMEA members and SFRY/Council for Mutual Economic Assistance.* Echelle 1:1 000 000 (E 8°–E 30° /N 54°–N 42°), [Moskva]: Mingeo, Fédération de Russie.

[12] Shuttle Radar Topography Mission: http://srtm.csi.cgiar.org/

[13] Csanády, V., Horváth-Szováti, E. & Szalay, L. (2013). *Applied statistics.* (In Hungarian), pp. 162–172, Publishing of the University of West Hungary.

[14] Hartigan, J. A. (1975). *Clustering algorithms*.

[15] Hartigan, J. A. & Wong, M. A. (1979). Algorithm AS 136: A k-means clustering algorithm. *Journal of the Royal Statistical Society.* Series C (Applied Statistics), 28 (1), pp. 100–108.

[16] Cesca, S., Sen, A. T. & Dahm, T. (2014). Seismicity monitoring by cluster analysis of moment tensors. *Geophysical Journal International*, Vol. 196, pp. 1813–1826.

[17] Zoback, M. L. (1992). First-and second-order patterns of stress in the lithosphere: The world stress map project. *Journal of Geophysical Research: Solid Earth*, 97 (B8), pp. 11703–11728.

[18] Barth, A., Reinecker, J. & Heidbach, O. (2008). *Stress derivation from earthquake focal mechanisms*. World Stress Map Project.

[19] Murtagh, F. (1983). A Survey of Recent Advances in Hierarchical Clustering Algorithms. *The Computer Journal*, Vol. 26 (4), pp. 354–359.

Geosciences and Engineering, Vol. 6, No. 9 (2018), pp. 151–162.

GLOBAL JOINT INVERSION OF ACOUSTIC VELOCITY AND QUALITY FACTOR DATA USING ROCK PHYSICAL MODELS

JUDIT SOMOGYINÉ MOLNÁR[1, 2]–ANETT KISS[1, 3]–
TÜNDE EDIT DOBRÓKA[4]

[1]*MTA-ME Geoengineering Research Group, University of Miskolc*
gfmj@uni-miskolc.hu
[2]*Institute of Electrical and Electronic Engineering, University of Miskolc*
[3]*Department of Geophysics, University of Miskolc*
[4]*Research Institute of Applied Earth Science, University of Miskolc*

Abstract: In this study, we apply new rock physical models to describe the pressure dependence of seismic/acoustic velocity and quality factor data. The models are based on the previously discussed idea that microcracks in rocks are opened and closed with changes in pressure. Using the model equations as forward modeling formulae, a global optimization algorithm (Simulated Annealing) was applied to solve the joint inversion problem and to determine the petrophysical parameters of the models.

Keywords: *petrophysical model, longitudinal wave velocity, quality factor, pressure, joint inversion, Simulated Annealing*

INTRODUCTION

As a result of the increasing world market price of hydrocarbons, the utilization of non-conventional hydrocarbon resources and the associated research has become very intensive. This type of hydrocarbon occurrences can also be found in Hungary. The knowledge of petrophysical parameters (porosity, permeability) in typically pressurized, deep-seated and high-temperature reservoirs is very important. These non-conventional reservoirs have very low porosity and permeability. Thus it is expedient to create a reservoir geological model in which the petroacoustic characteristics (mostly the propagation velocity of the elastic wave and quality factor) and their pressure dependence play an important role because they have a direct connection to the porosity.

The propagation characteristics of acoustic waves contain information on important mechanical properties of rocks. Therefore the determination of velocity and attenuation of the seismic/acoustic wave is relevant in studying rock parameters, both in the laboratory and in-situ conditions. The velocity of acoustic waves propagating in different rocks under various confining pressures [1–3] and also under different pore pressures [4–7] have been investigated over several decades and by many researchers. The phenomenon in which the wave velocity increases with increasing pressure is well-known and has been discussed in several rock physical

studies. One of the most frequently used mechanisms for explaining the phenomenon is based on the closure of microcracks in rocks under pressure [8–11]. Singh et al. created an empirical model for pressure-dependent wave velocity after observing measured P and S wave propagation velocities for several sandstone samples [12]. Prasad inferred the situation of gas-saturated and pressurized zones from the ratio of propagation velocities of P and S waves [13].

The attenuation of the acoustic wave decreases with increasing pressure, which can also be explained by the presence of microcracks in rocks [5, 14–15]. Toksöz et al. measured P and S wave velocities under pressure on dry samples, water, brine, or methane-saturated samples, and frozen samples and studied their attenuations [16]. It was found that the attenuation was higher for water-saturated and brine-saturated samples compared to methane-saturated or dry samples and the attenuation decreased with increasing pressure. The reason for this phenomenon can be the closure of microcracks according to Yu et al. [5], Best [10], and Johnston et al. [17].

Based on petrophysical models and experimental results, it is possible to infer the extent of emerging tensions in rocks, and perhaps even its dependence of direction, by means of measured longitudinal and transversal wave velocity data. Several petrophysical models are known in literature, e.g., the Biot model [18–19], Gassmann model [20], Contact radius model (CRM) [21], Friction model (FM) [22–23], etc. The Biot model describes wave propagation in a two-phase system, a porous elastic frame, and a viscous, incompressible pore fluid. The attenuation of the wave is ascribed to relative motion between the frame and its pore fluid. According to the Gassmann model, when the pore space of rock is saturated with fluid, there is a change in the apparent bulk modulus due to very small variations in pore pressure induced by the elastic wave. Thus in isotropic, porous rocks, the P wave velocity depends on the properties of the dry background and pore fluid as well as on porosity. CRM considers two elastic, homogeneous, identical spherical particles in contact. The radius of the area of contact between the spheres increases upon deformation due to a normal force. In the FM model, the frictional losses at shear strains are negligible in rock samples.

In this paper, we present a new approach for the description of the pressure dependence of phase velocity and the quality factor of acoustic waves propagating in a porous rock sample. Our considerations are based on the mechanism of closure of the microcracks in rocks under pressure.

THE PRESSURE DEPENDENT VELOCITY MODEL

Elastic wave velocity in rocks depends on many rock properties, such as the type of rock-forming minerals and cementing material (rock matrix), porosity, and pore-filling fluid, as well as microcracking. Following Walsh and Brace's idea [24], we assume that the main factor determining the stress dependence of the wave propagation velocity is the closure of the microcracks. In our considerations, we restrict ourselves only to the uniaxial stress state and longitudinal acoustic waves propagat-

ing along the direction of load. We assume further that only the projection of the area of the microcrack perpendicular to the load direction has an influence on the change in the propagation characteristics. For this reason, we introduce the concept of the effective area $A_\perp$ as the sum of the areas of the open individual microcracks projected to a plane perpendicular to the direction of the uniaxial load.

If we create a dσ stress increase in the rock, we find that $dA_\perp$ (the change in the effective area of the open microcracks) is directly proportional to the applied dσ stress increase. At the same time $dA_\perp$ is directly proportional to $A_\perp$, which is the total effective area of the open microcracks. We can unify both assumptions in the following differential equation as

$$dA_\perp = -\lambda A_\perp \, d\sigma , \tag{1}$$

where λ is a proportionality factor (material dependent rock physical parameter). In *Equation (1)* the negative sign represents the fact that with increasing stress – with closing microcracks – the total effective area of the open microcracks decreases. The solution of the equation is

$$A_\perp = A_\perp^{(0)} \exp(-\lambda\sigma) , \tag{2}$$

where $A_\perp^{(0)}$ is the total effective area of the open microcracks in a stress-free state (σ = 0). Another assumption is the linear relationship between the longitudinal wave velocity change dv and the change in the effective area $dA_\perp$

$$dv = -\alpha \, dA_\perp , \tag{3}$$

where α is a proportionality factor (a material quality dependent constant). The negative sign represents the fact that the velocity increases with decreasing effective area of the open microcracks. Combining *Equation (3)* with *Equation (1)* and *Equation (2)* one can obtain

$$dv = \alpha\lambda A_\perp^{(0)} \exp(-\lambda\sigma) \, d\sigma . \tag{4}$$

After integrating *Equation (4)* we have

$$v = K - \alpha A_\perp^{(0)} \exp(-\lambda\sigma) . \tag{5}$$

In a stress-free state (σ = 0) the propagation velocity v_0 can be measured, which can be computed from *Equation (5)* as $v_0 = K - \alpha A_\perp^{(0)}$. From here we get the integration constant $K = v_0 + \alpha A_\perp^{(0)}$. With this result and the introduction of $\Delta v = \alpha A_\perp^{(0)}$, *Equation (5)* can be rewritten in the following form

$$v = v_0 + \Delta v \, (1 - \exp(-\lambda\sigma)) , \tag{6}$$

where $\lambda=1/\sigma^*$ and σ^* is that stress value at which the velocity (starting from v_0) approximates the value v_{max} with 1/e accuracy.

Equation (6) provides a theoretical connection between the longitudinal wave velocity and rock pressure. It contains three model parameters (v_0, Δv, λ) which are to be determined by using the stress-dependent velocity data measured on the investigated rock sample. *Equation (6)* shows that the propagation velocity – as a function of stress – starts from v_0 and increases up to the value $v_{max} = v_0 + \Delta v$ according to the function $1\text{-}exp(\lambda\sigma)$. Consequently, the velocity reaches its limit v_{max} at high stress values. The value $\Delta v = v_{max}–v_0$ is a velocity range in which the propagation velocity can vary from the stress-free state up to the state characterized by high rock pressure. (Certainly, it is only valid in the framework of the model assumptions because in the range of high stresses new microcracks can open in the rock. It should be mentioned that the description of the latter was not a goal in our approach.)

THE PRESSURE DEPENDENT QUALITY FACTOR MODEL

The effect of microcracks for the quality factor – like in the case of propagation velocity – can be studied based on qualitative considerations without detailed analysis of the structure and the physical mechanisms. It is obvious that the $dA_\perp$ change in the effective area of the open microcracks leads to a dQ change in the quality factor of the longitudinal wave. We assume again a linear relationship between them and write

$$dQ = -\beta dA_\perp, \tag{7}$$

where β is another proportionality factor (a material quality dependent constant). The negative sign represents the fact that the quality factor increases with closing microcracks (thus decreasing the effective area of the open microcracks). Combining *Equation (7)* with *Equation (1)* and *Equation (2)* the following equation can be obtained

$$dQ = \beta\lambda A_\perp^{(0)} \exp(-\lambda\sigma)d\sigma\,. \tag{8}$$

Solving *Equation (8)* and introducing the notation $\Delta Q = \beta A_\perp^{(0)}$, one can get the following model equation, which is similar to *Equation (6)*,

$$Q = Q_o + \Delta Q\big(1-\exp(-\lambda\sigma)\big), \tag{9}$$

where Q_0 is the quality factor in a stress-free state ($\sigma = 0$) and λ is the common proportionality factor (material characteristic) in the two model equations *[Equations (6)* and *(9)]*. It is well-known that there can be several reasons for absorption. With *Equation (9)* we describe the attenuation caused by only the change in the effective area of the open microcracks. *Equation (9)* contains three model parameters (Q_0, ΔQ, λ) that can be determined by using the stress-dependent quality factor data measured on the investigated rock sample.

THE GLOBAL INVERSION METHOD MSA

The established petrophysical models *[Equations (6)* and *(9)]* create the possibility to calculate the propagation velocity and quality factor at any pressure based on known parameters (v_0, Δv, Q_0, ΔQ, λ) of rock (this is the so-called forward problem). In contrary, the parameters appearing in the above model equations can be derived from the observed data by using a geophysical (joint) inversion method [25]. In the joint inversion procedure, we give an estimate for the velocity and quality factor data in a single algorithm, where λ is the common petrophysical parameter connecting the two data sets in this case. So we integrate the measurement data into the combined data vector

$$\mathbf{d}^{obs} = \{v_1^{obs},...,v_{N_v}^{obs}, Q_1^{obs},...,Q_{N_Q}^{obs}\}, \tag{10}$$

where N_v and N_Q are the numbers of the measured velocity and quality factor data, respectively. Introducing the combined vector **m** of model parameters as

$$\mathbf{m} = (v_0, \Delta v, Q_0, \Delta Q, \lambda) \tag{11}$$

we can write the (joint) response function in the form

$$\mathbf{d}^{calc} = \mathbf{g}(\mathbf{m}), \tag{12}$$

where

$$\mathbf{d}^{calc} = \{v_1^{calc},...,v_{Nv}^{calc}, Q_1^{calc},...,Q_{N_Q}^{calc}\} \tag{13}$$

with

$$d_k^{calc} = g_k(\mathbf{m}) = \begin{Bmatrix} v^{calc}(\mathbf{m}_v, \sigma_k), \; k = 1,...,N_v \\ Q^{calc}(\mathbf{m}_Q, \sigma_k), \; k = N_v + 1,...,N_v + N_Q \end{Bmatrix} \tag{14}$$

and

$$\mathbf{m}_v = (v_0, \Delta v, \lambda), \quad \mathbf{m}_Q = (Q_0, \Delta Q, \lambda). \tag{15}$$

In the inversion procedure, the parameter vector **m** is determined usually by means of minimizing the weighted norm

$$E = (\mathbf{e}, \mathbf{W}\,\mathbf{e}) \tag{16}$$

of the

$$\mathbf{e} = \mathbf{d}^{obs} - \mathbf{d}^{calc} \tag{17}$$

deviation vector (the W_{kk} weights are usually given a priori).

As the forward modeling formula *Equation (12)* is nonlinear, linearization is often used. It is well-known that linearized inversion procedures can trap in a local minimum

of the *Equation (16)* function. To ensure finding the absolute (global) minimum, the methods of global optimization are to be used. In this paper, the Metropolis algorithm (a member of the family of Simulated Annealing procedures, abbreviated as MSA) [26–27] is used. In this method, an adequate objective function is required, which is minimized during the optimization procedure. In most cases, it is based on the L2-norm (or its weighted version in *Equation 16*) of the difference between the measured and calculated data (called Energy in the terminology of MSA). The SA methods are based on the random modification of the elements of the model vector in an iteration procedure. The modification of the *j*-th parameter can be written as

$$m_j^{new} = m_j^{old} + b_j^{\max} \varepsilon \,, \tag{18}$$

where ε is a uniformly distributed random number in the interval (0, 1) and $b_j^{\max}$ is an appropriately chosen limit of change in the *j*-th variable. During the random search, the energy function is calculated and compared with the previous one and the ΔE energy change is generated in every iteration steps. The acceptance probability of the new model depends on the Metropolis criteria

$$P(\Delta E, T) = \begin{Bmatrix} 1 & ,if\ \Delta E \le 0 \\ \exp\left(-\dfrac{\Delta E}{T}\right), & otherwise \end{Bmatrix}, \tag{19}$$

where the new model is always accepted when the value of the energy function is lower in the new state than in the previous one $\Delta E \le 0$. If the energy of the new model increases, there is also some probability of acceptance depending on the values of the energy function and control temperature T. The MSA method can be described by a simple and clear-cut scheme. The pseudo FORTRAN code is given by Sen and Stoffa [28]:

Start at a random location $\vec{m}_o$ with energy $E(\vec{m}_o)$ (20)

loop over temperature (T)

loop over the number of random moves/temperature

$$\Delta E = E(\vec{m}_1) - E(\vec{m}_o)$$

$$P = \exp\left(-\frac{\Delta E}{T}\right)$$

if $\Delta E \le 0$ then

$$\vec{m}_o = \vec{m}_1$$

$$E(\vec{m}_o) = E(\vec{m}_1)$$

end if

if $\Delta E \ge 0$ then

draw a random number $\alpha = U[0,1]$
if $P \geq \alpha$ then
$\vec{m}_o = \vec{m}_1$
$E(\vec{m}_o) = E(\vec{m}_1)$
end if
end if
end loop
end loop

This is repeated in an iterative procedure until a proper stop criterion is met. For our numerical calculations, this scheme was implemented in MATLAB code.

RESULTS AND DISCUSSION

In order to prove the validity and practical applicability of our rock physical model, the velocity and quality factor data measured by Prasad and Manghnani on a Berea sandstone rock sample were processed [29]. Since the data set contained relatively low noise we used **W = I** in *Equation (16)*, (where **I** is the unit matrix).

For the characterization of the accuracy, we calculated the measure of a fitting according to the data misfit formula

$$D = \sqrt{\frac{1}{N}\sum_{k=1}^{N}\left(\frac{d_k^{(obs)} - d_k^{(calc)}}{d_k^{(calc)}}\right)^2} \quad , \tag{21}$$

where $d_k^{(calc)}$ and $d_k^{(obs)}$ are the calculated and observed (measured) velocity/quality factor data at the *k*-th pressure value, while N is the number of measured points. As a starting value T_0 of the control parameter, we used the D distance calculated between the measured and the calculated (on the randomly selected) start model. The control parameter was reduced by 0.1% in each iteration. The MSA inversion results can be seen in *Table 1*.

Table 1

Estimated model parameters (using the MSA method) for Berea sandstone sample

Sample	**v_0 (km/s)**	**Q_0 (–)**	**Δv (km/s)**	**ΔQ (–)**	**λ (1/MPa)**
Berea sandstone	3.684	16.4	0.925	55.0	0.0932

With these parameters, the velocity and quality factor data can be calculated at any pressure by substituting them into *Equation (6)* and *Equation (9)*. The results are shown in *Figure 1*. The continuous lines show the calculated velocity–pressure and quality factor-pressure functions while symbols represent the measured data.

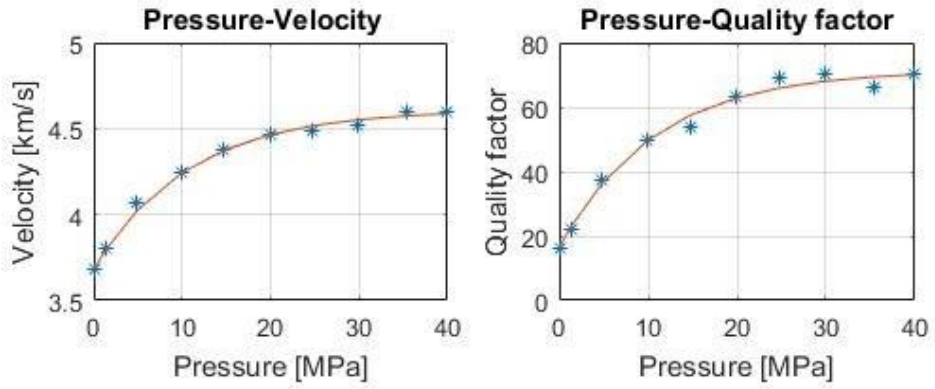

Figure 1. *The fit between the observed and calculated (with estimated model parameters) data using the global (MSA) joint inversion method*

The figure shows that the calculated functions are in good accordance with the measured data, which proves that the petrophysical models suggested in *Equations (6)* and *(9)* apply well in practice. This is proved also by the data misfit value, which is D = 0.025 in our case.

CONCLUSIONS

We presented new petrophysical models for describing the connection between the propagation velocity of the acoustic wave and rock pressure as well as the quality factor and pressure. The models are based on the idea that microcracks are opened and closed as pressure changes. Within the confines of the models, differential equations were set up and solved describing the phenomenon of pressure dependence. It was found that the quality factor and the seismic velocity increases with increasing pressure.

The models were applied to acoustic velocity and quality factor data measured on a core sample. By means of global inversion-based processing (Metropolis Simulated Annealing), the model parameters were determined from measurement data. The described inverse problem was significantly overdetermined. Therefore, the inversion procedure was stable and could be handled properly by the global MSA inversion technique. The calculated data matched accurately with measured data, proving that the petrophysical model applies well in practice. Inversion results confirmed the accuracy and feasibility of our petrophysical models.

ACKNOWLEDGMENTS

On behalf of Judit Somogyiné Molnár, the described article was carried out as part of the EFOP-3.6.1-16-2016-00011 *Younger and Renewing University –Innovative Knowledge City – institutional development of the University of Miskolc aiming at intelligent specialization* project implemented in the framework of the Széchenyi 2020 program.

The realization of the project in case of Tünde Edit Dobróka is supported by the European Union, co-financed by the European Social Fund. This research was supported by the GINOP-2.3.2-15-2016-00010 *Development of enhanced engineering methods with the aim at utilization of subterranean energy resources* project in the framework of the Széchenyi 2020 Plan, funded by the European Union, co-financed by the European Structural and Investment Funds.

LIST OF SYMBOLS

Symbol	Description	Unit
$A_{\perp}$	total effective area of the open microcracks projected to a plane perpendicular to the direction of the uniaxial load	m^2
$A_{\perp}^{(0)}$	total effective area of the open microcracks in a stress-free state	m^2
b_j^{max}	limit of change in the *j*-th variable	–
D	data misfit	%
$dA_{\perp}$	the change in the effective area of the open microcracks	m^2
d^{calc}	calculated data vector	–
$d_k^{(calc)}$	calculated velocity/quality factor at the *k*-th pressure value	m/s
d^{obs}	observed (measured) data vector	–
$d_k^{(obs)}$	observed (measured) velocity/quality factor at the *k*-th pressure value	m/s
dQ	the change in the quality factor of the longitudinal wave	–
dv	change of propagation wave velocity	m/s
dσ	stress increase	MPa
e	deviation vector	–
E	weighted norm	–
g	response function	–
I	unit matrix	–
K	integration constant	–
m	model parameter vector	–
m_0	start model parameter vector	–
m_j^{new}	*j*-th new model parameter vector	–
m_j^{old}	*j*-th old model parameter vector	–
m_Q	model parameter vector of quality factor model equation	–
m_v	model parameter vector of velocity model equation	–
N	number of measured points	–
N_Q	number of the measured quality factor data	–
N_v	number of the measured velocity data	–

Symbol	Description	Unit
Q	quality factor of the longitudinal wave	–
Q_0	quality factor of the longitudinal wave at stress-free state	–
Q^{calc}	calculated quality factor data of the longitudinal wave	–
Q^{obs}	observed (measured) quality factor data of the longitudinal wave	–
T	temperature	°C
T_0	start temperature	°C
v	longitudinal wave velocity	m/s
v_0	longitudinal wave velocity at stress-free state	m/s
v^{calc}	calculated longitudinal wave velocity data	m/s
v_{max}	longitudinal wave velocity at maximum pressure	m/s
v^{obs}	observed (measured) velocity data	m/s
W	weight	–
α	proportionality factor	1/(m s)
β	proportionality factor	1/ m^2
ΔE	energy change	°C
ΔQ	quality factor range of the longitudinal wave	–
Δv	velocity range	m/s
ε	random number in the interval (0,1)	–
λ	material dependent rock physical parameter	1/MPa
σ	stress	MPa
σ^*	maximum stress	MPa

REFERENCES

[1] Wyllie, M. R. J., Gregory, A. R., Gardner, G. H. F. (1958). An experimental investigation of factors affecting elastic wave velocities in porous media. *Geophysics*, 23 (3), pp. 459–493.

[2] Stacey, T. R. (1977). Seismic assessment of rock masses. *Symposium on Exploration for Rock Engineering*, Johannesburg, 2, pp. 113–117.

[3] King, M. S. (2009). Recent developments in seismic rock physics. *International Journal of Rock Mechanics and Mining Science*, 46, pp. 1341–1348.

[4] Nur, A., Simmons, G. (1969). The effect of saturation on velocity in low porosity rocks. *Earth and Planetary Science Letters*, 7, pp. 183–193.

[5] Yu, G., Vozoff, K., Durney, D. W. (1993). The influence of confining pressure and water saturation on dynamic elastic properties of some Permian coals. *Geophysics*, 58 (1), pp. 30–38.

[6] Darot, M., Reuschlé, T. (2000). Acoustic wave velocity and permeability evolution during pressure cycles on a thermally cracked granite. *International Journal of Rock Mechanics and Mining Science*, 37, pp. 1019–1026.

[7] He, T., Schmitt, D. R. (2006). Velocity measurements of conglomerates and pressure sensitivity analysis of AVA response. *Proceedings of the 76th SEG International Exposition and Annual Meeting*, New Orleans, USA, Oct 1–6, 2006.

[8] Holt, R. M., Furre, A. K., Horsrud, P. (1997). Stress-dependent wave velocities in sedimentary rock cores: why and why not? *International Journal of Rock Mechanics and Mining Science*, 34, pp. 3–4.

[9] Sengun, N., Altindag, R., Demirdag, S., Yavuz, H. (2011). P-wave velocity and Schmidt rebound hardness value of rocks under uniaxial compressional loading. *International Journal of Rock Mechanics and Mining Science*, 48, pp. 693–696.

[10] Best, A. I. (1997). The effect of pressure on ultrasonic velocity and attenuation in near-surface sedimentary rocks. *Geophysical Prospecting*, 45, pp. 345–364.

[11] Hassan, A., Vega, S. (2009). A study of seismic velocities and differential pressure dependence in a Middle East carbonate reservoir. *Proceedings of the 79th SEG International Exposition and Annual Meeting*, Houston, USA, Oct. 25–30, 2009.

[12] Singh, R., Rai, C., Sondergeld, C. (2006). *Pressure dependence of elastic wave velocities in sandstones. 76th International Exposition and Annual Meeting*, SEG, pp. 1883–1887.

[13] Prasad, M. (2002). Acoustic measurements in unconsolidated sands at a low effective pressure and overpressure detection. *Geophysics*, 67 (2), pp. 405–412.

[14] Lucet, N., Zinszner, B. (1992). Effects of heterogeneities and anisotropy on sonic and ultrasonic attenuation in rocks. *Geophysics*, 57 (8), pp. 1018–1026.

[15] Carcione, J. M., Helbig, K., Helle, H. B. (2003). Effects of pressure and saturating fluid on wave velocity and attenuation in anisotropic rocks. *International Journal of Rock Mechanics and Mining Science*, 40, pp. 89–403.

[16] Toksöz, M. N., Johnston, D. H., Timur, A. (1979). Attenuation of seismic waves in dry and saturated rocks, I. Laboratory measurements. *Geophysics*, 44 (4), pp. 681–690.

[17] Johnston, D. H., Toksöz, M. N., Timur, A. (1979). Attenuation of seismic waves in dry and saturated rocks, II. Mechanism. *Geophysics*, 44 (4), pp. 691–711.

[18] Biot, M. A. (1956a). Theory of propagation of elastic waves in fluid-saturated porous solids, I: Low-frequency range. *Journal of the Acoustical Society of America*, 28, pp. 168–178.

[19] Biot, M. A. (1956b). Theory of propagation of elastic waves in fluid-saturated porous solids, II: High-frequency range. *Journal of the Acoustical Society of America*, 28, pp. 179–191.

[20] Gassmann, F. (1951). Über die Elastizitat poröser Medien. *Vierteljahrsschrift der Naturforschenden Gesellschaft in Zürich*, 96, pp. 1–23.

[21] Duffy, J., Mindlin, R. D. (1957). Stress-strain relations and vibrations of a granular medium. *Journal of Applied Mechanics*, 24, pp. 585–593.

[22] Winkler, K. W., Nur, A. (1982). Seismic attenuation: effects of pore fluid and frictional sliding. *Geophysics*, 47, pp. 1–15.

[23] Stewart, R. D., Toksöz, M. N., Timur, A. (1983). Strain dependant attenuation observations and a proposed mechanism. *Journal of Geophysical Research*, 88, pp. 546–554.

[24] Walsh, J. B., Brace, W. F. (1964). A fracture criterion for brittle anisotropic rock. *Journal of Geophysical Research*, 69, pp. 3449–3456.

[25] Dobróka, M., Gyulai, Á., Ormos, T., Csókás, J., Dresen, L. (1991). Joint inversion of seismic and geoelectric data recorded in an underground coal-mine. *Geophysical Prospecting*, 39, pp. 643–665.

[26] Scales, J. A., Gerztenkorn, A., Treitel, S., Lines, L. R. (1988). Robust optimization methods in geophysical inverse theory. *Proceedings of the 58th SEG International Annual Meeting*, Anaheim, USA, Oct. 11–15, 1988, pp. 827–830.

[27] Steiner, F. (1997). *Optimum Methods in Statistics*. Budapest: Academic Press.

[28] Sen, M. K., Stoffa, P. L. (1997). *Global Optimization Methods in Geophysical Inversion*. Cambridge University Press; 2nd edition.

[29] Prasad, M., Manghnani, M. H. (1997). Effects of pore and differential pressure on compressional wave velocity and quality factor in Berea and Michigan sandstones. *Geophysics*, 62 (4), pp. 1163–1176.

Geosciences and Engineering, Vol. 6, No. 9 (2018), pp. 163–175.

A LEAST SQUARES INVERSION PROCEDURE APPLIED TO PARAMETER ESTIMATION OF DYNAMIC ORDERING IN SUPERCONDUCTING VORTEX SYSTEMS

MIHÁLY MÁRTON DOBRÓKA

Department of Physics, Tokyo Institute of Technology
dobroka.mihaly@gmail.com

Abstract: Generally, in physics and technical sciences, the proximity of measured and estimated data is often required. To ensure an appropriate fit, the Gaussian Least Squares method is extensively used. In the present work, this methodology was applied to parameter estimation of dynamic ordering phenomenon observed in vortex system. The forward modeling formulae were given by using elementary statistical assumptions. The inversion algorithm was proven to be accurate by means of the low level of parameter correlation and the highly acceptable fitting between the measured and calculated data.

Keywords: *superconductivity, physics of vortices, random ordering, least squares inversion*

INTRODUCTION

When a correlated many-particle system with random initial distribution is periodically sheared and the number of shear cycles is increased, the particles gradually self-organize to avoid future collisions and transform into an organized configuration. This is called dynamic ordering or random organization. This general phenomenon has been widely observed – experimentally as well as numerically – in various systems, such as colloidal suspensions [1, 2], superconducting vortices [3, 4], and amorphous solids [5].

Figure 1 schematically illustrates this process. Initially, we have colloidal particles with random initial distribution. Then the system is externally sheared by a shear amplitude γ and moved back. The definition of γ is shown in the figure. *Figure 1(a)* schematically illustrates a particle collision during a shear cycle. When the system is sheared the collided particles are given a small displacement in random direction; thus, they do not return to their initial position. *Figure 1(b)* shows the evolution of the particle configuration for shear amplitude $\gamma = 2$. The black dots represent those particles that will collide in the next cycle. The open dots mark the particles that will return back to their original position. Since the initial configuration is random, many collisions occur during the first shear cycle. As the cycle number is increased, however, the number of collided particles decreases and they eventually cease to collide. During the collisions, all of the particles have found a position where they no longer collide with surrounding particles when the system is periodically driven.

In our investigation, we use a superconducting vortex system. The advantage of a vortex system is its easy controllability and excellent reproducibility. The individual vortices are regarded as perfectly uniform particles due to quantization. Their motion can be controlled by applying current. The mean velocity can be detected precisely measuring the voltage response induced by the vortex motion.

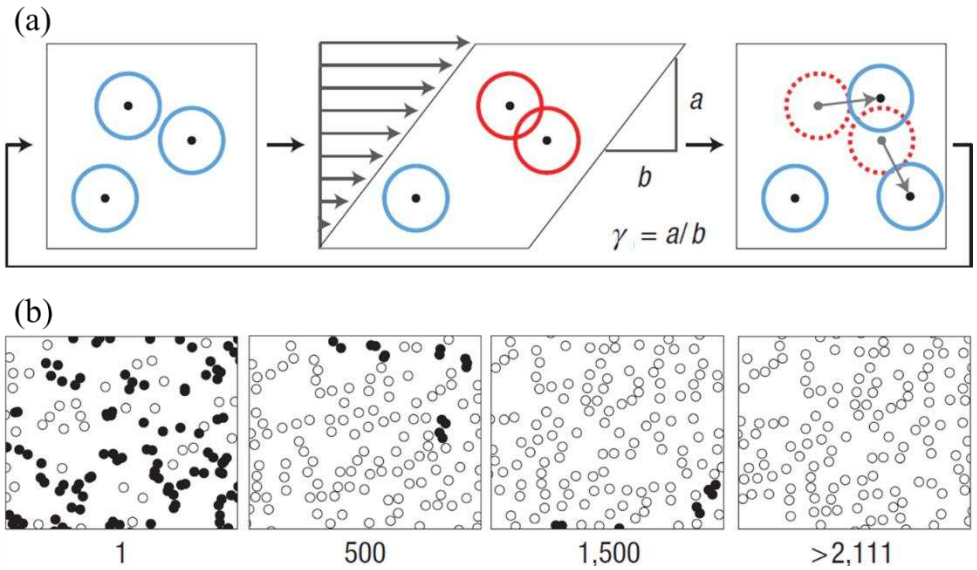

Figure 1. *(a) Schematic illustration of a particle collision during a shear cycle. When the system is sheared the collided particles are given a small displacement in a random direction and do not return to their initial position. (b) Evolution of the particle configuration for shear amplitude γ = 2 where the numbers below the snapshots show the shear cycle number. Black dots represent particles that will collide in the next cycle; open dots mark particles that will move back to their original position after the shear cycle.* [1]

VORTEX SYSTEM

In type-II superconductors, when the external magnetic field exceeds the value of the lower critical field, the magnetic field penetrates the material in the form of quantized flux called a vortex. In a vortex, supercurrent circulates around its normal, non-superconductive core. As the magnetic field is increased, the number and the density of vortices increase. Between the vortices a repulsive force exists. Thus, in clean superconductors, the vortices form a periodic triangular lattice known as an Abrikosov lattice *[Figure 2 (a)]*. However, in actual superconductors, there are impurities and defects of the material acting as pinning centers for the vortices. Since these places weaken the superconductivity, it is energetically favorable that vortices with a non-superconducting core occupy these places, resulting in an attractive force

between the pinning centers and vortices. Therefore, in the presence of the pinning, the vortex lattice becomes distorted. *[Figure 2 (b)]*.

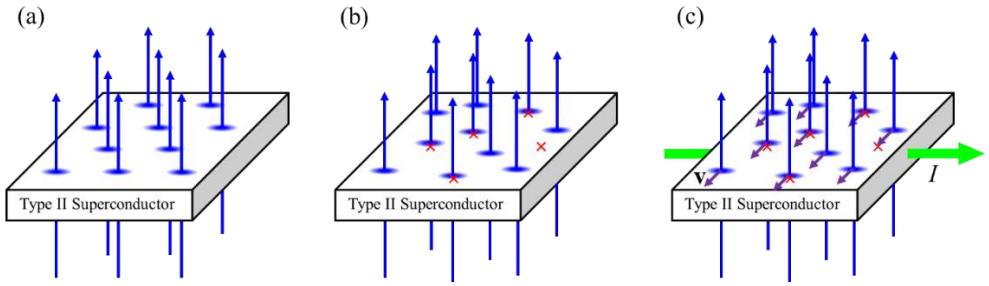

Figure 2. *Schematic illustration of vortices in type-II superconductors (a) absence of pinning (b) presence of random pinning (c) presence of random pinning and driving current. The blue dots and red crosses indicate the vortices and the pinning centers, respectively. The blue, green and purple arrows show the direction of the magnetic field, the current, and the driving force (parallel with the velocity), respectively. The voltage is generated in the direction of the applied current*

When an external current with a current density **J** is applied perpendicularly to the magnetic field, the Lorentz force per unit length that a single vortex is subjected to is expressed as

$$\mathbf{f} = \mathbf{J} \times \mathbf{\Phi_0}, \tag{1}$$

where **J** is the current density and $\mathbf{\Phi}_0$ is a vector with a magnitude of Φ_0 and with the direction along the vortex axis. The magnetic flux density is explained as

$$\mathbf{B} = n\,\mathbf{\Phi}_0, \tag{2}$$

where n is the number of vortices per unit area. Thus, the Lorentz force per unit area can be expressed as

$$\mathbf{F} = \mathbf{J} \times \mathbf{B}. \tag{3}$$

From *Equation (2)* it is evident that the vortices are driven in a direction perpendicular to both the applied current and the magnetic field (vortex axis). The electric field **E** generated by their motion due to the electromagnetic induction is expressed as

$$\mathbf{E} = \mathbf{B} \times \mathbf{v}, \tag{4}$$

where **v** is the velocity of a driven vortex. When a vortex is driven by the Lorentz force **F**, this electric field is parallel to the current. The voltage generated by the vortex motion is expressed as

$$V = vBl = vN\Phi_0 l, \tag{5}$$

where l is the distance between the voltage contacts and N is the total number of the vortices between them. The significance of *Equation (4)* is that the average vortex

velocity can be detected by measuring the voltage. Thus, we can derive the force-velocity relation from current-voltage characteristics experimentally. If the driving current of square waveform is periodic with frequency *f*, the distance covered by the vortex in a half time period *T/2 = 1/(2f)* is

$$d = v\frac{T}{2} = \frac{U}{2Blf}. \tag{6}$$

DYNAMIC ORDERING IN PERIODICALLY DRIVEN VORTEX SYSTEM

Andrei et al. investigated how vortices move when a small periodic drive is applied to the system [6]. They found that vortices can move easily in response to an AC current whose amplitude is below the DC depinning threshold I_c. *Figure 3* shows the transient voltage response when the drive is changed to AC and (at the end of the experiment) set back to DC while keeping the amplitude $I < I_c$. The voltage answer in response to the initial DC drive ($t < 2.5$ ms) is zero, consistent with the fact that the vortices are unable to move at $I < I_c$. However, voltage appears as soon as the drive is changed to the opposite direction. Under AC drive the amplitude of the voltage increases toward the steady-state value, indicating that it becomes easy for the vortices to move. This is called AC dynamic ordering. When the DC drive is set back, the voltage decays until it goes back to zero, indicating that it becomes difficult for the vortices to move. This is called DC dynamic disordering. It should be noted that the voltage also decays on each half pulse in the response to the AC drive (so during constant voltage dynamic disordering starts in the half pulse). Thus, AC dynamic ordering is referred to as an increase in the envelope curve of the amplitude.

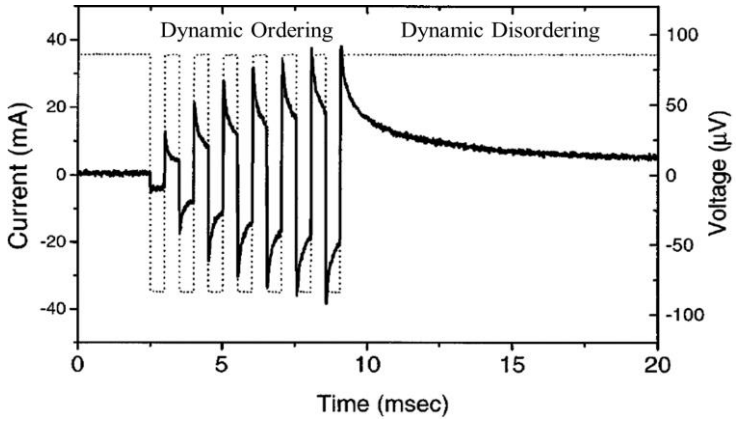

Figure 3. *The dotted line and full line show the driving current and the voltage response, respectively. In the experiment, at first DC current was applied for a few seconds. Later several cycles of AC current were applied and subsequently the DC current was applied again. The increase in the voltage amplitude in response to the AC drive indicates dynamic ordering while the decay of the voltage in response to the DC drive signifies the dynamic disordering of the system* [6]

THE FORWARD PROBLEM OF DYNAMIC ORDERING

The parameters characterizing the voltage response of the vortex system shown can be estimated by using the measured voltage data in the framework of inverse problem theory. To do this, we have to construct a model resulting in a forward modeling formula (response function). Using the basic physical rules and some elementary statistical considerations the voltage-time response function describing the dynamic ordering of the vortex system is given by *Equation (A6)* of the Appendix

$$U(t) = \left[U_0 + (U_\infty - U_0)\,(1 - \exp(-\lambda_1 t))\right] sygn(\sin(\omega t)) \tag{7}$$

as a response of AC squared waveform current. The function gives an increasing envelope curve of the amplitudes due to dynamic ordering.

As can be seen in *Figure 3*, in each new half period an opposite phenomenon starts with exponential decrease of the voltage. After some elementary investigations, the formula describing this effect together with the basic dynamic ordering phenomenon is derived in *Equation (A11)*:

$$U(t) = \left\{U_0 + (U_\infty - U_0)\,(1 - \exp(-\lambda_1 t_q))\exp(-\lambda_2 (t - t_q))\right\} sygn(\sin(\omega t)). \tag{8}$$

This is the required forward modeling formula giving the calculated voltage data at the time points at which the measured data were collected. As can be seen, the characteristic parameters of this model are: U_0, U_∞, λ_1, λ_2. In the following we use the relaxation times $\tau_1 = 1/\lambda_1$ and $\tau_2 = 1/\lambda_2$ as model parameters and introduce the model parameter vector

$$\vec{m} = \{m_1, m_2, ..., m_M\}^T, \tag{9}$$

where $m_1 = U_0$, $m_2 = U_\infty$, $m_3 = \tau_1$, $m_4 = \tau_2$ and $M = 4$ in our present case.

TIME-DEPENDENT VOLTAGE V(T) MEASUREMENT

For measurements the amorphous Mo_xGe_{1-x} superconducting films with weak pinning was prepared by rf sputtering on a Si substrate in a strip-like shape. The width and length between the voltage contacts are 0.3 mm and 1.2 mm, respectively. The vortices were driven in the direction of the sample width and the voltage generated by the vortex motion was measured by using the voltage contacts.

We used a ^{4}He cryostat to carry out the low-temperature experiments at 4.1 K. *Figure 4* shows the sample and the circuit used to measure the transient voltage response $V(t)$ of the vortex system. To drive the vortices, a voltage source Wave Factory 1965 (NF Corporation) was used which allows us to apply DC and AC drive to the system. To reduce the noise, we connected an attenuator (20dB) to the function generator that attenuates the voltage to 1/10. The voltage induced by the vortex motion was a hundredfold enhanced by a preamplifier (SA-400F3). The timescale of the vortex response is very short, usually in the order of a few milliseconds.

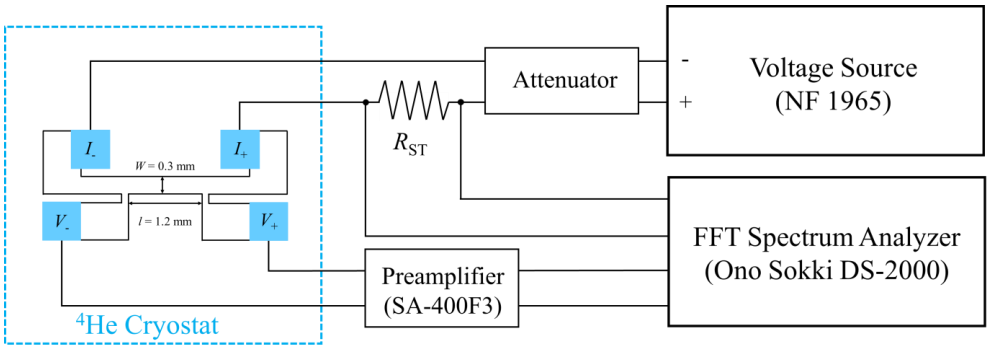

Figure 4. *Electrical circuit for the transient voltage response V(t) measurement. The blue dashed line indicates the ^{4}He cryostat*

To record the transient voltage precisely, we used an FFT spectrum analyzer (Ono Sokki DS-2000). Its voltage and time resolution are 10 μV and 25 μs, respectively. The measurement was computer regulated and the data samples were stored.

Figure 5 shows a typical data where the initially disordered vortex system is subjected to AC drive with displacement amplitude d = 5 μm in the steady-state. The increase in the amplitude of voltage indicates the dynamic ordering of the system. In the following, using a linearized Least Squares (LSQ) procedure, we estimate the characteristic parameters of dynamic ordering such as U^0 and U^∞, the initial and steady-state voltage amplitude and τ_1 and τ_2, the characteristic time of dynamic ordering and disordering, respectively.

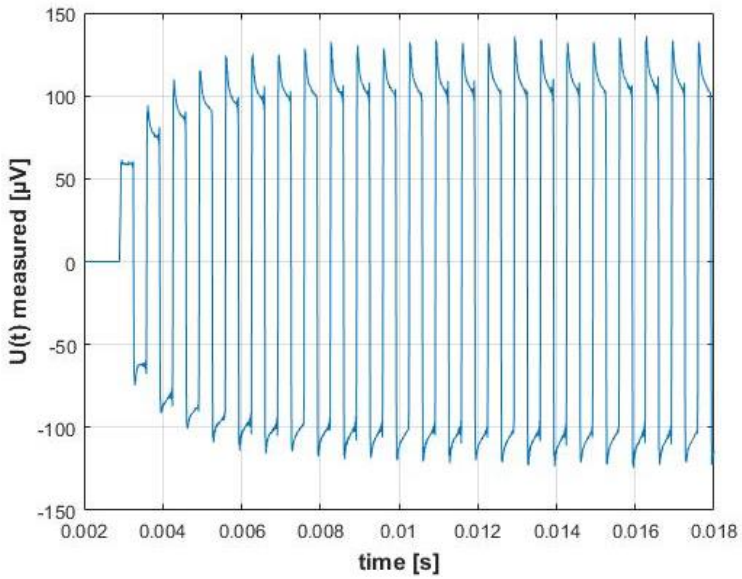

Figure 5. *The measured data set containing N = 1740 voltage data*

THE LEAST SQUARES INVERSION ALGORITHM

We denote the measured data set shown in *Figure 5* by a vector

$$\vec{d}^{\,m} = \left\{d_1^{(m)}, d_2^{(m)}, ..., d_N^{(m)}\right\}^T \tag{10}$$

containing the voltage samples found in different time points ($N = 1740$ in our case). The forward model gives the theoretical or computed data as a function of the model parameter vector

$$\vec{d}^{\,c} = \vec{g}(\vec{m}), \tag{11}$$

where the function is given in the form of Eq. (8). Using this equation we can calculate the voltage data at the same time points, that the measurement samples were collected and generate the vector of computed data

$$\vec{d}^{\,c} = \left\{d_1^{(c)}, d_2^{(c)}, ..., d_N^{(c)}\right\}^T. \tag{12}$$

In linearized inversion we approximate the calculated data using a truncated Taylor series expansion, so in the point

$$\vec{m} = \vec{m}_o + \delta\vec{m} \tag{13}$$

($\vec{m}_o$ being a start model) we write

$$d_k^c = g_k(\vec{m}_o) + \sum_{j=1}^{M}\left(\frac{\partial g_k}{\partial m_j}\right)_{\vec{m}_o} \delta m_j. \tag{14}$$

Introducing the Jacobi matrix

$$G_{kj} = \left(\frac{\partial g_k}{\partial m_j}\right)_{\vec{m}_o} \tag{15}$$

and the notation $d_k^{(o)} = g_k(\vec{m}_o)$, Eq. (14) gives

$$d_k^c = d_k^{(o)} + \sum_{j=1}^{M} G_{kj}\delta m_j$$

or in vector form

$$\vec{d}^{\,c} = \vec{d}^{\,(o)} + \underline{\underline{G}}\delta\vec{m}.$$

The difference between the $\vec{d}^{\,m}$ measured and the $\vec{d}^{\,c}$ calculated data can be written as

$$\vec{e} = \delta\vec{d}^{\,m} - \underline{\underline{G}}\delta\vec{m}$$

with $\delta\vec{d}^{\,m} = \vec{d}^{\,m} - \vec{d}^{\,(o)}$.

In our problem we have $M = 4$ unknown model parameters and $N = 1740$ measured data, so the inverse problem is appreciably overdetermined. In such a case the LSQ inversion algorithm is applied, giving estimated parameters by minimization of the

$$E = \vec{e}^T \vec{e}$$

functional, that means solving the equations given by the

$$\frac{\partial E}{\partial m_l} = 0, \quad l = 1,...,M$$

conditions. This results in the inhomogeneous linear set of equations

$$\underline{\underline{G}}^T \underline{\underline{G}} \delta\vec{m} = \underline{\underline{G}}^T \delta\vec{d}\,, \tag{16}$$

giving

$$\delta\vec{m} = (\underline{\underline{G}}^T \underline{\underline{G}})^{-1} \underline{\underline{G}}^T \delta\vec{d}\,. \tag{17}$$

The new parameter vector is given by *Equation (13)*. This procedure should be continued until a proper stop criterion is met. The parameter vector found in the last iteration is used to calculate predicted data vector $\vec{d}^{\,c}$ by means of *Equation (11)* (using the forward problem formula in *Equation (8)*. To qualify the inversion results the data distance

$$D = \sqrt{\frac{1}{N}\sum_{k=1}^{N}(d_k^m - d_k^c)^2} \tag{18}$$

and the elements of the $\underline{\underline{\mathrm{cov}\, m}}$ parameter covariance matrix

$$\underline{\underline{\mathrm{cov}\, m}} = \underline{\underline{G^{-g}}}\,\underline{\underline{\mathrm{cov}\, d}}\,(\underline{\underline{G^{-g}}})^T \tag{19}$$

are extensively used, where

$$G^{-g} = (\underline{\underline{G}}^T \underline{\underline{G}})^{-1} \underline{\underline{G}}^T$$

is the generalized inverse matrix [7], and $\underline{\underline{\mathrm{cov}\, d}} = D^2 \underline{\underline{I}}$ is the data covariance matrix, where $\underline{\underline{I}}$ is the unit matrix. The squared parameter estimation error (variance) is given by the diagonal elements of the parameter covariance matrix. The correlated nature of the model parameters can be characterized by means of the parameter correlation matrix defined as

$$(corr)_{i,j} = \frac{(\mathrm{cov})_{i,j}}{\sqrt{(\mathrm{cov})_{i,i}(\mathrm{cov})_{j,j}}}$$

and by its norm (the RMS value calculated by means of the off-diagonal elements).

RESULTS AND DISCUSSION

The measured data set shown in *Figure 5* was inverted using the LSQ algorithm. The estimated model parameters together with their estimation error are given in *Table 1*.

Table 1

The estimated model parameters with their estimation errors

Model parameter	Estimated value	Estimation error [V]	Relative error*100%
$m_1 = U_0$	61.0794 [μ V]	1.8262 [μ V]	2.99%
$m_2 = U_\infty$	117.341 [μ V]	6.6011 [μ V]	0.56%
$m_3 = \tau_1$	1.46797 [ms]	0.0825 [ms]	5.62%
$m_4 = \tau_2$	1.82181 [ms]	0.0987 [ms]	5.49%

The elements of the correlation matrix are given in *Table 2*. It can be seen that appreciable correlation exists only between m_2 and m_4 parameters. All of the other model parameters are weakly or moderately coupled. The correlation norm is 0.437, which shows a relatively stable inversion procedure.

Table 2

The elements of the parameter correlation matrix

	$m_1 = U_0$	$m_2 = U_\infty$	$m_3 = \tau_1$	$m_4 = \tau_2$
$m_1 = U_0$	1.0000	0.2033	0.6061	–0.1510
$m_2 = U_\infty$	0.2033	1.0000	0.2711	–0.8010
$m_3 = \tau_1$	0.6061	0.2711	1.0000	0.0001
$m_4 = \tau_2$	–0.1510	–0.8010	0.0001	1.0000

Figure 6 shows the fitting between the measured data (blue curve) and the predicted data [calculated by means of *Equation (8)* using the estimated model parameters] (red curve). It can be stated that the LSQ inversion procedure gives highly acceptable results.

The accurate determination of the relaxation time parameters *(* τ_1 and τ_2 *)* is very important in studying dynamic ordering and also dynamic disordering phenomena. It can be seen that the method presented is able to give also the estimation errors, which seems to be highly acceptable for our measurement surroundings.

It was shown both numerically and experimentally that as the displacement amplitude of the vortices increases, the system undergoes a transition from reversible to irreversible state. This transition also can be observed as a divergence of relaxation times τ_1 on both sides of the transition with critical exponents slightly larger than unity. It has also been suggested that this non-equilibrium transition from reversible

to irreversible state may fall into the universality class of plastic depinning and absorbing phase transitions, which includes directed or conserved directed percolation. A more accurate estimation of the relaxation parameters can be useful to get a further insight into these phenomena.

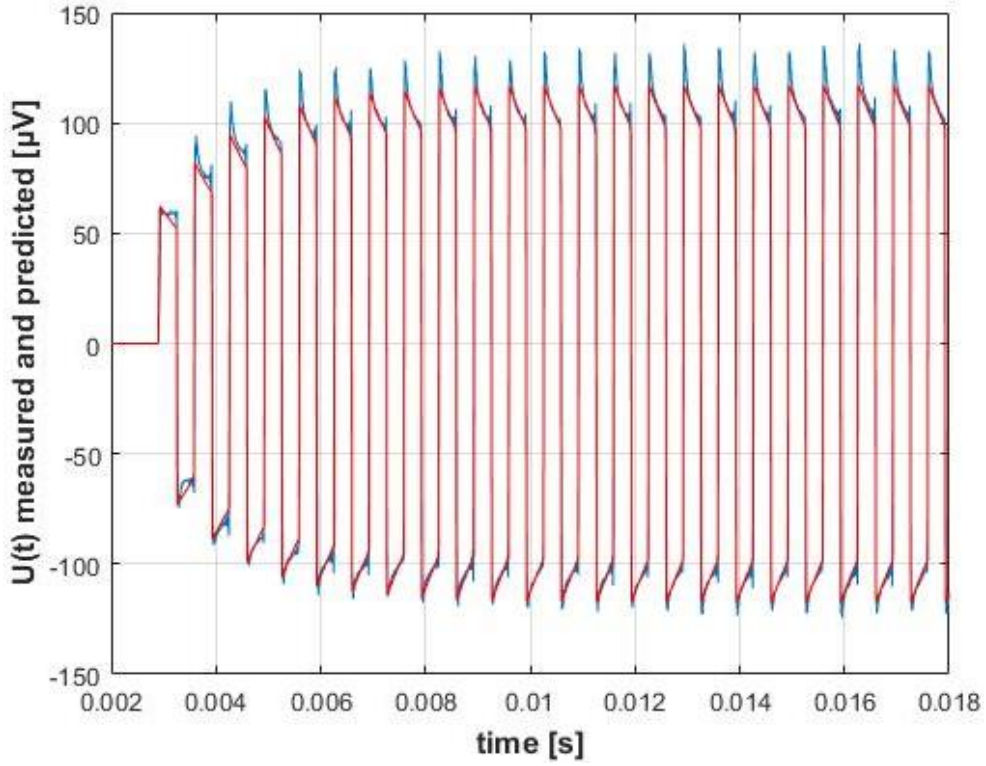

Figure 6. *The fitting between measured (blue curve) and calculated (red curve) data*

CONCLUSION

The linearized Least Squares algorithm was applied for the inversion of the dynamic ordering data measured on amorphous Mo_xGe_{1-x} superconducting films of type II. The forward modeling formulae were given by using elementary statistical assumptions. The estimated model parameters were given together with their estimation error. The inversion algorithm was proved to be stable and accurate by means of the low level of parameter correlation and the highly acceptable fitting between the measured data and the data calculated or predicted using the estimated model parameters and the forward modeling formula.

ACKNOWLEDGEMENT

The author expresses his deep gratitude to his father, Professor M. Dobróka, for helpful discussions.

APPENDIX

Let us assume that due to the initial DC current we have N_0 pinning centers (each occupied by a vortex) and at $t = 0$ we have n_0 free vortices. So the total number of vortices (free and bounded) is $n_0 + N_0$. In the dynamic ordering procedure in response to the AC current some vortices escape in the pinning. It is obvious to assume, that at time t the dN decrease of the number of occupied pinnings (in a time interval dt) is proportional to the $N(t)$ number of the instantaneously occupied pinnings and dt:

$$dN = -\lambda_1 N dt ,$$

where λ_1 is a proportionality factor (a material parameter). This gives

$$N(t) = N_0 \exp(-\lambda_1 t)$$

with the N_0 occupied pinning centers at $t = 0$. The number of the abandoned pinning centers

$$N_0 - N(t) = N_0 (1 - \exp(-\lambda_1 t)) \tag{A1}$$

is the same as the increase in the number of the free vortices, so

$$n(t) = n_0 + N_0 (1 - \exp(-\lambda_1 t)) \tag{A2}$$

giving $n_\infty = n_0 + N_0$ at $t = \infty$. From this

$$N_0 = n_\infty - n_0 \tag{A3}$$

and so

$$n(t) = n_0 + (n_\infty - n_0)(1 - \exp(-\lambda_1 t)) \tag{A4}$$

Using *Equation (5)* we introduce the U_0 voltage belonging the n_0 initial number of free vortices (at $t = 0$) and similarly U_∞ belonging the n_∞ number at t_∞. In accordance with the results of Henderson and Andrei [6] here we assume that the velocity (after a very short transient) tends to a stationary value v_0 giving the time dependent velocity

$$v(t) = v_0 sygn(\sin(\omega t)) \tag{A5}$$

which is common in U_0 and U_∞. So we find the time varying voltage belonging the $n(t)$ given in *Equation (A4)* as

$$U(t) = \left[U_0 + (U_\infty - U_0)(1 - \exp(-\lambda_1 t))\right] sygn(\sin(\omega t)) . \tag{A6}$$

Equation (A6) is the required forward modeling formula for dynamic ordering. Due to the situation depicted in *Figure 3* the expression describes an increase in the envelope curve of the amplitude. Apart from the sygnum function, *Equation (A6)* is similar to that extensively used in the literature describing various kinds of dynamic ordering (Corté et al. [1], Reichhardt et al. [2]).

As can be seen in *Figure 3*, in each new half period an opposite process starts with exponential decrease of the voltage. This is caused by the fact that after the change in sign of the driving current the direction of the velocity also changes *[Equation (A5)]*; consequently, the vortices turn back to the vicinity of the pinning centers from which they were previously escaping. This procedure can result in some vortices becoming trapped. In the *q*-th half cycle $(q-1)T/2 \le t \le qT/2$ the number of occupied pinnings increases. It is obvious that its $dN \ge 0$ change is proportional to the $N_0 - N(t)$ number of the unoccupied pinnings

$$dN = \lambda_2 (N_0 - N(t))\, dt \tag{A7}$$

where λ_2 is another material constant. Taking into account *Equations (A1)* and *(A2)* $n(t) = n_0 + N_0 - N(t)$ one finds

$$dn = -\lambda_2 (n - n_0)\, dt\,,$$

giving

$$n(t) - n_0 = C \exp(-\lambda_2 t)\,. \tag{A8}$$

To determine the integration constant C we require the initial condition at $t_q = (q-1)T/2$ (the beginning of the *q*-th half cycle)

$$n(t_q) - n_0 = C \exp(-\lambda_2 t_q)\,,$$

resulting in

$$n(t) - n_0 = (n(t_q) - n_0) \exp(-\lambda_2 (t - t_q))\,. \tag{A9}$$

Taking into account *Equation (A4)* (at $t = t_q$) we find

$$n(t) = n_0 + (n_\infty - n_0)(1 - \exp(-\lambda_1 t_q)) \exp(-\lambda_2 (t - t_q))\,. \tag{A10}$$

Using again *Equation (5)* we can write U_0 and U_∞ voltages belonging to the n_0 and n_∞ vortex numbers, respectively, and find

$$U(t) = \left\{U_0 + (U_\infty - U_0)(1 - \exp(-\lambda_1 t_q)) \exp(-\lambda_2 (t - t_q))\right\} sygn(\sin(\omega t))\,, \tag{A11}$$

which is the required forward modeling. In agreement with the terminology of inverse problem theory *Equation (A11)* gives the calculated voltage data at the time points when the measured data were collected.

REFERENCES

[1] Corté, L., Chaikin, P. M., Gollub, J. P. & Pine, D. J. (2008). Random organization in periodically driven systems. *Nature Phys.*, 4, 420.

[2] Reichhardt, C. & Olson Reichhardt, C. J. (2009). Random Organization and Plastic Depinning. *Phys. Rev. Lett*., 103, p. 168301.

[3] Dobroka, M., Kawamura, Y., Ienaga, K., Kaneko, S. & Okuma, S. (2017). Memory formation and evolution of the vortex configuration associated with random organization. *New J. Phys.*, 19, 053023 .

[4] Ienaga, K., Dobroka, M., Shirahata, Y., Kawamura, Y., Kaneko, S. & Okuma, S. (2017). Random organization of vortices under an anisotropic condition. *J. Phys. Conf. Ser.*, 871, 012020.

[5] Zhou, C., Olson Reichhardt, C. J., Reichhardt, C. & Beyerlein, I. (2014). Random organization in periodically driven gliding dislocations. *Phys. Lett A.*, 378, 1675.

[6] Henderson, W., Andrei, E. Y. & Higgins, M. J. (1998). Plastic Motion of a Flux-line Lattice Driven by Alternating Current. *Phys. Rev. Lett.*, 81, 2352.

[7] Menke, W. (1984). *Geophysical data analysis: Discrete inverse theory*. Academic Press Inc.